Heliostat Cost Reduction for Power Tower Plants

by
Arvind Sastry Pidaparthi

Thesis presented in partial fulfilment of the requirements for the degree of Master of Engineering (Mechanical) in the Faculty of Engineering at Stellenbosch University

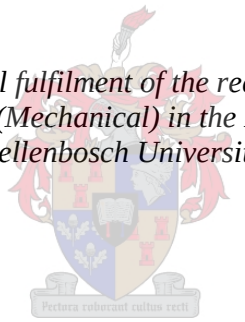

Supervisor: Dr. Jaap Hoffmann

March 2017

Declaration

By submitting this thesis electronically, I declare that the entirety of the work contained therein is my own, original work, that I am the sole author thereof (save to the extent explicitly otherwise stated), that reproduction and publication thereof by Stellenbosch University will not infringe any third party rights and that I have not previously in its entirety or in part submitted it for obtaining any qualification.

Date: March 2017

Abstract

Heliostats typically contribute to about 40 % of the total installed costs in a concentrated solar power (CSP) tower plant. The objective of this study is to investigate the effects of heliostat size on the levelized cost of electricity (LCOE). These effects are analysed in a power tower with a net capacity of 100 MW_e with 8 hours of thermal energy storage in Upington, South Africa. A large, medium and a small sized heliostat with a total area of 115.56 m^2, 43.33 m^2 and 16.69 m^2 respectively are considered for comparison. The heliostat cost per unit is calculated separately for the three different heliostat sizes and the effects due to size scaling, learning curve benefits and the price index is considered. The annual operation and maintenance (O&M) costs are estimated separately for the three heliostat fields, where the number of personnel required in the field is determined by the number of heliostats in the field. The LCOE values are used as a figure of merit to compare the different heliostat sizes. The lowest theoretical LCOE value of 0.1960 $\$/kWh_e$ is achieved using the medium size heliostat with an area of 43.33 m^2 for this power tower configuration.

Opsomming

Heliostate dra gemiddeld 40 % by tot die totale geïnstalleerde kostes van ‘n sentrale toring gekonsentreerde sonkrag stasie. Die doel van hierdie studie is om die effek van heliostaat grote op die huidige waarde van die gemiddelde jaarlikse totale koste, [“Levelized Cost of Electricity” (LCOE)] van só ‘n kragstasie te ondersoek. Hierdie effekte word ondersoek op ‘n toring met ‘n kapasiteit van 100 MW_e, en 8 ure se termiese stoor kapasiteit, in Upington, Suid Afrika. ’n Groot, medium en klein heliostaat sal gemodelleer word, met oppervlak areas van 115.56 m^2, 43.33 m^2 en 16.69 m^2 elk, om die resultate te vergelyk. Die heliostaat eenheidskostes word apart bereken vir elk van die drie grotes, met die effekte van opskalering, leer-kurwe voordele en prys-indekse in ag geneem. Die jaarlikse operasionele en onderhoud kostes word vir elke grote apart beraam, waar die hoeveelheid personeel benodig bepaal word deur die hoeveelheid helsiostate in die veld. Die LCOE waardes vir elke grote word gebruik om die meriete daarvan te bepaal. Die laagste teoretiese LCOE wat bereik is, was 0.1960 $\$/kWh_e$, vir die 43.33 m^2 heliostaat.

Acknowledgements

I would like to express my sincere gratitude to the following people and organizations:

Department of Mechanical Engineering, Stellenbosch University and the Solar Thermal Energy Research Group (STERG) that provided the funding for this research.

Dr. J.E. Hoffmann, Senior Lecturer - Department of Mechanical Engineering, Stellenbosch University for his guidance as my supervisor and the freedom he gave me to choose a topic that highly interested me.

Prof. Frank Dinter, Director - Solar Thermal Energy Research Group (STERG) for his support and guidance during my research.

Mr. E.P Dall, with whom I worked very closely and shared ideas about our keen interest in concentrating solar power (CSP) technology and who co-authored a paper with me on CSP performance analysis in SolarPACES 2015.

Researchers from the Helio 100 team (Paul Gauché, Willem Landman and James Larmuth) and STERG for their valuable suggestions.

I would like to thank my family for their love and support – my parents and my brother who always encouraged me to work in the field of renewable energy.

My wife, Manjari, for her love and support during these two years.

My friends at Stellenbosch University, staff at the Department of Mechanical Engineering, the writing lab and Concordia housing.

Dedications

I dedicate this work to my grandfather KVRK Sastry who introduced me to the world of Physics.

॥ ॐ ध्येयः सदा सवित्र मण्डल मध्यवर्ती नारायण सरसिजा सनसन्नि विष्टः
केयूरवान मकरकुण्डलवान किरीटी हारी हिरण्मय वपुर धृतशंख चक्रः ॥

Always focus your attention at the centre of the solar system,

where the sun, the supreme power of the universe, resides.

(Sukhatme, 1996)

Table of contents

List of figures

List of tables

Nomenclature

A^0_h	Reference heliostat area (m^2)
A^0_{rec}	Reference receiver area (m^2)
A_{eff}	Effective reflected image area (m^2)
A_h	Heliostat total area (m^2)
A_{ineff}	Ineffective reflected image area (m^2)
A_l	Total land area (m^2)
A_{rec}	Total surface area of the receiver (m^2)
A_{sf}	Total reflective area of the heliostat field (m^2)
A_{total}	Total reflected image area (m^2)
B	Function of day number N (degrees)
C_a	Heliostat assembly cost ($)
C_c	Heliostat control system cost ($)
$C_{c,tot}$	Total contingency cost ($)
C_d	Heliostat drive cost ($)
$C_{d,s}$	Subtotal direct cost of the plant ($)
$C_{d,tot}$	Total direct cost ($)
$C_{EPC,tot}$	Total EPC cost ($)
CF	Capacity factor (%)
C_f	Heliostat foundation cost ($)
C_h	Individual heliostat cost ($)
$C_{h,opt}$	Heliostat optical improvement cost ($)

$C_{h,optic}$	Optical improvement cost per heliostat ($/unit)
$C_{h,tot}$	Total heliostat field cost ($)
c_i	Attenuation coefficient with i ranging from 0 to 3 (-)
$C_{i,tot}$	Total indirect costs of the plant ($)
$C_{inst,tot}$	Total installed cost ($)
C_l	Cost per total land area ($/acre)
$C_{l,tot}$	Total cost of the land ($)
C_m	Heliostat mirror cost ($)
$C_{net,cap}$	Total cost per net capacity of the plant ($/kW$_e$)
CP	Contingency as a percentage of the total direct costs (%)
C_{PB}	Power block cost per electric kilowatt ($/kW$_e$)
$C_{PB,tot}$	Total power block investment cost ($)
$C_{piping,c}$	Constant piping loss (kW$_t$)
$C_{piping,s}$	Losses that scale with height of the tower (kW$_t$/m)
$C_{r,ref}$	Reference receiver cost ($)
$C_{r,tot}$	Total Receiver cost ($)
CRF	Capital recovery factor (-)
C_s	Heliostat structure cost ($)
C_s	Site improvement cost ($/m^2)
$C_{s,tot}$	Total site improvement cost ($)
C_{SGS}	Steam generation system cost ($/kW$_e$)
$C_{SGS,tot}$	Total SGS costs ($)
$C_{ST,tot}$	Total Sales tax cost ($)

$C_{t,fixed}$	Fixed tower cost ($)
$C_{t,tot}$	Total tower cost ($)
C_{TES}	Thermal energy specific ($/kWh$_t$)
$C_{TES,tot}$	Total TES system cost ($)
$C_{w,i}$	Polynomials that scale thermal losses with wind velocity (-)
D	Daylight savings (h)
d	Slant distance between heliostat and tower (m)
D_{helio}	Heliostat footprint diameter (m)
D_{image}	Size of reflected image (m)
DNI	Total Annual DNI value (kWh/m^2/year)
D_{rec}	Receiver diameter (m)
ds	Separation distance (m)
$E_{e,a}$	Annual net electrical energy (kW$_e$)
EOT	Equation of time (min)
$EPCP$	EPC costs as a percentage of the total direct costs (%)
E_{rec}	Annual energy reaching the receiver (kW$_t$)
f	Heliostat aspect ratio (-)
f_b	Blocking factor (-)
h_{fc}	Heat transfer coefficient accounting for forced convection (W/(m^2/K))
H_{gap}	Gap length between the panels in the horizontal dimension (m)
H_{helio}	Heliostat height (m)
h_{mix}	Mixed heat transfer coefficient (W/(m^2/K))
h_{nc}	Heat transfer coefficient accounting for natural convection (W/(m^2/K))

H_{rec}	Receiver height (m)
H_t	Tower height (m)
I	Intercepted energy (W)
k_d	Annual debt interest rate (%)
k_i	Annual insurance rate (%)
k_{rec}	Receiver cost scaling exponent (-)
k_t	Tower cost scaling exponent (-)
LC	Longitude correction (h)
$LCOE$	Levelized cost of electricity ($/kWh$_e$)
LCT	Local clock time (h)
L_v	Length of the vertical axis (m)
n	Plant lifetime (years)
N	Day ‘number’ of the year (-)
N	Heliostat normal (-)
n	unitized heliostat normal (-)
$N_{h,TES}$	Number of full load hours of storage (h)
N_{hel}	Total number of heliostats in the field (-)
$N_{panel,h}$	Number of panels in the horizontal dimension (-)
$N_{panel,v}$	Number of panels in the vertical dimension (-)
$OPEX$	Annual O&M costs ($)
pi	Price index (-)
pr	Progress ratio (-)
Q_{cycle}	Cycle thermal power (MW$_t$)

Q_{des}	Receiver design–point thermal rating (MW_t)
Q_{in}	Incident power (W)
Q_{loss}	Heat loss from the receiver system (W)
$Q_{loss,des}$	Design point thermal losses (W)
Q_{piping}	Piping thermal losses (W)
R_{GtoN}	Gross to net conversion factor (-)
s	Scaling factor (-)
SM	Solar multiple (-)
STB	Percentage of total direct costs used to calculate Sales tax (%)
STR	Sales tax rate (%)
t	scalar parameter of the three dimensional object equations (-)
t	Unitized target vector (-)
T_{amb}	Ambient temperature (K)
t_s	Solar time (h)
T_{wall}	Average receiver surface temperature (K)
V^0_h	Reference volume of production as exponent (-)
V_h	Current volume of production (-)
v_{wind}	Wind velocity (m/s)
W_{des}	Design turbine gross output (MW_e)
W_{gap}	Gap length between the panels in the vertical dimension (m)
W_{helio}	Heliostat width (m)
W_{net}	Design net output rating of the turbine (MW_e)
x	Function of day number N (degrees)

ΔAZ	Azimuthal distance between two heliostats in a row (m)
ΔR	Radial distance between two heliostat rows (m)

Greek alphabet

α	Receiver thermal absorptance (-)
α_z	Solar altitude angle (degrees)
β	Slope of the field (degrees)
γ_s	Solar azimuth angle (degrees)
δ	Declination angle (degrees)
ε	Receiver thermal emittance (-)
ε_T	Elevation angle of the heliostat (degrees)
η_a	Atmospheric attenuation efficiency (%)
η_b	Blocking efficiency (%)
η_c	Cosine efficiency (%)
η_{des}	Cycle thermal efficiency (%)
η_{des}	Rated cycle conversion efficiency (%)
η_i	Image interception/spillage efficiency (%)
η_{rec}	Receiver efficiency (%)
η_s	Shading efficiency (%)
η_{sf}	Solar field efficiency (%)
θ	Angle of incidence (degrees)
θ_Z	Zenith angle (degrees)
σ_{assemb}	Assembly error (mrad)

σ_{ast}	Astigmatic error (mrad)
σ_{bq}	Beam quality error (mrad)
σ_{gl}	Gravitational load error (mrad)
σ_{mirror}	Wind load error (mrad)
σ_{shape}	Error due to deformations from self loads (mrad)
σ_{slope}	Macro slope error (mrad)
$\sigma_{specular}$	Tracking error (mrad)
σ_{sse}	Surface slope error (mrad)
σ_{sun}	Sunshape error (mrad)
σ_{temp}	Gravitational load error (mrad)
σ_{tl}	Temperature load error (mrad)
σ_{tot}	Effective beam dispersion error (mrad)
σ_{track}	Tracking error (mrad)
σ_{wl}	Wind load error (mrad)
φ	Angle between the receiver and the target vector (degrees)
ϕ	Latitude angle (degrees)
ω	Hour angle (degrees)

Subscripts

i	Heliostat number (-)
E	East (degrees)
H	Hour number (-)
N	North (degrees)
T	Target vector (-)

z	Zenith (-)

Constants

π	3.1416
λ	9.3 mrad
σ	Stefan-Boltzmann constant (5.67×10^{-8} W/m^2/K^4)

Abbreviations

AFD	Allowable Flux Density
BOP	Balance of Plant
CED	Cumulative Energy Demand
CPV	Concentrated Photovoltaic
CRF	Capital Recovery Factor
CSIRO	Commonwealth Scientific and Industrial Research Organisation
CSP	Concentrated Solar Power
DLR	Deutschen Zentrums für Luft - und Raumfahrt
DNI	Direct Normal Irradiance
EPC	Engineering, Procurement and Construction
GHG	Greenhouse Gas
GIS	Geographic Information Systems
GUI	Graphical User Interface
HAB	Heliostat Assembly Building
HFLCAL	Heliostat Field Layout Calculator
HTF	Heat Transfer Fluid
LCA	Life Cycle Assessment

LCOE	Levelized Cost of Electricity
LFR	Linear Fresnel Reflectors
MCRT	Monte Carlo Ray Tracing
NREL	National Renewable Energy Laboratory
O&M	Operations and Maintenance
PSA	Plataforma Solar de Almeria
PT	Parabolic Trough
PV	Photovoltaics
PVB	Polyvinyl butyral
REIPPPP	Renewable Energy Independent Power Producers Procurement Program
RSGS	Response Surface Generating System
RSS	Root Sum Squared
SGS	Steam Generating System
SNL	Sandia National Laboratories
SolarPILOT	Solar Power Tower Integrated Layout and Optimization Tool
STERG	Solar Thermal Energy Research Group
SUNSPOT	Stellenbosch University Solar Power Thermodynamic (cycle)
TES	Thermal Energy Storage
TMY	Typical Meteorological Year
TOD	Time of Day
USA	United States of America
ZAR	South African Rand

1. Introduction

Renewable energy has the potential to supply clean and affordable energy to billions of people across the world. Implementing renewable energy technologies have several advantages which include reduction in pollution levels and creation of new jobs. There are several ways of producing electricity by renewable energy sources, some of which are: Hydro, wind, solar, biomass and tidal energy.

Solar energy can be used for power production, process heat and even cooling applications for the residential and industrial sectors. Solar energy is starting to play a major role in electricity generation and as of early 2016 around 231.8 GW is installed worldwide (REN21, 2016). The solar energy technologies that can be used for power production are solar Photovoltaics (PV) and Concentrated Solar thermal Power (CSP) systems.

PV systems use cells or modules (several cells make up a module) to convert sunlight into direct current. Currently, PV systems are the most widely used solar energy technology for power production and make up for about 227 GW out of the 231.8 GW installed worldwide (REN21, 2016). This is partly due to the fact that these systems can be mounted on the rooftop of a commercial or residential building. PV systems have reached grid parity and are now cost competitive with fossil fuel sources.

CSP systems use mirrors (also called reflectors) with very high reflectivity to concentrate the direct beam radiation (or direct normal irradiance (DNI)) onto a receiver. The radiation is absorbed by the receiver as heat and this heat is transferred to a fluid called heat transfer fluid (HTF) (IRENA, 2013). This heat can be then be used as process heat for various applications or to produce steam in a heat exchanger and generate electricity through steam turbines. CSP tower plants use sun tracking mirrors, also called heliostats, to direct beam radiation onto a central receiver placed on the top of a tower.

This study aims to explore the subject of heliostat cost reduction by investigating the effects of heliostat size on the LCOE for power tower plants. Heliostat cost as a function of size and the optical performance of the heliostat field are included in a holistic LCOE model which compares heliostats of different sizes in a radial staggered

heliostat field layout. Heliostats are often compared on 'cost per square meter' basis which does not consider scaling effects, learning curve benefits, subcomponent cost comparison or the optical performance of the heliostat field layout (Larmuth *et al.*, 2016). This study approaches the method of using LCOE as a figure of merit proposed by Weinrebe *et al.* (2014).

1.1 Background

One of the major engineering challenges faced by engineers working with CSP technology is to effectively concentrate the beam radiation onto the receiver with proper sun tracking techniques (Müller-Steinhagen and Trieb, 2004). This can be achieved by line or point focussing systems. Line focussing systems use rows of parabolic troughs (PT) or linear Fresnel reflectors (LFR) to concentrate the beam radiation onto a stainless steel absorber tube. Special coatings are used on the absorber tube to improve the absorptivity. These systems track the sun in one axis and have low concentration ratios. Concentration ratio is defined as the "the ratio of the area of aperture to the area of the receiver" (Duffie and Beckman, 2013) and higher concentration ratios are desirable for CSP systems. High concentration ratios are indicators of higher operating temperatures and greater precision in tracking the sun.

Point focussing systems use curved mirrors mounted on a structure (parabolic dish) or heliostats arranged in a field (power towers or central receivers). Power tower systems have high concentration ratios, thus have the capability to reach very high operating temperatures. Higher operating temperatures lead to higher cycle thermal efficiencies and have a positive effect on the levelized costs of energy (LCOE) (Guédez *et al.*, 2015). Power towers with molten salt as primary HTF can realize temperatures as high as high as 565 °C. Most parabolic trough plants which are currently operational use synthetic oil as HTF and can only operate at a maximum temperature of 393 °C due to temperature limitations of the HTF (Relloso and Lata, 2011). Currently, power tower plants are more capital intensive than parabolic trough plants, due to lower technology maturity and greater land requirements. However, power towers are advantageous since less site preparation is needed and have higher plant efficiencies.

A major advantage with CSP systems is that these plants can be combined with thermal energy storage (TES) systems (Guédez *et al.*, 2015; Helman and Jacobowitz, 2014). This is essential as electricity can be produced after sunset and during peak demand

hours, thereby increasing the capacity factor and the annual energy yield of the plant, which in turn has an effect on the LCOE. The method of calculation of LCOE is widely accepted and used to compare power plants with different technologies on the basis of cost structures and power generation (Kost *et al.*, 2013). Power towers with several hours of TES have the potential to achieve low LCOE values and capacity factors as high as 80 % (Crespo *et al.*, 2012). The high operating temperatures allow for a higher temperature differential, thus reducing the costs of TES (Crespo *et al.*, 2012).

In spite of all these advantages, power towers still face many challenges as they are capital intensive. The major subsystem costs for power towers are: solar collector field, solar receiver, thermal energy storage and power block/balance of plant (Kolb *et al.*, 2011). The heliostat field is one of major cost components of power towers and accounts for about 40 % of the total plant installed costs (Pfahl, 2014). It is therefore very important to reduce heliostat costs to meet the ambitious cost objectives set by the CSP industry of reaching an LCOE of 0.06 $/kWh$_e$ by the year 2020 (U.S. Department of Energy, 2012). This is essential as power towers represent 40 % of the capacity of the CSP plants currently under construction worldwide (REN21, 2015). As of early 2016, the CSP sector has added a total capacity of 4.8 GW worldwide (REN21, 2016) and many more plants are in the construction or development phase. Spain is currently the world leader in terms of the capacity installed with almost 2.3 GW of CSP plants installed (D'Ortigue, 2015). Power towers with a total capacity of 593 MW$_e$ have been built till date and approximately 400 MW$_e$ are under construction (ESTELA *et al.*, 2016).

This study addresses the issue of heliostat cost reduction while evaluating the 'best suitable heliostat size for a given power tower plant. The hypothetical power tower in consideration is the ESKOM 100 MW$_e$ plant (ESKOM, 2016) which is being considered for Upington, Northern Cape Province (Hoffmann and Madaly, 2015). Heliostat cost reduction for power towers forms a part of research being conducted in the field of renewable energy technology.

1.2 Motivation

The true potential of CSP technology can be estimated when one takes a look at South Africa's annual DNI values, which are as high as 3000 kWh/m^2 in some locations in the Northern Cape (Meyer, 2012). These values are amongst the highest in the world

and are considered ideal for operating power tower plants. A study conducted in 2009 using Geographic Information Systems (GIS) indicates that South Africa has a potential to accommodate CSP plants with a total nominal capacity of 547.5 GW (Fluri, 2009). However, the results of this study only assumed parabolic trough technology installations and did not consider power tower plants. Therefore, it is also important to consider power tower plants in future studies since power towers are much more capital intensive than parabolic trough plants (IRENA, 2016) and need greater land area to build these plants (Ong et al., 2013).

The first power tower plant in South Africa was commissioned in 2016 in Upington, Northern Cape. The plant – Khi solar one – is a direct superheated steam power tower project with a gross capacity of 50 MW_e and approximately two hours of steam storage (Silinga *et al.*, 2015). This plant was developed by Abengoa Solar and has approximately 4120 heliostats, each with an aperture area of 140 m^2 (Geyer, 2014). These 'ASUP 140' heliostats were introduced by Abengoa in 2012 and are based on the 'SL 120' heliostats installed in PS 10 and PS 20 plants in Spain and are expected to lower the costs of the heliostat field by approximately 30 % (Abengoa, 2012). These heliostats will also be used in Abengoa's 110 MW_e Atacama 1 power tower plant in Chile (Abengoa, 2015).

The second power tower plant in the development phase in South Africa is the Redstone solar thermal power project in Postmasburg, Northern Cape. This plant is being developed by SolarReserve and ACWA Power and is expected to start operations in 2018. The plant will have a gross capacity of 100 MW_e with 12 hours of storage and will generate around 480 000 MWh annually (SolarReserve, 2015). There is no information yet on the heliostats for this plant. SolarReserve's other power tower plant – Crescent Dunes – in Nevada, USA uses the 'pathfinder 2' heliostats, each with an aperture area of 62.5 m^2 (Tonopah Solar Energy LLC, 2009) . That plant has a total reflective area of 1 081 250 m^2 with a total of 17 300 heliostats (Augsburger, 2013).

The third power tower in South Africa– Kiwano Solar Power Plant – is in the planning phase with a gross capacity of 100 MW_e and is being developed by ESKOM, the country's electricity public utility. This plant will have molten salt as HTF and will likely include storage (Hoffmann and Madaly, 2015). The heliostat size has not yet been determined. This study aims to look at the best suitable heliostat size for this plant.

The heliostat field is the most expensive component in a power tower system. Therefore reducing these costs is very important for future market development of power tower plants. The configuration of power towers (net capacity not exceeding 150 MW_e) in

the planning/development phase in the Renewable Energy Independent Power Producer Procurement Programme (REIPPPP) in South Africa is considered for recommending the optimum heliostat size.

1.3 Objective

The objectives of the study are to:

- Select three heliostats from the three existing defined size ranges, based on the level of commercialization and suitability of implementation in utility scale power towers.
- Review established trends about the heliostat cost-area proportionality for the selected heliostat sizes.
- Develop a mathematical model to include the optical performance of three given heliostat fields and the capital costs of heliostats.
- Optimize the heliostat field layouts to obtain the heliostat positions, receiver dimensions, and tower height and include these parameters in a holistic LCOE model.
- Provide design recommendations, based on the LCOE results, for the best suitable heliostat size for power towers in South Africa with a net capacity of 100 MW_e.

1.4 Outline

Chapter 2 describes the location and the design of the power tower plant which sets the scope of the research.

Chapter 3 contains a literature review of the existing research about heliostats in power tower plants, history of heliostat development, variations in heliostat sizes and various heliostat cost reduction studies conducted in the past.

Chapter 4 reviews the heliostat cost as a function of size where heliostats are categorized according to their size. The theory behind the cost-area proportionality used for heliostats is described.

Chapter 5 presents the model developed for the energy performance of the heliostat field where the energy intercepted from the heliostat field is calculated. This involves the precise calculation of the losses in various stages when beam radiation is intercepted at the receiver.

Chapter 6 presents the method in which the heliostat field layout is generated for a 100 MW_e power tower with 8 hours of TES and a SM of 1.8. The field is then optimized and the optimal field layout is then developed. The optical performance simulation results for the heliostat field are then presented.

Chapter 7 presents the economic performance of the power tower configuration. The direct capital costs are calculated with emphasis on heliostat costs developed based on principles observed in Chapter 4. The indirect capital costs and the operations and maintenance (O&M) costs are calculated separately in the cost model.

Chapter 8 combines the thermo-economic performance of the power tower plant and presents the method of calculation of LCOE which is used as a figure of merit for the comparison of the three heliostats chosen for the study.

Chapter 9 presents the results of the study and concludes with the recommendations for future work in this field of research.

2. Plant location and system design

CSP plants utilize only the DNI which is defined as irradiance on the collector perpendicular to the vector from the centre of the sun to the observer and which passes through the atmosphere unaffected (WMO, 2008). There are three major ways to obtain the DNI for a given location: Ground measurements, satellite derived data and to use the combined ground measurements with satellite derived data (Sengupta *et al.*, 2015). Direct ground measurements are given by stations in daily, hourly or sub-hourly intervals and are usually located in areas with high population density, while the locations best suited for CSP plants are either deserts or areas which are very arid and dry (Seidel, 2010). These regions receive a lot of sunlight and since there is significantly less pollution and aerosol density, the direct beam radiation is high (Trieb, 2007). This section describes the plant location in South Africa and design of the power tower plant. The suitable location must have a proper connection to the transmission grid, availability of water and connections via air, railways and roads.

2.1 Site assessment - Solar resource data

The Northern Cape Province in South Africa has attracted several CSP developers as some locations in the province have DNI values as high as 3000 kWh/m^2/year (Meyer, 2013). The site chosen for this study is near Upington where a solar park is being considered. The site has a potential for very high solar energy yields combined with good infrastructure needed to build power towers.

A site assessment report was prepared with ground measurements for more than four years and has been compared with satellite derived solar radiation resulting in an enhanced long term DNI average of 2816 kWh/m^2/year (Suri, 2011). The terrain is mostly flat hence the site considered for this region is not expected to be affected by any shading. The annual yield of a CSP plant can be calculated in time steps of 60 minutes or interpolated on intervals less than 60 minutes. For this study, hourly values of solar radiation data are used from a typical metrological year (TMY).

2.2 Local conditions and weather data

Local weather conditions like ambient temperature and wind speeds play an important role in the efficiency and annual yield of the whole system. These effects have to be taken into consideration while designing the CSP system. Wind plays a major role in the design of a power tower plant. High wind speeds affect the tracking of the heliostats and lower the accuracy of tracking due to bending and oscillations in the structure (Peterka and Tan, 1987). Higher wind speeds also increase convective losses from the receiver to the atmosphere, thus affecting the first law efficiency of the system. According to Augsburger (2013), wind plays an indirect role in the transient behaviour of the receiver: velocity of a cloud passing over the heliostat field influences the amount of flux reaching the receiver. Fast changes in the flux might cause thermal fatigue or sometimes even failure in the cyclic operation of the receiver and hence its lifetime (Sobin *et al*., 1976). Figure 2.1 shows a plot of the frequency of occurrence of wind speeds in the region using TMY3 weather data from Meteonorm.

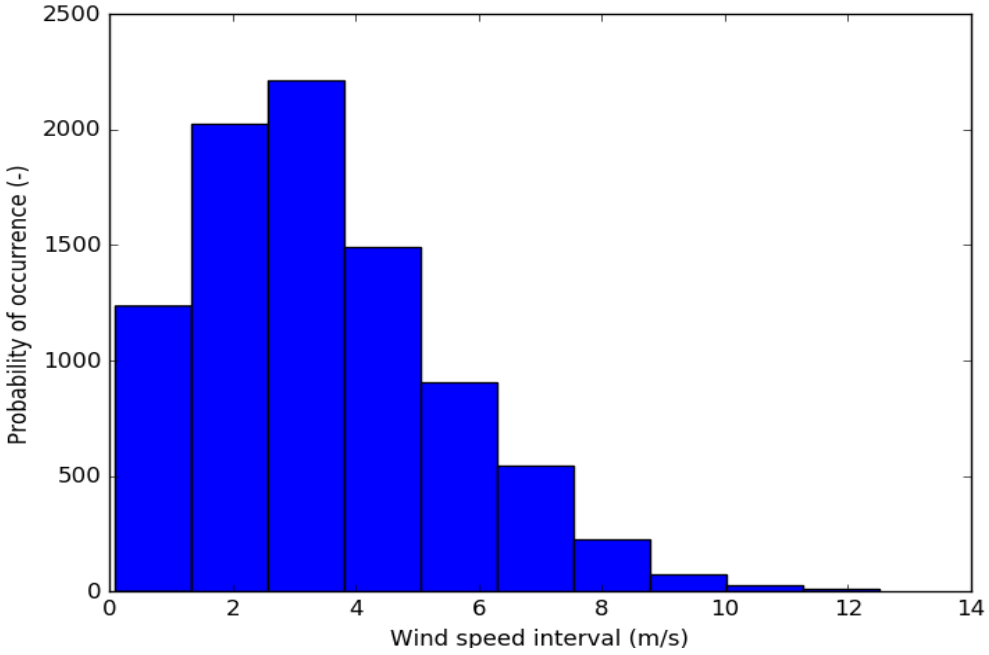

Figure 2.1: Frequency of wind speeds using TMY3 weather data from Meteonorm.

Most conventional plants currently use wet cooling technology i.e. evaporation cooling technologies, which require enormous amounts of water in the cooling towers. However it is very common for CSP plants to be planned in areas which are very dry

or arid. Water is usually scarce in these regions, and transporting water to these sites adds to the total expenditure and becomes an important factor. Hence dry cooling technology is considered for this study. The method of dry cooling is governed by dry bulb temperature. The dry bulb temperature, the wet bulb temperature and relative humidity are taken from the same dataset as DNI values.

2.3 Heliostats and the field layout

A heliostat, mounted on a pylon, directs beam radiation onto a receiver located on top of a tower (Stine and Geyer, 2001). Several mounting strategies exist but the most widely used heliostat type is the 'azimuth-elevation' concept (Björkman, 2014), which allows the heliostat assembly to move in the azimuth axis, while the elevation axis, which carries the mirrors, is directly above and orthogonal to the azimuth axis (Vant-Hull, 2012). Azimuth-elevation tracking systems use slew drives for the azimuth axis and have high costs. A 'slope-drive' axes arrangement using linear actuators for both azimuth and elevation axes are now being considered to save further costs without affecting the performance (Arbes *et al.*, 2016). For this study, the azimuth-elevation configuration is considered for the heliostats. In a given power tower plant, several heliostats are arranged in a collector field in a particular arrangement. These arrangements are reviewed and one arrangement for the heliostat field layout is then chosen.

2.3.1 Heliostat field Layout

Heliostats can be arranged surrounding the tower or on one side of the tower in such a way that there is minimum optical and mechanical interference from one another (Vant-Hull, 2012). A field with heliostats arranged surrounding the tower is called a surround field whereas a field with heliostats on one side of the tower is called a north/polar field. The arrangement of north fields depends on the geographical location of the field. Heliostats are arranged on the north side of the tower in the northern hemisphere while they are on the south of the tower in the southern hemisphere (Falcone, 1986). Several power towers with large capacities of 100 MW_e are being built. For such configurations, a surround field is considered suitable and is used for this study as well.

This is also in agreement with the findings of Yao *et al.* (2009) that north field configurations are better suited for power towers with small power output capacity. Figure 2.2 shows examples of a north and a surround field.

Figure 2.2: A north field used in PS-10 and PS-20 plants (Left) and a surround field used in the Gemasolar plant (Right) (Google Images, 2016).

There are four types of surround fields mentioned in the literature: Radial staggered, radial cornfield, a random field and phyllotaxis spiral (also called as biomimetic) arrangement (Lutchman, 2014). The radial staggered arrangement has proved to be very efficient in optimizing the field layout using the RCELL and DELSOL codes (Collado and Guallar, 2013). The biomimetic spiral pattern is used to create a layout which imitates a system in nature. For example, heliostats could also be arranged in a phyllotaxis given by the Fermat spiral equations just like florets are arranged on the head of a sunflower. The advantage of using such a layout is that heliostat packing density could be maintained even while moving away from the tower (Vogel, 1979).

Of all the layouts presented, recent studies have compared the widely implemented radial staggered layout with the biomimetic spiral pattern. The biomimetic spiral pattern is recommended as the most suitable layout for power towers as this layout is very efficient, maintains high heliostat density thereby requiring lower solar field area (Noone *et al.*, 2012; Zhang *et al.*, 2015a). A study by Ridley (1982) indicates that the normalized packing efficiency of a biomimetic field could be as high as 81 %. However, no plant till date has used this layout. A study on the design methodologies of different heliostat field layout designs and the impact on the power plant efficiencies states that biomimetic algorithms could be an alternative to the radial staggered pattern but concludes that radial staggered layouts offer very close or even better results (Mutuberria *et al.*, 2015). Considering the various points mentioned above, a radial staggered pattern is chosen for this study.

2.3.2 Radial staggered arrangement

The radial staggered arrangement for heliostats was first proposed by the University of Houston (Lipps and Vant-Hull, 1978) and is the most widely and commonly used algorithm for arranging heliostats and requires the least computing resources. This configuration uses two distinctive parameters – the azimuthal spacing between two heliostats in a row and the radial distance between two rows. These two parameters can be represented as a function of the characteristic dimension – the diagonal of the heliostat (Vant-Hull *et al.*, 1991). An additional advantage of using this arrangement is that established codes such as RCELL (Lipps and Vant-Hull, 1978), DELSOL (Kistler, 1986) and SOLERGY (Stoddard *et al.*, 1987) can be used to optimize the heliostat field layout. The tower height, the dimensions of the receiver and the heliostat field layout can be further optimized to get the lowest LCOE values (Sánchez and Romero, 2005). A radial staggered field layout is shown in Figure 2.3.

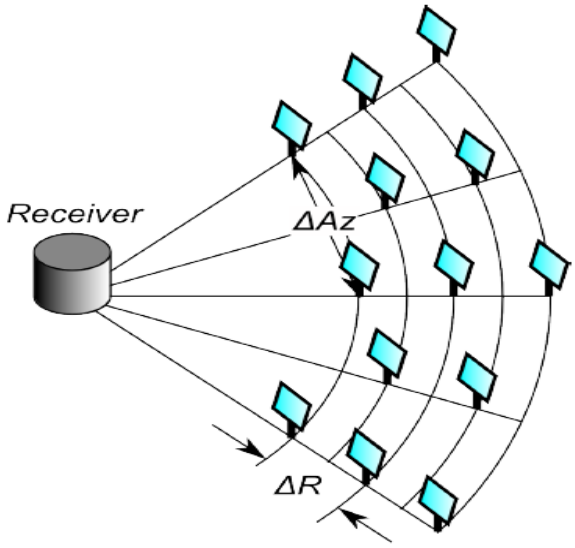

Figure 2.3: Radial staggered heliostat field layout where ΔR is the radial distance and ΔAZ is the azimuthal distance between the heliostats (Wagner, 2008).

The radial staggered arrangement for heliostats is optimized using SolarPILOT software where a set of potential positions for each heliostat is generated within the field boundary. SolarPILOT (Wagner and Wendelin, 2016) can be used to generate and optimize heliostat field layouts. The motivation for choosing this software and the modelling approach is described in § 6.1. The optical performance of the heliostat field

layout is evaluated by considering the position of each heliostat individually and estimating its annual performance. Optical efficiency parameters like the cosine, atmospheric attenuation; interception/spillage, blocking, mirror reflectivity and soiling losses are considered during the generation of the heliostat field layout. The radial staggered pattern uses the curve fits where the azimuthal and radial spacing is expressed as follows (Wagner, 2008):

$$\Delta R = (1.1442 \times \cot\theta_L - 1.0935 + 3.0684\theta_L^{\,2}) \times H_{helio} \tag{2.1}$$

$$\Delta AZ = (1.791 + 0.6396 \times \theta_L) \times W_{helio} + \frac{0.02873}{\theta_L - 0.04902} \tag{2.2}$$

where,

$$\theta_L = \frac{\pi}{2} - \theta_t \tag{2.3}$$

with θ_t as the angle between the vertical and the vector from the heliostat to the tower; H_{helio} as the height of the heliostat mirror and W_{helio} as the width of the heliostat mirror. The optimization algorithm and the generation of the field layout is explained in § 6.

2.4 Tower

The primary role of the tower is to hold the receiver. Other important uses of a tower are also to contain a buffer tank for storing the HTF (Augsburger, 2013) and to hold the optical targets (also called as beam characterization targets) below the receiver which is used for periodic calibration of individual heliostats (Malan, 2014). These targets are coated with a white paint and are designed to receive the flux of only one or two heliostats at a time (Stine and Geyer, 2001). The flux density distribution of the reflected beam from the heliostat is then measured for tracking accuracy. Figure 2.4: Different towers with their calibration target (Malan, 2014)Figure 2.4 shows various towers built by power tower developers with their calibration targets enclosed in dotted rectangles.

Figure 2.4: Different towers with their calibration target (Malan, 2014)

The tower also holds the piping system with proper insulation, which is essential to carry the HTF from the top of the tower and back. This ensures that heat losses by conduction from the tower and convection from the pipes to the surroundings are kept to a minimum. The tower must also be designed keeping in mind the costs (costs rise exponentially with the height of the tower); the shadow the tower casts on the heliostat field during operation and the landscape of the surroundings.

Considering the costs to build the tower, it is recommended that towers be made with reinforced concrete if the height of the tower is more than 120 m. A steel lattice tower is recommended when the height of the tower is less than 120 m (Kistler, 1986). The tower is characterized by its height and width and the fixed tower costs. These parameters are optimized using SolarPILOT in this study.

2.5 Receiver

The receiver in a power tower is made up of several panels. Adjacent panels then form passes and each sequential panel in a receiver is in a serpentine pattern (Augsburger *et al.*, 2016). These panels are made up of several vertical tubes which are welded to share a common HTF header The main purpose of the receiver is to convert the concentrated beam radiation into heat which is carried by the HTF flowing in the panels (Augsburger *et al.*, 2016).

There are several types of losses during this conversion: reflection of beam radiation from the receiver to the atmosphere, conduction losses, convection losses which depend on the ambient temperature and the wind speeds and radiation losses. Detailed thermal models of the receiver have been developed by Wagner (2008) and very recently using the concept of thermal resistance by de Meyer *et al.* (2016). The most widely used receivers used are the external cylindrical type or the cavity type and a review of these designs is presented by Ho and Iverson (2014). Since a surround field is chosen for this study, it makes sense to use an external cylindrical receiver.

The receiver is characterized by its height, diameter and the number of panels contained in it. These parameters (along with the aspect ratio and the maximum allowable incident flux) are optimized using the SolarPILOT software for this study.

2.6 TES system

TES systems are employed to shift the excess energy produced during times when solar availability is high to when it is low (Stine and Geyer, 2001). Commercialization of CSP plants with TES systems is now focusing on using molten salt as the heat transfer medium as well as the storage medium. This study assumes a power tower with a molten salt receiver with a 'two tank' system. Each tank has the capacity to hold the entire molten salt inventory. According to Helman and Jacobowitz (2014), the thermal storage capacity of the plant represents the total energy that is stored and is expressed in terms of MWh_t. The thermal capacity is often expressed in terms of the number of hours a plant can operate directly from storage when running at nominal capacity. A power tower with eight hours of TES in Upington will potentially be able to produce electricity during the peak demand hours from 16:30 to 21:30 in the night. Hence, eight hours of storage is considered.

2.7 Power cycle

The main role of the power cycle is to convert the thermal energy into electrical energy taking the losses into consideration: piping, storage, power cycle and the auxiliary losses (Augsburger, 2013). A power tower plant can be modelled with either a Rankine

cycle or a supercritical carbon dioxide (sCO_2) Brayton cycle. Recent research has shown that sCO_2 cycle is an attractive alternative to Rankine cycles for CSP and nuclear applications due to higher plant efficiencies and higher annual production (Dyreby *et al.*, 2014; Neises and Turchi, 2013). Supercritical carbon dioxide (the fluid state of carbon dioxide) has very high density when it operates near or above its critical point (304.13 K and 7.38 MPa) (Dostal *et al.*, 2004). This high density helps in reducing the size and the power of a compressor, thereby increasing the efficiency of the Brayton cycle and higher power density compared to a Rankine cycle. The sCO_2 cycle also rejects heat at relatively higher temperatures and is advantageous for using heat rejection strategies like dry cooling. This is important since CSP plants are suitable for dry and arid areas where there is a shortage of water.

All the above mentioned characteristics allow for smaller and more compact equipment with higher efficiencies (Iverson *et al.*, 2013; Mehos *et al.*, 2016). However, no power tower plant has yet been built with the sCO_2 power cycle. The Rankine cycle remains the most common and widely used cycle for power towers. With technological advancements, the cycle thermal efficiency (diagram efficiency, excluding parasitic losses) is expected to go up from 42.8 % in 2015 to 43.9 % in 2025 (IRENA, 2016).

The operating characteristics of a Rankine power cycle in a conventional power plant do not vary much. On the other hand, the power cycle in a CSP plant must take into consideration the daily and seasonal start-up and shutdown (Hirsch and Feldhoff, 2012), frequent changes in weather – clouds passing over the power plant, and varying HTF temperatures and flow rates (Wagner, 2008). These parameters are important for long term simulations as changes in these parameters affect the performance of the power block. A Rankine power cycle is chosen for this study.

2.8 Conclusion

The techno economic performance of a solar tower is assessed by modelling the conversion of solar radiation to electric power through the major components involved during this process: heliostat field, central receiver system and the power conversion unit (Augsburger, 2013). The heliostat field losses are first calculated: cosine, atmospheric attenuation, interception or spillage, shading and blocking efficiencies respectively. Next, the heat transfer losses from the central receiver tower system are calculated with molten salt as the heat transfer fluid. Finally, the losses due to piping,

storage and other auxiliary equipment are considered for the power conversion unit. The strategy for the plant operation and the design of the heliostat field layout should be modelled using a tariff structure. However, the tariff structure is not incorporated in the model for the generation and optimization of the heliostat field layout. Heliostats are sorted according to the power they deliver to the receiver at each hour. The efficiency of the external cylindrical receiver is calculated and a nominal cycle thermal efficiency is assumed in this study.

The plant operation is simulated on a single design point that is chosen as solar noon on spring equinox similar to a few other studies (Collado, 2009; Kistler, 1986). This point is chosen since the instantaneous power collected at this design point shows very little difference when compared with the annual average power (Collado, 2008a). The optical performance of the heliostat field is included and LCOE is used as the figure of merit to compare heliostats with different sizes.

3. Literature review

This chapter presents a brief overview of the literature reviewed for this study. The role and design considerations of a heliostat in a power tower plant are studied in detail. A short summary of the different heliostat designs developed since the early days of power tower development in the early 1970's is presented. Focus is then placed on the topic for this research: variation in heliostat size and the different approaches to lower heliostat costs conducted in the past. The method of heliostat design is then summarized with a view of how different components influence the size and cost of a heliostat.

3.1 Heliostats in power tower plants

Each individual heliostat in a collector field has the following components: A reflecting element which is usually a low iron glass mirror; drives; pedestal; foundation; support structures and wiring connections (Stine and Geyer, 2001). Sandwich mirror facets – with a first layer of thin glass mirror (thickness of 0.95 mm), a 'sandwiched' layer of polyurethane foam (thickness of around 28 mm) and a steel backward layer (thickness of 0.5 mm) are now being used instead of low iron glass mirrors (thickness of 3~4 mm) (Pfahl *et al.*, 2013). In addition to these components the heliostat field direct costs also include field wiring, labour, installation and transportations costs (Turchi and Heath, 2013).

During the design stage, several issues that must be addressed to maintain high optical efficiency of the heliostat are summarized by Spelling (2012) as follows:

- Reflectivity must be high
- Optical precision must be high
- Sun tracking must be accurate
- Structure must be resistant to loads

In addition to the design considerations mentioned above, wind loads have a radical impact on the costs of heliostats (Björkman, 2014). Hence, both strength and stiffness requirements are taken into consideration while designing heliostats (Blackmon, 2012).

Recent studies also emphasise the importance of carefully selecting the site specific design wind speed to park heliostats to the stow position (Emes *et al.*, 2015; Reeken *et al.*, 2016a) since it was observed that mean wind speeds for different sites differ throughout the year. Environmental aspects like blowing sand, dust and extreme temperatures also affect the design of a heliostat (Blackmon, 2013).

Other requirements like minimal environmental impact impose limits on field preparation and have a direct impact on the foundation of the heliostat. For example, the 'Ivanpah Solar Energy Generating System' plant in California had to plan a 'low impact pylon design' to allow the sites natural vegetation and contour to remain (BrightSource, 2014). Several countries also have their own codes for structural design and these must be taken into consideration for heliostat support structure design (Blackmon, 2015). For example, recently built CSP plants designed collectors using a design wind speed of 34 m/s in Spain. However, the Eurocodes increased this value to 38 m/s in Spain citing the extreme weather conditions these days. The wind speeds in South Africa are more severe (A collector designed for 40 m/s in South Africa experiences 38 % higher wind loads) than in several countries in Europe with lower design wind speeds (Balz and Reeken, 2015). All these design considerations indicate that heliostat design should take into consideration the geographical location and the environmental conditions of the site.

Several studies were made in the past to investigate methods to reduce heliostat costs; the most recent ones were in 2007, 2011, 2013 and in 2015 (Kolb *et al.*, 2007, 2011; Coventry and Pye, 2013; Pfahl, 2014; Pfahl *et al.*, 2015). It is therefore necessary to look at the history of development of heliostats including some unconventional designs in the recent past.

3.2 Heliostat development - History

Heliostat development began in the 1970's, primarily in USA, and continued into the 1980's. Figure 3.1 shows several design concepts that were developed during this development stage: Pedestal mounted azimuth elevation tracking heliostat in (a), bubble enclosed membrane in (b), ganged Heliostats in (c) and carousel type heliostats in (d). The general trend was to increase the heliostat size to almost 150 m^2 to lower the 'cost per unit area' which was used as a figure of merit to compare different heliostats. Shortly after the second generation heliostats came out in the early 1980's,

several other design variables were examined and emphasis was laid on heliostat size optimization.

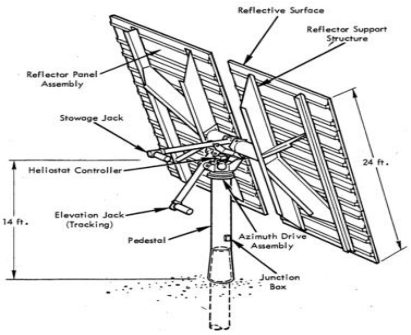

(a) Backside of pedestal mounted heliostat by McDonnell Douglas (General Motors Corporation, 1979)

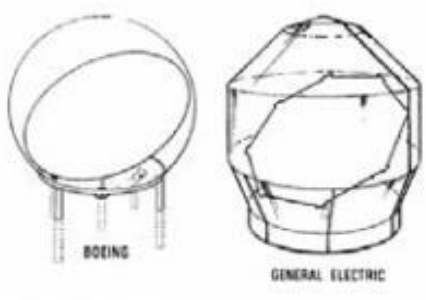

(b) bubble enclosed membrane heliostat (Kolb *et al.*, 2007)

(c) Mega ganged heliostat concept by DLR (Amsbeck *et al.*, 2007)

(d) 150 m^2 large carousel heliostat, PSA, Spain (Kolb *et al.*, 2007)

Figure 3.1: Heliostat design concepts

3.3 Variations in heliostat sizes

Heliostats that were used in the first power tower plants constructed had different sizes. At a later stage, heliostats also found use in a similar technology – Concentrating Photo-Voltaic (CPV) systems. CPV systems use an optical assembly to concentrate sunlight onto a small PV cell which converts the radiation into electricity. These cells can operate at higher irradiation levels than normal sunlight which is not concentrated (Stoddard *et al.*, 2006). Heliostats developed by Amonix for CPV systems were as large as 320 m^2. This trend of favouring larger heliostats is on the basis of the

assumption of several advantages of 'economies of scale'. For a given heliostat field, larger heliostats have fewer drives, foundations, pedestals and structural assemblies and are easier to operate and maintain when compared with smaller heliostats (Ulmer, 1998).

Heliostats in currently operational power tower plants are in the size range between 1.14 m^2, offered by eSolar in 2010, to about 140 m^2, developed by Abengoa in 2014. Figure 3.2 shows the variation in size between these two heliostats. Solar field construction costs still remain a huge challenge for large heliostats as they are assembled in a special purpose facility called Heliostat Assembly Building (HAB) (U.S. Department of Energy, 2013). However, the motivation behind eSolar's small sized heliostats were that they could be constructed and assembled in factories, thus had a huge potential to reduce labour costs on the field (Schell, 2011). eSolar further asserts that their newly developed 2.2 m^2 heliostats are still sufficiently small, can be installed manually and do not need a lifting device (Ricklin *et al.*, 2013), further reducing installation costs.

According to Kolb *et al.* (2007) and as cited by Landman and Gauché (2014), smaller heliostats with higher costs per unit area, but with better optical efficiencies result in the same LCOE values due to the lower tower height, area of the receiver and the number of heliostats. Another advantage with smaller heliostats is that relatively inexpensive linear electric actuators can be used to reduce costs (Buck *et al.*, 2010).

(a) 1.14 m^2 heliostat developed by eSolar (Google Images)

(b) 140 m^2 heliostat developed by Abengoa (Google Images)

Figure 3.2: Variations in heliostat sizes offered by eSolar (a) and Abengoa (b)

It is only very recently that 'cost versus heliostat size' has been taken into consideration and there is an indication in literature that the lowest life cycle costs might eventually be achieved by heliostat sizes larger than 50 m^2 (Kolb *et al.*, 2011). However, power tower developers and several R&D organizations like NREL, DLR and CSIRO

(Coventry and Pye, 2013) and STERG, are developing very small heliostats, all of which are less than 10 m^2. Since not many power tower systems have been installed and operated throughout the world, the optimum heliostat size might only be realized when more power tower systems have been installed and operated. Figure 3.3 shows the historical trend in the heliostat sizes and it can be seen that smaller heliostats are also being tested and experimented with since 2007.

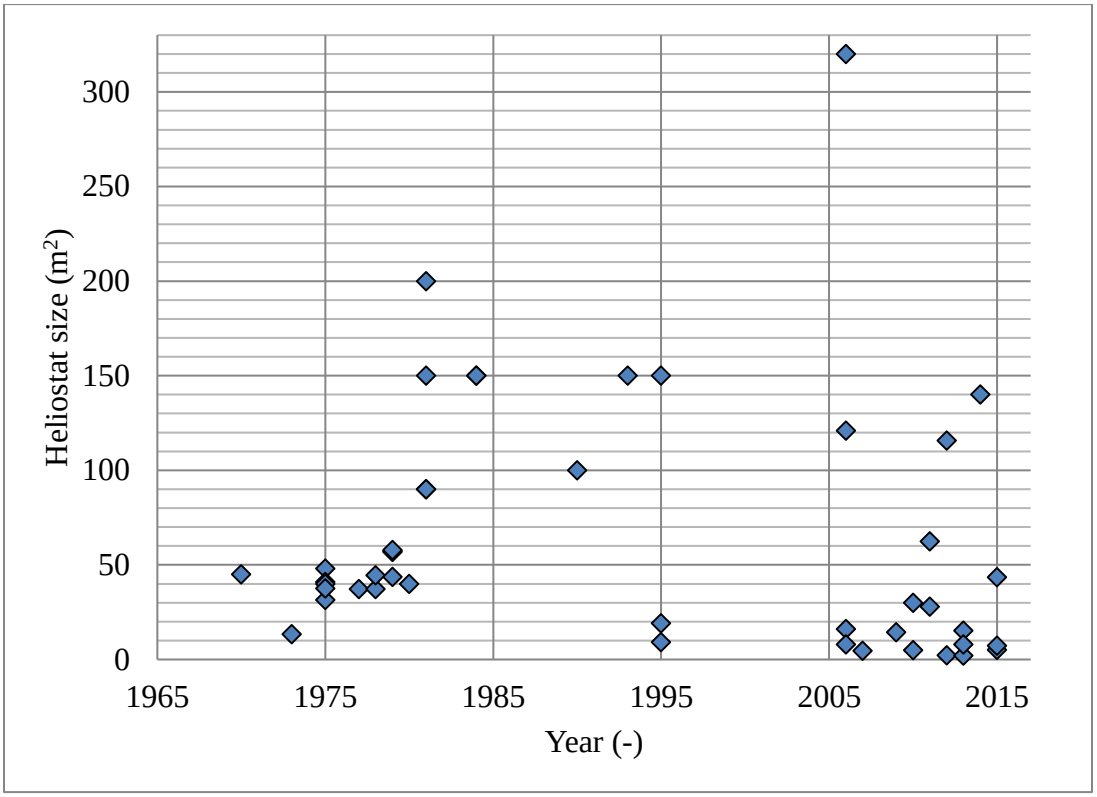

Figure 3.3: Historical trend of heliostat sizes (Lovegrove and Stein, 2012)

It is difficult to predict the optimum heliostat size for a power tower plant because of the huge variation in the sizes currently available in the market. According to a recent study, heliostats in the size range from 8 m^2 to beyond 100 m^2 were investigated, with all applicable costs taken into consideration and an optimum heliostat size of 40 m^2 was identified (Bhargav *et al.*, 2013). Another study gives a rough indication that optimum costs are achieved with 16 m^2 heliostats for smaller fields and 32 m^2 for larger fields. That study is based on the assumption that the maximum facet size is 8 m^2 (Pfahl *et al.*, 2015).

During the early period of heliostat development, costs for electronic parts were relatively high, and larger heliostats were expected to reduce the fixed costs per heliostat. Electronic costs have reduced considerably since then and smaller heliostats are being designed (Lovegrove and Stein, 2012). Figure 3.4 shows the path to developing low cost heliostats that was adopted in 1980's.

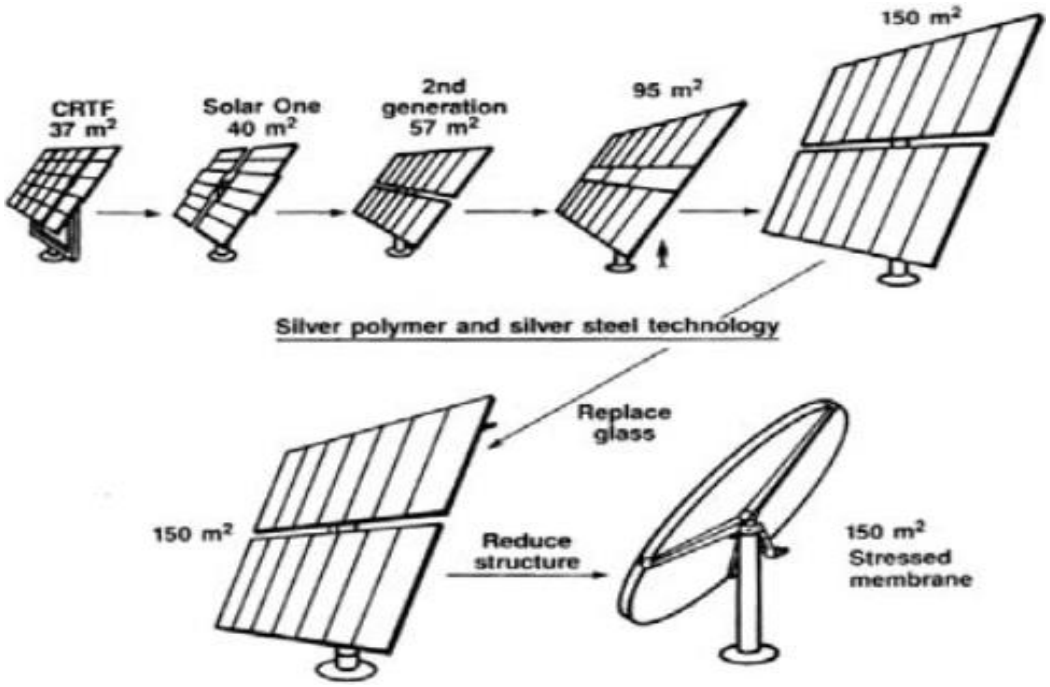

Figure 3.4: Heliostat size development in 1980's (Kolb *et al*., 2007)

3.4 Major heliostat cost reduction studies

Several studies, with different approaches, have investigated methods to reduce costs in the heliostat field in a holistic way. These studies are reviewed to get an idea about the different approaches used in the recent past.

A major study on this subject titled 'Heliostat Cost Reduction Study' was prepared by Sandia National Laboratories (SNL), USA, in 2007. This report had contributions from approximately 30 heliostat and manufacturing experts from USA, Europe and Australia. The results of this study evaluated the heliostat technology for the year 2006 and gave an estimated price of 126 $/m^2 (based on the material costs and costs of

deploying labour for ~ 600 MW power towers per year) (Kolb *et al.*, 2007). Further R&D was proposed to ultimately reach a price of 90 $/m^2. According to this study, optimal heliostat size will be more than 50 m^2.

Another study 'Power Tower Technology Roadmap and Cost Reduction Plan' also done by Sandia National Laboratories in 2011, indicated that the optimum size of heliostats was difficult to predict and suggested that optimal sizes will only be understood when more power tower systems have been installed. This report also explained that some of the main drivers for both large and small heliostats were drives (27-30 %), manufacturing facilities (23 %) and mirror modules (16-22 %) (Kolb *et al.*, 2011). This study noted that pedestal/mirror support structure and field wiring systems were relatively more expensive for smaller heliostats when compared to larger heliostats because of the number of heliostats.

A heliostat cost reduction survey conducted by Pfahl (2014a) suggests that cost reductions can be realized by decreasing or increasing certain variables in a heliostat sub function. The main heliostat sub functions considered are: reflecting sunlight, fixing shape of reflective material, connecting the system to ground, determining the offset of the mirror plane orientation and turning the reflective material around two axes.

Evaluating the life cycle costs for heliostat sizes, Bhargav *et al.* (2013) predict that the most promising heliostat size appears to be around 40 m^2. The main costs i.e. component, installation and operations/maintenance costs were included while arriving at this conclusion. The method used for this study is to initially consider a small heliostat and 'scale up' the size while optimizing for life cycle costs.

According to Coventry and Pye (2013), a few of the promising design concepts are the inclusion of wind fences that reduce both operational and stow condition loads, mirrors or sandwich facets with minimal auxiliary support frames and autonomous heliostats with wireless network communication provided alongside a PV power supply. Unconventional designs like those of Google (Google, 2013) are also reviewed.

4. Heliostat cost as a function of size

This chapter reviews the established trends between the size and the cost of a heliostat. Heliostat size categories are first defined for the small, medium and large heliostats. The importance of heliostat cost scaling relationships is justified as this is central to this study. This chapter also defines the heliostat cost size scaling relationship for the major subcomponent cost categories considered for this study: foundation, metal support structure, drives, controls, reflector panels and assembly.

4.1 Heliostat size categories

Heliostat sizes are categorized into three basic categories: large, medium and small. Large heliostats are assumed to be in the range of 60-150 m^2, medium heliostats in the range of 20-60 m^2 and small heliostats in the range of 1-20 m^2. These categories do not exist in literature and are defined for the sake of simplicity. Of all the heliostat sizes reviewed, very few heliostats have an area less than 10 m^2. However, since 2010 many heliostat developers are developing small heliostats. Figure 4.1 shows the heliostats (large, medium and small) considered for this study.

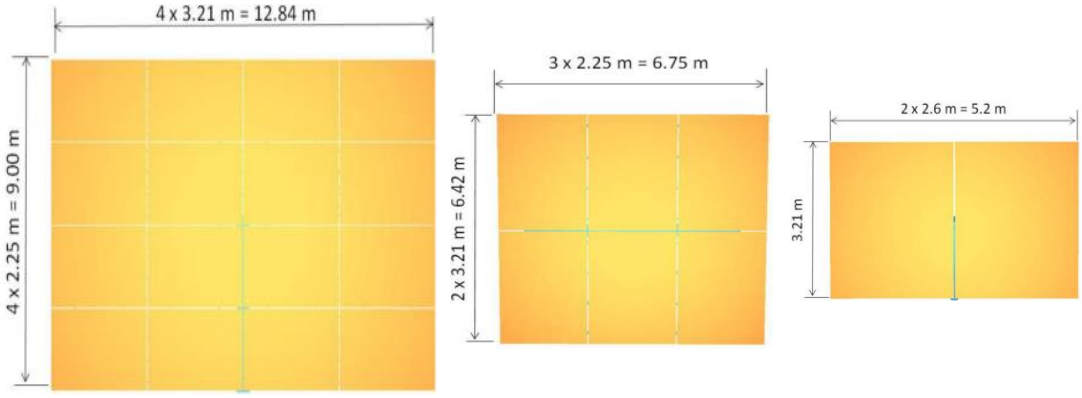

(a) Large heliostat (b) medium heliostat (c) small heliostat

Figure 4.1: A large, medium and a small heliostat considered for this study (Weinrebe, 2014)

4.2 Heliostat cost size scaling relationship

The size of a heliostat influences the subcomponent costs in several ways as labour; O&M costs and the price of the components vary for different heliostat sizes. Differences in design are recognized between small, medium and large size heliostats. The heliostat development program in the early 1980's in the United States favoured larger heliostats in order to lower costs per square meter ($/m^2). An assessment of power tower technology cost and performance conducted in USA indicated that the optimum heliostat size is 148 m^2 (Sargent & Lundy LLC Consulting Group, 2003). A similar analysis performed by DLR for European conditions also identified, among many others, the 'Megahelio' concept and indicated this value to be more than 200 m^2 (Pitz-Paal *et al.*, 2005). However, smaller heliostats are also being developed recently citing the fact that they have better optical performance than the larger heliostats. Hence, the objective of this section is to investigate the trends between the cost of heliostats and their sizes.

Cost scaling relationships are based on the length of the chord, area of the heliostat or in some cases, the number of mirror modules on a given heliostat (Jones, 2000). According to this study, for a given CSP power tower plant, the solar field with smaller heliostats will be smaller due to their better optical efficiency when compared with larger heliostats. However, the O&M costs for a solar field with smaller heliostats will be higher since the number of heliostats, the control systems and the number of personnel required for the plant is higher.

Additionally, the learning curve effect also plays a significant role in the manufacturing industry and was first described in 1936 with major emphasis on the time taken for making airplane parts (Wright, 1936). Learning curve effects have been used in several models to predict the decrease in costs (or time) with the increase in production volumes as workers in a manufacturing plant become more efficient (Nemet, 2006). These effects are important for smaller heliostats since there is a percentage drop in cost with doubling of each production. Apart from the heliostat area, heliostat costs are also dependent on the subsystem costs like drives and torque tubes. It is also important to note that learning curve effects for 'off-the-shelf' products are considered to be less than custom made products (Kolb et al., 2007).

4.3 Heliostat cost - area proportionality

Heliostat cost per unit for the three chosen sizes is calculated by considering the main cost categories of the heliostat: foundations, metal support structure, drives, mirrors, and assembly of the heliostat. To evaluate these costs, a reference heliostat with a conventional pedestal/torque tube structure and an azimuth/elevation drive configuration is selected from the literature. This heliostat is chosen in such a way that it is easily scalable and recent cost information for the main cost categories mentioned is available. For this reason, a medium sized heliostat with a total surface area of 43.33 m^2 is chosen as the reference heliostat for this study. The specific costs for the drives and mirrors for this heliostat are based on quotations and include overhead costs and profit. An additional 20 % is added to the remaining cost categories (foundations, metal support structure and assembly) to account for the business requirements of the component manufacturers (Reeken *et al.*, 2016b).

4.3.1 Foundation

The costs of the foundation depends on the soil conditions of the chosen site, pedestal diameter, the type of foundation (Reeken *et al.*, 2016b) and mass of material necessary to endure the design and operational wind speeds (Emes *et al.*, 2015). For the large and medium size heliostats, foundations are usually made by drilling a hole, inserting the pedestal and filling up the hole with a composite material like concrete. On the other hand, smaller heliostats can be directly inserted into the ground which does not require land levelling or using concrete foundations. This allows the natural contour and vegetation of the site to remain in the solar field and leads to lower costs. Requirements like ‘minimal environmental impact’ impose limits on field preparation and have a direct impact on the foundation of the heliostat. For example, the Ivanpah SEGS in California had to plan a ‘low impact pylon design’ so that the natural vegetation and contour of the site are not disturbed (BrightSource, 2014).

The soil in Upington, the site chosen for this study, is very hard and percussion drilling has been recommended (Reeken *et al.*, 2016b). For the three heliostat sizes, a foundation based on steel reinforced concrete pile is considered where the tubular steel pedestal is driven into the ground. The foundation costs C_f vary linearly with the

torque or moment imposed (Blackmon, 2012; Kusek, 2011). The imposed moment is proportional to $A_h^{3/2}$ and hence the foundation costs are expressed as a function of heliostat area A_h as follows (Blackmon, 2013):

$$C_f \propto A_h^{3/2} \tag{4.1}$$

4.3.2 Metal support structure

The metal support structure for glass-metal heliostats comprise of the tubular steel pedestal and the reflector support structure. The pedestal is made of galvanized steel and is hollow. The reflector support structure can either be a torque tube assembly or a truss structure. Large and medium size heliostats use hollow sections like purlins and girders while smaller heliostats may be built using stamped profiles mass manufactured in a production line (Reeken *et al.*, 2016b).

The load bearing component costs vary linearly with the moment imposed and thus are proportional to $A_h^{3/2}$. This relationship describes the ability of the heliostat to move and operate against design and operational wind loads and is considered to be an important criterion for the strength of the heliostat (Blackmon, 2012). This is shown to be true for both the reflector support structure and the tubular steel pedestal in uniform wind speed conditions (Blackmon, 2013). For this study, the metal support structure costs are expressed as a function of heliostat area as follows:

$$C_s \propto A_h^{3/2} \tag{4.2}$$

4.3.3 Drives

Heliostat costs depends on whether the drives used have a conventional azimuth-elevation or the slope drive configuration (Arbes *et al.*, 2016). A azimuth-elevation heliostat uses one slew drive and one linear drive, whereas the slope drive configuration uses two linear drives which are most cost efficient and reduce costs significantly (Reeken *et al.*, 2016b). Another factor that influences the drive costs is gearbox backlash (Kunert *et al.*, 2009). A wider backlash can lower costs as special measures

that must be taken for lower tolerances can be avoided. However, this can also result in lower annual optical efficiency. Hence, backlash must also be optimized.

A study by Jones (2000) indicates that the scaling of drive costs is proportional to heliostat area to the power between 0.56 and 0.65. An average value of 0.6 is used for this study and the cost of the drives is expressed as follows:

$$C_d \propto A_h^{0.605} \tag{4.3}$$

4.3.4 Control and communication

The cost of the control system for drives depends on the type of technology used. For large heliostat fields, a wired fieldbus can be deployed which includes the costs for the material, trenching and protection from lightning and rodents. However, these expenses quickly increase with the increase in number of heliostats and this is noticeable when the field has small or medium size heliostats (Pfahl *et al.*, 2015). The use of wireless technology is being investigated to reduce costs in the heliostat field.

This study assumes a wired control system as wireless systems have not yet been implemented in large heliostat fields. It is also essential to note that, the cost of several components in a wired control system is not a function of heliostat size. For example, the cost of controllers for heliostat logic and motor functions, position trip limit switches, encoders for position and instrument junction boxes do not vary with heliostat size. Augsburger (2013) indicates that control system costs are proportional to heliostat area to the power 0.2311 and hence are expressed as:

$$C_c \propto A_h^{0.2311} \tag{4.4}$$

4.3.5 Reflector panels

In the past, a reflecting panel was usually made up of a low iron glass mirror of thickness 3~4 mm. The performance of the reflector panels was improved by using a laminated polyvinyl butyral (PVB) film behind the coating of the mirror with a backing glass. The use of PVB lamination results in the use of thinner but highly durable mirrors with a very high reflectivity (Wang *et al.*, 2010). Sandwich mirror facets – with a first

layer of thin glass mirror (thickness of 0.95 mm), a 'sandwiched' layer of polyurethane foam (thickness of around 28 mm) and a steel backward layer (thickness of 0.5 mm) are now being used instead of low iron glass mirrors (Pfahl *et al.*, 2013).

The reflector cost per unit area essentially remains constant irrespective of the number of heliostats in the field or the heliostat size (Blackmon, 2012). Augsburger (2013) indicates that mirror costs are proportional to heliostat area to the power 1.042 and hence are expressed as:

$$C_m \propto A_h^{1.042} \tag{4.5}$$

4.3.6 Assembly

The assembly costs of a heliostat include the assembly of the heliostat sub-components into the structure, jigs and fixtures, transport from the heliostat assembly building (HAB) to the site, and the installation, checkout and reflector panel alignment (canting) at the site. The assembly in the HAB could be either done using robotic assembly or using manpower in an assembly line (Reeken *et al.*, 2016b). The costs for installation and canting at the site depend on the chord length, whereas the checkout depends on the duration it takes to ensure the precise calibration of the heliostat; these costs are therefore independent of heliostat size (Jones, 2000). The labour costs are included in this cost category as well, which is a function of the number of mirror modules to be installed in the field.

For this study, the assembly costs are assumed to be proportional to heliostat area to the power 0.4264 (Augsburger, 2013) and hence are expressed as:

$$C_a \propto A_h^{0.4264} \tag{4.6}$$

4.4 The way ahead

This chapter reviews the heliostat cost-size scaling relationships and defines the major cost components of a single heliostat. For further work, along with some major cost reduction studies, some unconventional designs by Google (Google, 2013), NREL (U.S. Department of Energy, 2013), DLR (Buck *et al.*, 2010; Pfahl *et al.*, 2015) and a few others are reviewed to identify the best possible solution to recommend the best suitable heliostat size. The Solar Thermal Energy Research Group (STERG) at Stellenbosch University has recently designed and reviewed 2 m^2 heliostat prototypes. This research is aimed at providing insight into low cost, low volume heliostats (Larmuth *et al.*, 2013). However, very small heliostats have not yet been implemented in utility scale power tower plants and therefore this study does not consider very small heliostats.

The total heliostat field costs of a given power tower plant also depends on the optical performance of the heliostat field layout i.e. fewer heliostats with better optical performance are required for the same system design. Several other key factors are essential to keep the capital costs low. The method of arranging the mirror facets i.e. using canting techniques, optical efficiency of the mirror facets, the annual solar field efficiency and O&M schedules are also important and are discussed in the next chapter.

5. Energy performance

The objective of this chapter is to study the energy performance of the power tower plant. The energy intercepted from the heliostat field is studied and the method of calculation of the major optical losses is presented in a radial staggered heliostat field layout. The method of calculation of the solar-to-thermal efficiency of the external cylindrical receiver is also presented.

5.1 Intercepted Energy from heliostat field

There are several quantities that control the thermal power transferred to the top of a receiver in a power tower plant. These quantities can be categorized as energetical, geometrical, and material (Collado, 2008a). Among these quantities, geometrical quantities can be estimated and summarized into one 'characteristic function' without major approximations (Leonardi and D'Aguanno, 2011). This characteristic function can be defined for a specific sun position as the effective surface area of all the heliostats, in a given field, that reflects the beam radiation onto the receiver. The geometrical quantities could relate to heliostat area or to ground area. Ground area is more useful while considering a multi-tower solar array (Schramek and Mills, 2003). However, a single tower is considered for this study. Figure 5.1 illustrates the losses that must be considered while evaluating the optical performance of a power tower.

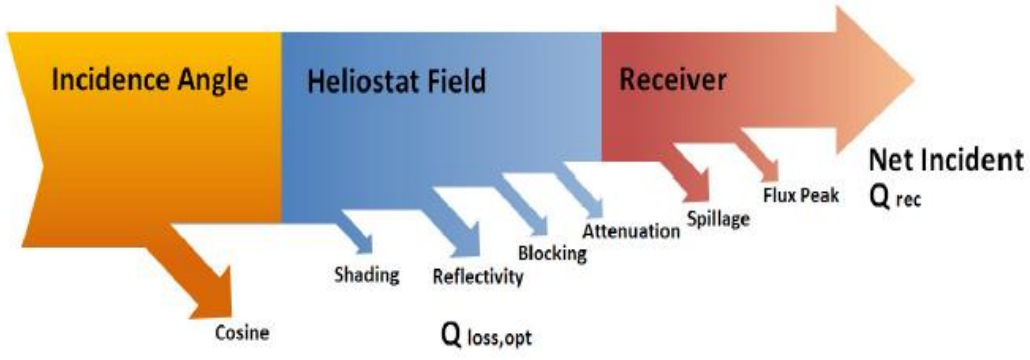

Figure 5.1: Optical losses in a power tower plant (Gertig *et al.*, 2013)

Leonardi and D'Aguanno (2011) provide a method to calculate the hourly intercepted energy at the receiver by multiplying the hourly DNI with the effective area of each heliostat in the field. It is assumed that each heliostat in the field has the same area. This method was used to develop and optimize solar field layouts in two other studies (Lutchman *et al.*, 2014; Scheffler, 2015).

The total hourly intercepted energy is expressed as follows:

$$I = A_h \times \sum_{H=1}^{8760} DNI_H \left(\sum_{i=1}^{N_{hel}} \eta_{c_{i,h}} \eta_{a_{i,}} \eta_{in_i} \eta_{s_{i,h}} \eta_{b_{i,h}} \right) \tag{5.1}$$

It is assumed that each heliostat in the field has the same area. The subscript H indicates the 'hour number' and the index i indicates the heliostat number with N_{hel} as the total number of heliostats. The subscripts c, a, in, s and b are related to the solar field efficiency and indicate cosine, atmospheric attenuation, interception/spillage, shading and blocking efficiencies respectively. These efficiencies are included in the characteristic function explained above including the co-ordinates of each heliostat in the field. Both mirror reflectivity and soiling factors are assumed. Figure 5.2 shows the nomenclature of the factors to be considered while evaluating at the optical performance of a power tower plant.

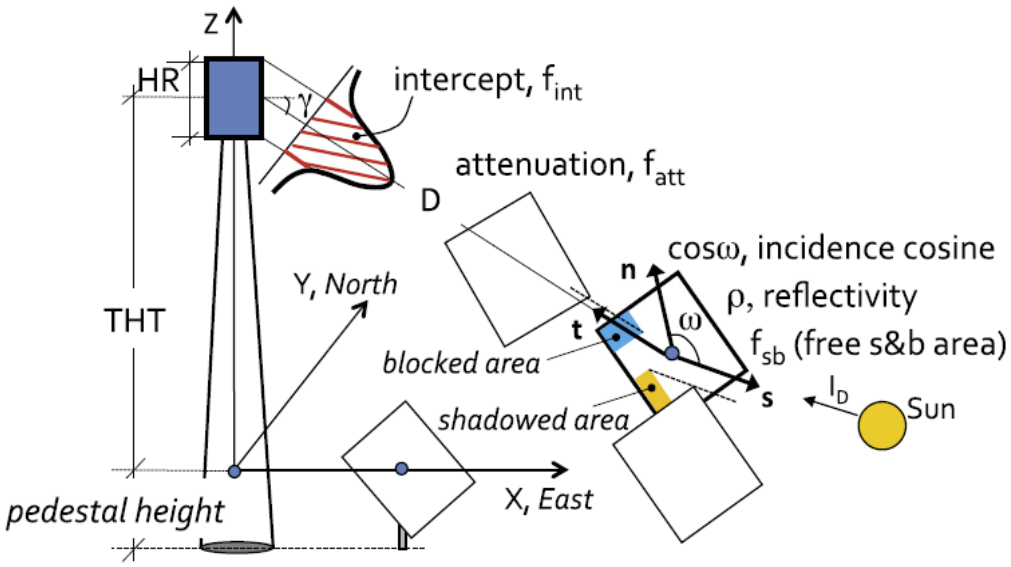

Figure 5.2: Optical efficiency factors in a power tower (Collado and Guallar, 2013)

5.2 Sun position

Collecting energy from the sun needs a good understanding of the position of the sun relative to the intended location or to be even more precise, the location of each heliostat. The tracking of a heliostat depends on the vector pointing from the heliostat towards the sun – the 'sun vector' (Lutchman, 2014). The sun vector has three components in the east, north and the zenith direction and the zenith angle and the solar azimuth angle must be calculated to find these components. Figure 5.3 shows the three components of the sun vector and the important angles to be considered: altitude angle α_Z, zenith angle θ_Z and the solar azimuth angle A.

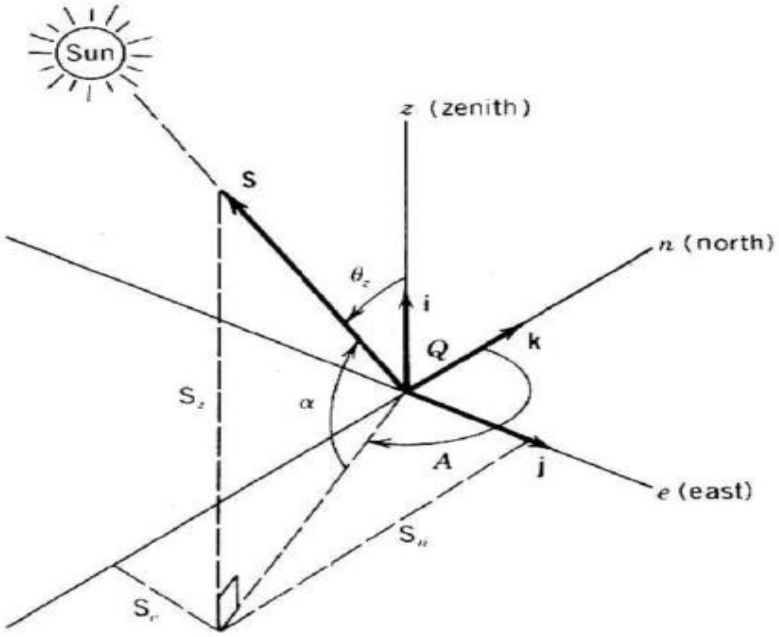

Figure 5.3: Earth surface co-ordinate system with respect to an observer standing at Q (Stine and Geyer, 2001)

The sun vector changes with each passing hour and in this study it is calculated using the method shown in the book "Power From The Sun" (Stine and Geyer, 2001).

Firstly, the solar time t_s can be calculates as follows:

$$t_s = LCT + \frac{EOT}{60} - LC - D \tag{5.2}$$

where LCT is the local clock time (preferably in a 24 hour format), EOT is the equation of time in minutes, LC is the longitude correction factor and D is the daylight savings time (not applicable to South Africa) in hours.

Secondly, equation of time (EOT) defined as "the difference between the mean solar time and the true solar time on a given date" can be determined in a process described by either Woolf (1968) or by Spencer (1971).

According to Woolf (1968), EOT in minutes can be expressed as follows:

$$EOT = 0.258\cos(x) - 7.416\sin(x) - 3.468\cos(2x) - 9.228\sin(2x) \tag{5.3}$$

where the angle x, in degrees, can be calculated as follows:

$$x = \frac{360(N-1)}{365.242} \tag{5.4}$$

where N is the day 'number' of the year, is the number of days since the first day of January taking into account if the year is a leap year or not.

According to Spencer (1971), EOT in minutes can be expressed as:

$$EOT = \begin{pmatrix} 229.2(0.000075 + 0.001868\cos(B) - 0.032077\sin(B) - \\ 0.014615\cos(2B) - 0.004089\sin(2B) \end{pmatrix} \tag{5.5}$$

where, the angle B, in degrees, can be calculated as follows:

$$B = \frac{360(N-1)}{365} \tag{5.6}$$

According to Iqbal (1983) the expression for EOT as given Spencer (1971) is sufficiently accurate (± 0.01 %) for engineering calculations and is used to calculate the EOT.

Thirdly, the hour angle, defined as "the angular distance between the meridian of the observer and the meridian whose plane contains the sun" (Stine and Geyer 2001), can be determined by the following expression:

$$\omega = 15(t_s - 12) \tag{5.7}$$

where, t_s is the solar time in hours and ω is in degrees.

Fourthly, the declination angle, described by Spencer (1971) can be determined as follows:

$$\delta = \frac{180}{\pi}\begin{pmatrix} 0.006918 - 0.399912\cos(B) + 0.070257\sin(B) - \\ 0.006758\cos(2B) + 0.000907\sin(2B) - 0.002697\cos(3B) \\ + 0.00148\sin(3B) \end{pmatrix} \quad (5.8)$$

By notation, δ is positive if the sun is north of the celestial equator and negative if the sun is in the south (Reda and Andreas, 2003).

Fifth, the zenith angle, the incident angle of the beam radiation on a horizontal surface, can be determined as follows:

$$\theta_Z = \cos^{-1}(\cos(\phi)\cos(\delta)\cos(\omega) + \sin(\phi)\sin(\delta)) \quad (5.9)$$

where ϕ is the latitude angle. By convention north of the equator is taken as positive. The zenith angle θ_Z and the solar altitude angle are complimentary angles, hence α_Z, in degrees, can be calculated as:

$$\alpha_Z = 90 - \theta_Z \quad (5.10)$$

Finally, the solar azimuth angle can be determined as follows:

$$\gamma_S = sign(\omega) \times \cos^{-1}\left(\frac{\cos(\theta_Z)\sin(\phi) - \sin(\delta)}{\sin(\theta_Z)\cos(\phi)}\right) \quad (5.11)$$

where, the sign function $sign$ is equal to +1 if ω is positive and -1 if negative.

The equations describing the sun position are sufficiently accurate enough for layout of heliostats in a field, but in case more accurate models are required, the sun position algorithm for solar radiation applications (Blanco-Muriel *et al.*, 2001; Reda and Andreas, 2003) are available for use in the literature.

The three components of the sun vector are in the east, north and the zenith direction. These components can be expressed in terms of either the zenith angle or the solar altitude angle as these two angles are complimentary angles. The vertical component is given by the cosine of the zenith angle (alternatively expressed as sine of the altitude angle). The sun vector and the three components can be calculated as follows (Gauché *et al.*, 2011):

$$\mathbf{s} = [S_{\mathrm{E}}\ S_{\mathrm{N}}\ S_Z]^{\mathrm{T}} \tag{5.12}$$

$$S_{\mathrm{E}} = \cos(\alpha_Z)\sin(\gamma_S) \tag{5.13}$$

$$S_{\mathrm{N}} = \cos(\alpha_Z)\cos(\gamma_S) \tag{5.14}$$

$$S_Z = \sin(\alpha_Z) \tag{5.15}$$

A heliostat is a two axis tracking system and most heliostats use the azimuth/elevation (Az-El) angle tracking, hence the importance of the solar Azimuth angle γ_S and the solar altitude angle α_Z. These angles are the tracking angles in the zenith and horizontal axis respectively. The next step is to calculate the target vector and the heliostat normal.

5.3 Target vector and heliostat normal

The target vector is the vector pointing from the heliostat to the tower (Lutchman, 2014) and can be calculated using the co-ordinates of the tower and the heliostat considered as follows:

$$\mathbf{T}_i = \begin{bmatrix} x_T - x_i \\ y_T - y_i \\ z_T - z_i \end{bmatrix} \tag{5.16}$$

where, the subscripts T and i represent the coordinates of the tower and the heliostat respectively. The unit vector of T_i is now obtained by dividing each component of the vector by its magnitude, which is given by:

$$\mathbf{t}_i = \frac{\mathbf{T}_i}{\|\mathbf{T}_i\|} \tag{5.17}$$

The heliostat normal is obtained by adding the sun vector and the target vector as follows:

$$\mathbf{N}_{i.h} = \mathbf{s} + \mathbf{t}_i \tag{5.18}$$

The unit vector for the heliostat normal is then given by:

$$\mathbf{n}_{i.h} = \frac{\mathbf{N}_{i.h}}{\|\mathbf{N}_{i.h}\|} \tag{5.19}$$

5.4 Cosine efficiency

A heliostat facet which is not normal to the sun, will not be able to reflect all the beam radiation falling on it and this radiation is reduced by the cosine of the angle between the collector normal and the sun. This effect is known as the cosine effect and is one of the major factors in the calculation of the annual optical heliostat field efficiency. The cosine efficiency of the heliostat field depends on the position of the sun and the relative position of each heliostat in the field with respect to the receiver (Collado and Turégano, 1989).

The cosine efficiency for a heliostat field can be calculated using the law of reflection (Noone *et al.*, 2012). When the heliostat tracks the sun, the collector normal bisects the rays of the sun and the line joining the heliostat and the receiver. Considering $\vec{S}$ as the unit vector pointing towards the sun and $\vec{t}$ as the unit vector pointing towards the surface of the receiver, the unit vector normal to the surface of the heliostat is expressed by Besarati and Goswami (2014) as follows:

$$\vec{n} = \frac{\vec{S} + \vec{t}}{\left|\vec{S} + \vec{t}\right|} \tag{5.20}$$

The cosine efficiency is then given as the dot product of the two vectors as shown in Figure 5.4:

$$\eta_c = \vec{n} \cdot \vec{S}; \;\; \theta = \frac{\cos^{-1}(S.t)}{2} \tag{5.21}$$

where, θ is the angle of incidence.

In this study, the cosine efficiency is modelled using the sun vector, the target vector and the heliostat normal. The results are compared and validated by SolarPILOT – an industry standard simulation tool useful for generating the layout of a heliostat field and optical characterization of power towers. Figure 5.4 shows two heliostats A and B on opposite sides of the field illustrating the cosine effect.

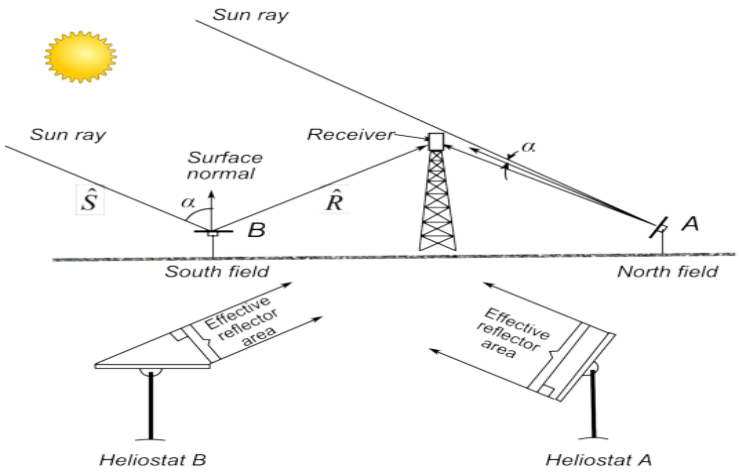

Figure 5.4: The cosine effect as seen on two heliostats A and B; A is placed in the North and B in the South (Stine and Geyer 2001)

5.5 Blocking efficiency

Blocking occurs when a heliostat blocks a neighbour's reflected beam radiation to the receiver (Huang *et al.*, 2013). Blocking is exclusively a function of the placement a heliostat with respect to the others in a given field. With increasing heliostat sizes, the effects of blocking increases and a trade-off between packing density and blocking effects must be the deciding factor (Srilakshmi *et al.*, 2015). The codes mentioned in § 6 can handle the calculations of the blocking effect. However, these calculations can be lengthy. Therefore an easy way to calculate blocking losses is important. Blocking losses can be calculated using the projections of rectangular heliostats in space (Cádiz *et al.*, 2015). This use of the radial staggered layout also simplifies the blocking losses of the heliostat field. For the radial staggered heliostat field layout the blocking factor can be calculated using the same nomenclature used by Collado and Turégano (1989) and expressed as follows:

$$f_b = 1 - \left[\frac{\Delta R}{H_{helio}} \left(\frac{\cos(\varepsilon_T) + \tan(\beta)\sin(\varepsilon_T)}{\cos(\theta)} \right) \right] \times \left[\frac{2f - (\sqrt{1+f^2} + ds)}{f} \right] \quad (5.22)$$

where, ΔR represents the radial distance between the adjacent rows, ε_T is the elevation angle of the heliostat, β is the slope of the field, f is the aspect ratio (width/height), θ is the angle

of incidence (described in equation (5.21)) and ds is given by the sum of the safety distance and an additional azimuthal separation distance.

The blocking efficiency is calculated using the blocking factor:

$$\eta_b = 1 - f_b \tag{5.23}$$

Additionally, a graphical method for 'no-blocking' heliostat field layout has been described by Siala and Elayeb (2001). According to this method, the minimum azimuthal distance between two heliostats in a row is twice the heliostat width. With an increase in the radial distance between the rows, the azimuthal distance continues to increase till a certain value is reached when it is reset again to twice the heliostat width. The position of the rows, are then determined so that heliostats that lie directly behind the next row are placed properly to ensure the 'no-blocking' effect (Wagner, 2015). Figure 5.5 shows that the beam radiation reflected by the lowermost part of the distal heliostat is not blocked by the uppermost part of the proximal heliostat. Each intermediate row does not contribute to the blocking losses. In this study, blocking losses are eliminated in the heliostat field layout using this method.

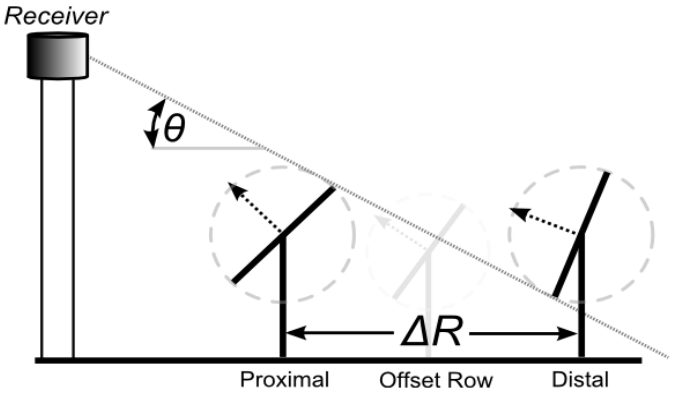

Figure 5.5: 'No-blocking' effect between two heliostats (Wagner, 2015)

5.6 Shading efficiency

Shading losses occur when one or more heliostats cast their shadow on a neighbouring heliostat. These losses, like blocking losses, are dependent on the placement of heliostats in the field and occur before the beam radiation hits the heliostat. These losses are highest when the sun is very low in the sky: in the early morning or in the

late evening. These losses can be obtained by projecting the polygons of the nearby heliostats on the heliostat considered in the direction of the sun (Augsburger, 2013). However, a few studies are of the opinion that shading losses are negligible as they occur during low sun angles and the plant is not in operation during these hours (Collado, 2008b; Falcone, 1986). Blocking efficiency is sufficient to get an idea about the annual efficiency trends and the final heliostat field layout. Furthermore, including shading losses could lead to a 'cascaded' loss in efficiency, where heliostats that would otherwise be excluded due to high blocking losses, shadow 'productive' heliostats and cause their removal from the field layout. Shading losses are not included in this study.

5.7 Atmospheric attenuation efficiency

The beam radiation reflected by the heliostat to the top of the receiver gets attenuated as the slant distance between the heliostat and the tower increases. Figure 5.6 illustrates this slant distance. With increasing heliostat field sizes, attenuation losses are estimated to be as high as 10 % when the heliostats are placed more than a kilometre away from the tower (Sengupta and Wagner, 2011). Atmospheric transmittance of the direct beam radiation and the losses have been approximated for clear and hazy days in several studies (Hottel, 1976; Kistler, 1986; Schmitz *et al.*, 2006), and more recently in (Tahboub *et al.*, 2013). These studies study the effect of atmospheric attenuation as a function of the distance between the heliostat and the receiver.

An analytical model has recently been proposed by NREL to account for the effects of atmospheric attenuation as a function of the measured direct beam radiation (Sengupta and Wagner, 2012). However, since different sites have different weather conditions, there is a difference between these models and the actual attenuation losses. According to Cardemil *et al.* (2014) these analytical models should be validated by actual experiments at the site as it was found that a heliostat field could be 4 % larger due to the water vapour in the atmosphere. However, this is difficult as obtaining ground measured data for a particular location for more than one year can sometimes be difficult.

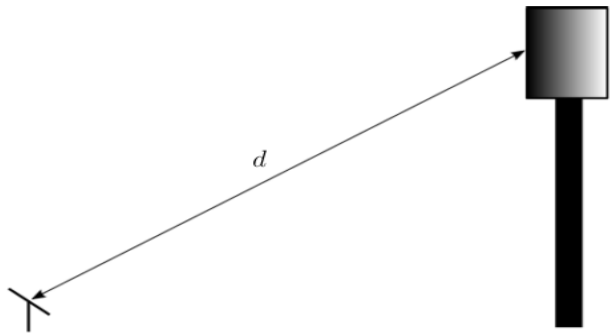

Figure 5.6: Slant distance between the heliostat and the receiver (Lutchman, 2014)

According to Noone *et al.* (2012), the difference between these models is less than 1 % in the visibility range on clear days. The atmospheric attenuation efficiency in this study is calculated using the widely used method discussed by Leary and Hankins (1979). This method is also in agreement with the model described by Pitman and Vant-Hull (1984) which is used for a visual range of 40 km. The atmospheric attenuation is calculated as a function of the slant distance, here expressed as d , between the chosen heliostat and the receiver:

$$\eta_a = 0.99321 - 0.0001176d + 1.97\times10^{-8}d^2; d \le 1000 \text{ m} \tag{5.24}$$

$$\eta_a = \exp(0.0001106d); d > 1000\,\text{m} \tag{5.25}$$

5.8 Heliostat reflection

In a power tower plant, mirrors are the first link in the conversion of energy from the sun to the electrical energy delivered to the grid. The shape of the mirror and the solar reflectance are of primary importance to estimate how beam radiation is concentrated and the amount of radiation reflected (Montecchi, 2016). According to Snell's law, the angle of incidence and the angle of reflection are equal for specular reflection and are measured from the surface normal at the reflected point. For heliostats, the surface normal on a point on the facet can deviate due to the optical errors like slope errors and improper tracking (Ulmer, 1998). This has an effect on the reflected image of the heliostat. Astigmatic aberrations (van Rooyen *et al.*, 2016) and accumulated dust on the mirrors (Heimsath *et al.*, 2016) also have an effect on specular reflectance. A value

of 0.95 is assumed for solar reflectance of the mirror and a soiling factor of 0.95 (Collado, 2008a). Hence the total optical reflectance of the mirror facets is taken as 0.9025.

5.9 Image interception/spillage efficiency

A part of the reflected beam radiation that falls outside the perimeter of the receiver aperture area is lost into the atmosphere and cannot be used for power generation (Lutchman, 2014). These losses, known as spillage losses, depend on the type of the receiver: external or cavity type. Since, an external receiver is considered for this study, only spillage losses for external cylindrical receivers are discussed. The spillage efficiency can also be calculated by estimating the size of the vertical and the horizontal elliptical image made on the receiver by the heliostat. This method is described in detail by Lutchman (2014) and the method and nomenclature is adapted in this study.

The spillage losses are calculated by determining how much larger the reflected image is than the receiver. The size of the reflected elliptical image is calculated as a function of the slant distance d and the largest dimension of the heliostat (width W_{helio} for the heliostat considered) and is expressed as:

$$D_{image} = d\lambda + W_{helio} \tag{5.26}$$

where λ is the angle subtended by the sun when seen from the surface of the earth and this value is taken as 9.3 mrad. This image is the one on the horizontal axis, whereas the vertical axis of the image depends on the heliostat-tower distance. The length of the vertical axis is obtained by dividing the size of the image D_{image} by the sinusoid of the angle between the receiver and the target vector (Lutchman, 2014):

$$L_v = \frac{D_{image}}{\sin(\varphi)} \tag{5.27}$$

where the angle φ is given by the following expression:

$$\varphi = \sin^{-1}\left(\frac{d_{xy}}{d}\right) \tag{5.28}$$

The area of the image is then calculated using the length and the width of the image as follows:

$$A_{total} = \frac{\pi}{4} L_v D_{image} \tag{5.29}$$

The difference in the length between the width of the receiver and the diameter of the image D_{image} is calculated and multiplied to give the spilled area. Similarly, the difference in the length between the height of the receiver and the length of the vertical axis L_v is calculated and multiplied with the diameter of the image to get the rectangular area which is spilled.

For the same dimensions, the area of a rectangle is larger than a rectangle by a factor of 1.273. Lutchman (2014) uses a value of 1.284 to account for the distortion of the elliptical area by using receiver and heliostat dimensions from an experimental case study. However, since this value cannot be currently verified, this same value is used. Figure 5.7 illustrates the elliptical image formed on the receiver which is used for calculating the spillage efficiency.

The total ineffective area is now given by the expression:

$$A_{ineff} = A_{ineff\ v} + A_{ineff_h} \tag{5.30}$$

where the ineffective areas are expressed as follows:

$$A_{ineff\ v} = \frac{(L_v - H_{rec})D_{image}}{1.284} \tag{5.31}$$

$$A_{ineff\ h} = \frac{(D_{image} - D_{rec})L_v}{1.284} \tag{5.32}$$

The effective image area is given by:

$$A_{eff} = A_{total} - A_{ineff} \tag{5.33}$$

The spillage/image intercept efficiency can now be calculated as:

$$\eta_{in} = \frac{A_{eff}}{A_{total}} \tag{5.34}$$

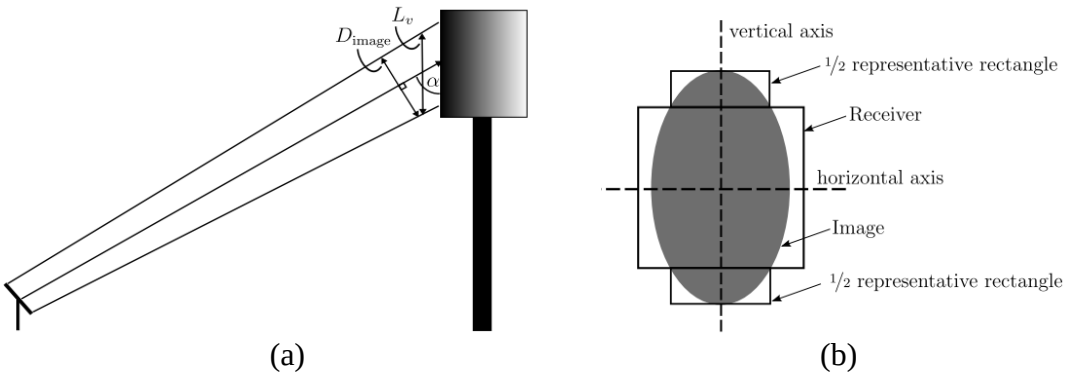

Figure 5.7: Representative rectangle used for calculating the spillage efficiency (Lutchman, 2014)

5.10 Receiver efficiency

According to de Meyer *et al.* (2016), the design of the receiver and heliostat aiming strategies play a crucial role in the heat transfer efficiency of the receiver. In a power tower, the receiver converts the incident beam radiations into heat energy which is then transferred to the HTF. This conversion process is mainly affected by losses due to reflection, radiation and convection. Conduction losses are small and hence can be ignored. The efficiency of the receiver η_{rec} can be calculated as follows:

$$\eta_{rec} = \frac{Q_{in} - Q_{loss}}{Q_{in}} = \frac{\alpha Q_{in} - \varepsilon \sigma A_{rec} (T_{wall})^4 - h_{mix} A_{rec} (T_{wall} - T_{amb})}{Q_{in}} \qquad (5.35)$$

where, Q_{in} is the incident power (W), Q_{loss} is the heat loss from the receiver system (W), α is the receiver thermal absorptance ε is the receiver thermal emittance, σ is the Stefan-Boltzmann constant (5.67×10^{-8} W/m^2/K^4), A_{rec} is total surface area of the receiver (m^2), T_{wall} is the average receiver surface temperature (K), and T_{amb} is the ambient temperature (K). The mixed heat transfer coefficient h_{mix} (W/(m^2/K)) is obtained by accounting for the forced and the natural heat transfer coefficients and is expressed as follows:

$$h_{mix} = \left({h_{fc}}^{a} + {h_{nc}}^{a} \right)^{1/a} \qquad (5.36)$$

where h_{fc} is the estimated heat transfer coefficient accounting for forced convection and h_{nc} is the estimated heat transfer coefficient accounting for natural convection. For an external receiver, a value of 3.2 is recommended for a, whereas a value of 1 is used for a cavity type receiver (Siebers and Kraabel, 1984).

Losses due to reflection can be as high as 10 % but are reduced to about 5 % when a black Pyromark® coating is applied on the external surfaces of the receiver panels (Pacheco, 2002). Hence receiver thermal absorptance α is assumed as 0.95. Considering a typical 100 MW_e power tower plant, the receiver thermal emittance is assumed as 0.88 (Ho *et al.*, 2014) for an average wall temperature as 873 K. The mixed convection heat transfer co-efficient is assumed to have a value of 10 $W/(m^2/K)$ (Christian *et al.*, 2015). By comparison, this value for the Gemasolar plant (with a smaller receiver area) is reported to be 16.1-19.3 $W/(m^2/K)$ (Collado and Guallar, 2016). The ambient temperature is assumed as 293 K (Christian *et al.*, 2015).

There is a certain level of uncertainty in the calculation of the receiver efficiency since most of the values in equation (5.36) are assumed. Hence, care must be taken in assuming these values, especially in the case of high wind speeds. For example, the receiver efficiency of the cylindrical receiver at the Solar Two power plant was reported as 88 % during periods of low wind speeds and 86 % during high wind speeds (Pacheco *et al.*, 2000). The receiver design–point thermal rating is first calculated in § 6.4.2 and then the optimized area of the receiver is calculated based on the receiver dimensions obtained using the SolarPILOT software. The solar-to-thermal efficiency of the external cylindrical receiver is calculated in Appendix A.

5.11 Summary

The energy performance of the power tower plant with the major optical and thermodynamic losses considered is described in this chapter. The energy intercepted from the heliostat field is calculated by considering the major optical losses. The receiver efficiency is then calculated by estimating the convection and radiation losses. To validate this optical performance model, the results are compared to an industry standard tool – SolarPILOT. This is done in the next chapter where the heliostat field layout is first generated and then the performance is simulated.

6. Heliostat field layout performance simulation

The design of the heliostat field layout and its optical characterization is very tedious and computationally expensive since many variables must be considered and then optimized. The variables include heliostat positions in the solar field, individual heliostat performance on an annual basis, the dimensions of the receiver used and height of the tower. Heliostats in power tower plants must also be placed in such a way that there is minimum optical and mechanical interference from one another. The optical efficiency of heliostats depends on the mirror surface slope errors and tracking errors. The optical characterization of a power tower plant also involves the precise calculation of the losses mentioned in § 5: cosine, blocking and shading, atmospheric attenuation and interception/spillage losses. The heliostat field operation strategy must also be kept in mind.

There are two methods of characterizing the optical performance of the solar field as categorized by Garcia *et al.*, (2008) and are based on the type of mathematical algorithms used. The first category is the Monte-Carlo Ray-Tracing (MCRT) method which uses a randomly chosen bundle of rays from one surface to another, with the surface irradiance proportional to the number of rays causing impact. SolTRACE (Wendelin, 2003a), MIRVAL (Leary and Hankins, 1979), HELIOS (Vittitoe and Biggs, 1977), STRAL (Belhomme *et al.*, 2009) and Tonatiuh (Blanco *et al.*, 2005) are examples of this category. These codes aid in the optical characterization but are not suitable to quickly generate and then optimize the field layout. The second category uses an analytical approach, where rays carry error cone information and the flux distribution is estimated using convolution of the Gaussian distribution functions (Georgiou *et al.*, 2013).

The codes, UHC (also known as RCELL suite) provided by University of Houston, (Lipps and Vant-Hull, 1980; Pitman and Vant-Hull, 1989), DELSOL3 by Sandia National Laboratories (Kistler, 1986) and HFLCAL developed by a German company called Interatom (Schwarzbözl *et al.*, 2009) are examples of this category. Even though these codes are advantageous because of their computational efficiency, only a few limited shapes of the reflected image can be modelled. Another method within this approach uses the truncated Hermite function expansion to describe the shape of the reflected image in two dimensions (Walzel *et al.*, 1977) and is the basis of DELSOL3 and RCELL suite.

Ray tracing methods have several advantages over codes based on convolution of the Gaussian distribution functions. Directional information, even after several reflections, is preserved. Additionally, several reflected image shapes can be modelled (Wagner and Wendelin, 2016) and that real photon interactions are replicated; hence providing more accurate results (Wendelin, 2003b). However, these codes are quite complex to use and require rather long computational time. Hence, research on finding a method for quick evaluation of the optical performance of power towers is quite active.

6.1 Modelling with SolarPILOT

A new approach to integrate both the analytical and MCRT methods where heliostat layouts can be generated quickly while using ray-tracing techniques is highly desirable. SolarPILOT, a tool developed at NREL is capable of integrating both these methods and can be used for generating heliostat field layouts, conducting a parametric study with different heliostat templates and optimizing the field layout. All these activities can be performed through a user friendly graphical user interface (GUI) (Wagner and Wendelin, 2016). Figure 6.1 shows the GUI of SolarPILOT along with the layout results of a 100 MW_e power tower plant in Upington.

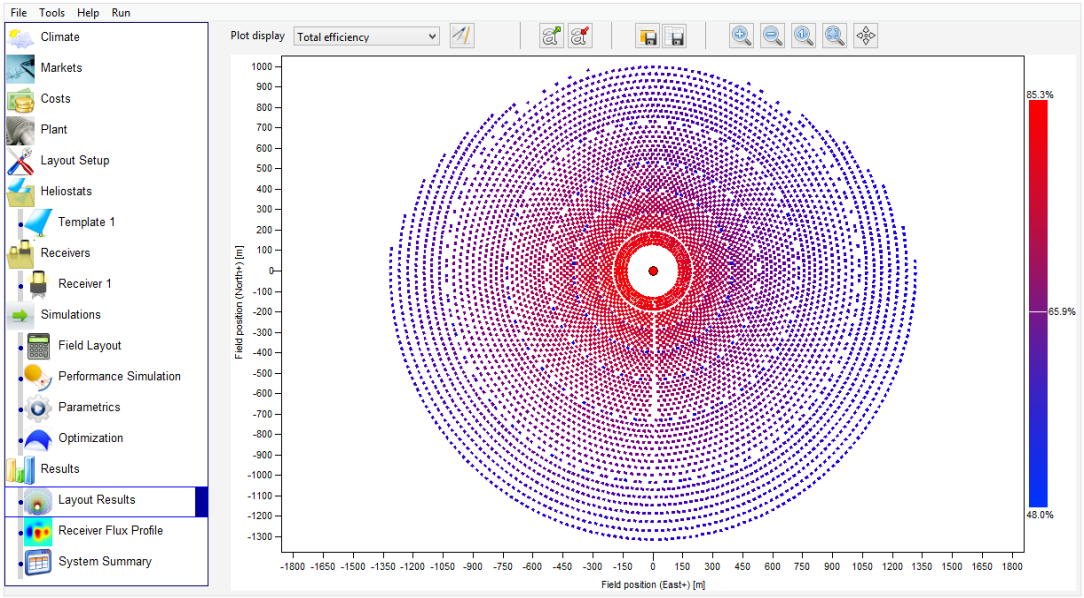

Figure 6.1: SolarPILOT layout results of a 100 MW_e power tower in Upington.

6.2 Model description

SolarPILOT uses the Hermite function and applies it to individual heliostats in a heliostat field. This approach differs from a previous approach, which was used by DELSOL3, which divides the heliostat field into several zones and evaluates the performance at the centre point of that zone (Wagner and Wendelin, 2016). Since every heliostat is evaluated, this could have a negative impact on the computation efficiency. Codes like DELSOL3 work well when the layout is symmetric i.e. when a radial staggered pattern is used. However, other approaches have reported higher land utilization, reduced land area and can include sensitive topographic features and uneven land features in the model (Sánchez and Romero, 2005; Wei *et al.*, 2010). Since each heliostat is evaluated in SolarPILOT, this has a negative impact on the simulation time. To alleviate this problem SolarPILOT uses several methods to lower simulation time and to improve the accuracy. The methods include: approximating the annual yield of a power tower using a subset of time steps over a year (instead of an annual simulation) and optimizing the receiver and tower dimensions through a chosen algorithm. Furthermore, land areas can be specified to be included or excluded from the layout and heliostats can be sorted based on the performance/cost ratio.

The computational speed is achieved by evaluating the components of the coefficients of certain parameters like sunshape, mirror geometry and optical errors of a heliostat only for the first time a simulation is performed. A mixed approach of calculating simple efficiencies like cosine and atmospheric attenuation by considering individual heliostats and a computationally expensive interception factor using the zonal method also reduces the computation time. Heliostat aim points are generated using analytical methods and a flux profile is generated using MCRT methods thereby integrating both the methods (Wagner and Wendelin, 2016).

6.3 Plant location and atmospheric conditions

Both the location of the plant and the atmospheric conditions influence the optimum heliostat field layout. The latitude dictates the annual path of the sun and the local atmospheric conditions affect both DNI and atmospheric attenuation. The ratio of the furthest distance in the south and the north directions from the tower can be defined as the south to north coefficient and is equal to 0 for a north field and closer to 1 for a

surround field. The latitude of the plant is quite significant in determining this ratio and gives an indication about which side of the field has a higher field density. **Error! R eference source not found.** summarizes the important details for the plant location.

Table 6.1: Details of plant location in the Northern Cape Province

Parameter	Description/value
Plant location	Upington
Time Zone	GMT 2
Latitude	-28.433 °N
Longitude	21.05 °E
Elevation	814 m

Apart from the location, the atmospheric conditions also play an important role in the generation of a heliostat field layout. A sunshape model, insolation model and the atmospheric attenuation model must be defined. A large number of sunshape models exist and a suitable one must be chosen for the model. An insolation model based on the position of the sun is helpful and helps in determining the DNI and other weather data during the layout simulation and must therefore be defined. An atmospheric attenuation model must then be defined to obtain the fraction of energy lost from each heliostat due to atmospheric scattering.

6.3.1 Design point DNI

The annual solar resource at Upington is relatively high when compared to other locations with operational CSP plants. From the TMY3 weather data (from Meteonorm), an annual DNI value of 2863 kWh/m^2 is observed. Figure 6.2 shows the histogram of beam irradiance in the region excluding the zero values. From the analysed weather data, a value of 950 W/m^2 is chosen as the design point DNI.

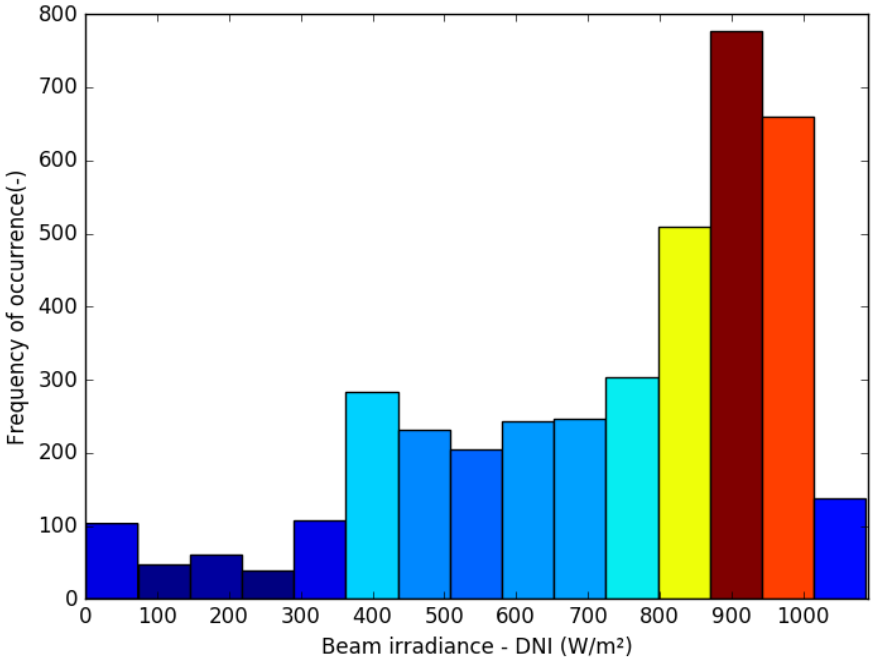

Figure 6.2: Histogram of beam irradiance in the region excluding zero values

6.3.2 Atmospheric conditions

Sunshape model

The sun is not a point source of light and in reality, the rays coming from the sun are not parallel (Meyen *et al.*, 2009). The sun's rays are emanated from a spherical outer shell called the photosphere with an approximate diameter of 1.39×10^9 m. This shell is the surface we see from the earth's surface and it appears as a disc. The disc appears to be brighter at the centre and this is known as limb darkened solar disc (Walzel *et al.*, 1977). The angle subtended by the sun's rays can be calculated using the earth-sun distance and the diameter of the photosphere. This angle is approximated as 0.533 degrees (9.3 mrad) (Stine and Geyer, 2001). Sun's rays could come from any part of the photosphere and pass through the earth's atmosphere. This essentially means that the rays reflected off the surface of a heliostat are not necessarily parallel and in turn may not intercept the receiver's surface (Ewert and Fuentes, 2012). In other words, these rays spread outwards due to this 'sunshape' error by the subtended angle of 0.533

degrees. Atmospheric scattering, precipitable water and the aerosol content increase this angle of spread (Biggs and Vittitoe, 1979).

Sunshape errors for several locations in the USA and Europe have been measured. However, little data is available at locations that are favourable for building and operating CSP plants (Wilbert and Geuder, 2013). Sunshape distributions have been described in detail by Buie *et al.* (2003). The sunshape errors for Upington are not yet available and therefore; the sunshape model in this study is assumed to be a 'limb darkened sun'. This model calculates the intensity of the sun as a function of the angular distance from the centroid of the sun's disc (Wagner, 2015).

Insolation model

The intensity of the beam radiation can be calculated by using several of the available models. Weather data models such as Meinel (Kistler, 1986), Moon (Vant-Hull, 1976), Hottel (Hottel, 1976) and Allen (Vant-Hull, 1976) approximate the DNI and other weather data based on the site altitude, solar zenith angle and the extra-terrestrial radiation. However, hourly weather data as a TMY3 form is available for Upington and is used for this study. This data is more suitable than the models mentioned above since it accounts for the weather variability at the specific site and the weather trends over the year (Wagner, 2015).

Atmospheric attenuation model

The atmospheric attenuation model governs the amount of energy attenuated which is reflected from a heliostat towards the tower. The attenuation increases with the increase in slant distance between the heliostat and the tower. The calculation for the atmospheric attenuation efficiency was presented in § 5.7 and is used for the evaluation of the optical performance of the developed solar field. The attenuation model used for the generation of the heliostat field layout using SolarPILOT is the 'DELSOL3 clear day' with a visibility of 23 km. The attenuation efficiency is calculated as a function of the slant distance d between the chosen heliostat and the receiver. This model also uses attenuation coefficients c_i with i ranging from 0 to 3. The atmospheric attenuation efficiency is expressed as:

$$\eta_a = \sum_{i=0}^{3} c_i \times d^i \qquad (6.1)$$

where

$c_0 = 0.006789$; $c_1 = 0.1046\text{km}^{-1}$; $c_2 = -0.0170\text{km}^{-2}$; and $c_3 = 0.002845\ \text{km}^{-3}$

6.4 Solar field layout method

The Solar field layout of the three fields is generated using SolarPILOT. The methodology used for the layout is as follows (Wagner, 2015):

- Potential heliostat positions are identified and placed within the field boundary. The positions are generated according to the heliostat field layout arrangement as described in § 2.3.1 (a radial staggered arrangement is used and losses due to blocking effects are eliminated) (Siala and Elayeb, 2001). Additionally, the minimum and maximum field boundaries are chosen to scale with the tower height H_t. The minimum field boundary is chosen as $0.75 \times H_t$ as recommended by Kistler (1986). The maximum field radius apparently has no limitation and a value of $20 \times H_t$ is recommended by Reeken *et al.* (2016a).
- The performance of each heliostat is simulated over the design points (listed in § 6.4.1) using the site specific weather data. For this study, the daylight hours from a subset of 12 days is simulated to achieve convergence and to take seasonal, daily and hourly weather variability into account.
- Heliostats are now sorted according to their 'performance-to-cost' ratio where the performance of each heliostat is measured according to the power it delivers to the receiver over the simulation set.
- Solar field performance is now simulated at the single design point chosen for the plant using the design point DNI (described in § **Error! Reference source not found.**). The design point can either be specified either by the sun position or the hour and the day of the year. Collado (2008a) concluded that there was only a 1-1.5 % difference between the rated power of the plant and the instantaneous power delivered by the solar field at solar noon of spring equinox multiplied by the total number of annual solar hours. Hence, solar noon of spring equinox is taken as the design point for the heliostat fields. This corresponds to a design point on 20th September and the day number is 264 considering Upington is in the southern hemisphere.
- The list of sorted heliostats is used to obtain the solar field layout. The least number of heliostats that can provide the solar field design power are selected for the layout.

6.4.1 Design point definition

A clear definition of the design points helps in the evaluation of the performance of the potential heliostats chosen for the field. Inclusion of the 'Time-of-day' (TOD) pricing is a way to improve the annual revenue of the plant by sorting the heliostats in the field so that the layout is more effective during the peak electrical price. Vant-Hull (2012) suggests that valuing sunlight proportionately to the TOD pricing before optimizing the solar field yields better layout results. TOD pricing has not been included in the generation and optimization of the heliostat field layout. Heliostats are sorted according to the power they deliver to the receiver at each hour as mentioned in Table 6.2. A total of 150 hours are simulated over the whole year.

Table 6.2: Design point considered for simulation

Day number (-)	Month of the year (-)	Day of the month (-)	Peak DNI (W/m^2)	Total DNI (kWh/m^2)	Hours simulated (h)
3	January	4	760.0	6.0	11
34	February	3	581.8	4.8	12
64	March	5	775.1	7.0	13
95	April	5	830.0	8.3	14
125	May	5	887.1	9.2	15
156	June	5	809.8	9.5	16
186	July	5	830.5	9.2	16
217	August	5	782.6	8.3	15
247	September	5	915.0	9.2	14
277	October	4	773.5	7.1	13
308	November	5	822.1	6.7	12
338	December	4	722.1	5.7	11

6.4.2 System design

The system design parameters help in defining design gross turbine output capacity W_{des} of the power tower plant. Power towers with a design net output rating of about 100 MW_e are increasingly being planned throughout the world and in South Africa; this value has therefore been used for this study. This is also in agreement with the condition that recent CSP projects awarded by the Renewable Energy Independent

Power Producer Procurement Programme (REIPPPP) in South Africa (Round 3.5 and 4.5) have a capacity limitation of 150 MW_e (Relancio *et al.*, 2016). The steps to obtain the solar field design power are as follows:

The receiver design–point thermal rating (also called as solar field design power or the design power block thermal input) Q_{des} is obtained by multiplying cycle thermal power Q_{cycle} and the solar multiple SM.

$$Q_{des} = Q_{cycle} \times SM \tag{6.2}$$

The cycle thermal power Q_{cycle} is obtained by dividing the design turbine gross output W_{des} by the cycle thermal efficiency η_{des}.

$$Q_{cycle} = \frac{W_{des}}{\eta_{des}} \tag{6.3}$$

The design gross turbine output W_{des} is obtained by dividing the design net output rating of the turbine W_{net} by the gross to net conversion factor r_{GtoN}.

$$W_{des} = \frac{W_{net}}{r_{GtoN}} \tag{6.4}$$

with r_{GtoN} = 0.875 (default value used by System advisor Model (SAM) (Blair *et al.*, 2014))

6.5 Heliostat models

As observed in § 3.3, there are heliostats with several sizes that are currently in operation in several power tower plants throughout the world. Heliostats with different sizes have different optical errors and hence different efficiencies (Weinrebe *et al.*, 2014). The optical efficiency of heliostats depends on the mirror surface slope errors and tracking errors. The slope errors can further be divided into errors due to shape (deformations due to self and wind loads), temperature, and assembly (Reeken *et al.*, 2016b). Tracking accuracies and the 'cost-area' scaling relationship must also be taken into consideration while increasing the size of a heliostat (Balz *et al.*, 2016; Kolb *et al.*, 2007). Hence, three different heliostats which are in the large, medium and small size

categories are compared against one another. Each power tower plant is considered with only one heliostat template i.e. only single heliostat geometry is used for the entire solar field.

6.5.1 Heliostat geometry

Figure 6.3 illustrates the geometry of a single heliostat which defines the active reflective area which is used to reflect the beam radiation to the receiver. The width of the heliostat is given by W_{helio}, the height by H_{helio} and the heliostat footprint diameter by D_{helio}. The gap length between the panels in the horizontal and the vertical dimension is defined by H_{gap} and W_{gap} respectively. Similarly, $N_{panel,h}$ and $N_{panel,v}$ represent the number of panels in the horizontal and the vertical dimension respectively. All these parameters are important for calculating the active reflective area for the heliostat.

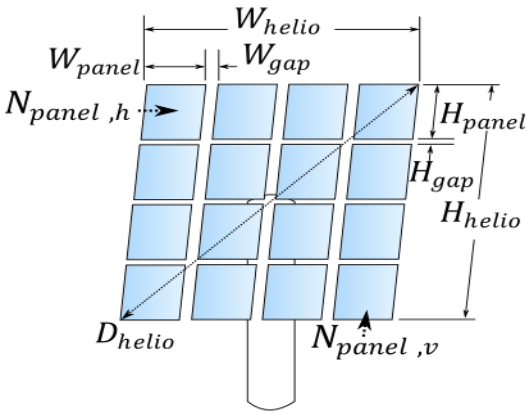

Figure 6.3: Heliostat geometry (Wagner, 2015)

The three heliostats from the large, medium and small category are chosen based on the level of commercialization, practicality and suitability of implementation in utility scale power tower plants. The heliostats are assumed to be rectangular in shape. Canting techniques determine the orientation of each facet and an 'on-axis' canting strategy (Landman and Gauché, 2014) is used throughout the analysis. Canting is often implemented for a particular tracking position or orientation and a distorted image is created due to astigmatism when the orientation changes.

The major design parameters required to evaluate the optical performance of the three heliostat field are listed in Table 6.3.

Table 6.3: Heliostat geometry design parameters (Weinrebe, 2014)

Heliostat geometry design parameter	**Large heliostat**	**Medium heliostat**	**Small heliostat**
Heliostat total area (m^2)	115.56	43.33	16.69
Heliostat height (m)	9.00	6.42	3.21
Heliostat width (m)	12.84	6.75	5.20
Heliostat footprint diameter (m)	15.68	9.32	6.11
Number of facets in the horizontal direction (-)	4	3	2
Number of facets in the vertical direction (-)	4	2	1
Individual facet dimensions (m)	3.21 × 2.25	3.21 × 2.25	3.21 × 2.60
Reflective surface ratio (-)	0.9583	0.9700	0.9200
Heliostat mirror reflective area (m^2)	111.40	42.03	15.36

6.5.2 Heliostat optical parameters

Optical losses can be due to several errors in a heliostat: tracking, sun shape, canting, swaying movements in a tower, gravitational bending due to structural and wind loads, mirror surface uniformity and alignment, azimuth axis tilt errors, etc. (Stone and Jones, 1995). The reflected image on the receiver at any given point of time may be described by a "single circular normal distribution of the energy flux" (García *et al.*, 2015) and can be expressed as:

$$F(x,y) = \frac{1}{2\pi\sigma_{tot}^{\ 2}} \exp\left(\frac{-\left(x^2+y^2\right)}{2\sigma_{tot}^{\ 2}}\right) \tag{6.5}$$

The image intercept/spillage losses can then be calculated by integrating the flux distribution along the receiver aperture plane as follows (Zhang *et al.*, 2015b):

$$\eta_i = \frac{1}{2\pi\sigma_{tot}^{\ 2}} \int_{x'}\int_{y'} \exp\left(\frac{-\left(x^2+y^2\right)}{2\sigma_{tot}^{\ 2}}\right) dy'\,dx' \tag{6.6}$$

In the equation above, the value σ_{tot} is known as total effective beam dispersion error, is expressed as a standard deviation (Monterreal and Heller, 1997) and is given by the convolution of the following Gaussian distribution functions: sun shape σ_{sun}, beam quality σ_{bq}, astigmatic effects σ_{ast}, and tracking errors σ_{track}. These factors are considered to be statistically independent of the effective beam dispersion error and hence are expressed using their combination as follows (Landman, 2013):

$$\sigma_{tot}^{\ 2} = \sum \sigma^2 = \sigma_{sun}^{\ 2} + \sigma_{bq}^{\ 2} + \sigma_{track}^{\ 2} \tag{6.7}$$

Sunshape

Sunshape errors are discussed in § 6.3.2.

Beam quality

The term 'beam quality' includes the statistically independent optical errors in a heliostat and is a specification that must be maintained during operational design conditions (Landman, 2013). Factors having a major influence on the beam quality have been described by Winter *et al.* (1991) as:

$$\sigma_{bq}^{\ 2} = \sigma_{sse}^{\ 2} + \sigma_{wl}^{\ 2} + \sigma_{gl}^{\ 2} + \sigma_{tl}^{\ 2} + \cdots \tag{6.8}$$

where the subscripts sse, wl, gl and tl represent surface slope errors, errors due to wind loads, gravitational loads and temperature loads. Other sources of error also include the errors due to contour bending and assembly errors. The slope errors are macro features (Wendelin, 2003b) and arise due to the deviation in angle of the collector surface normal from the profile desired (Landman, 2013). On the other hand, specularity errors are micro structure effects due to irregularities on the collector surface. These two errors can be expressed together as surface slope errors as (Wendelin, 2003b):

$$\sigma_{sse}^{\ 2} = 4\sigma_{slope}^{\ 2} + \sigma_{specular}^{\ 2} \tag{6.9}$$

The slope error can again be expressed as a function of several errors as (Reeken *et al.*, 2016b):

$$\sigma_{slope}^{\ 2} = \sigma_{shape}^{\ 2} + \sigma_{mirror}^{\ 2} + \sigma_{temp}^{\ 2} + \sigma_{assemb}^{\ 2} \tag{6.10}$$

where σ_{shape} represents the error due to deformations from self and wind loads, σ_{mirror} is the error due to contour bending, σ_{temp} is the deformation due to temperature and

σ_{assemb} is the error due to waviness in the surface of the mirror. All these errors can be dealt with in a single variable σ_{slope} (described in § 7.1.2) which is defined with respect to heliostat normal. The effect on beam quality is therefore doubled and is expressed as:

$$\sigma_{bq}^{\ 2} = (2\sigma_{slope})^2 \tag{6.11}$$

Figure 6.4 shows the slope and the specularity errors on a reflective surface where the standard deviation σ is expressed as a Gaussian distribution.

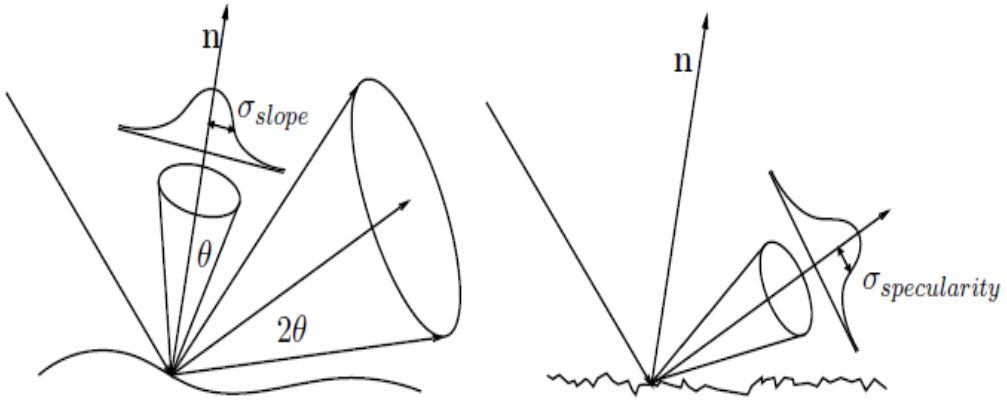

Figure 6.4: Slope(left) and specularity errors (right) on a reflected ray (Wendelin, 2003b)

Tracking

A heliostat with azimuth-elevation tracking is usually tracked with motors and hydraulic drives. The tracking errors could be due to the deviation in the mirror normal vector. These effects are multiplied due to gravitational loads or when the whole heliostat is in a wrong orientation (Ulmer, 1998). For large heliostats these errors are found to be in the range of 0.63-1 mrad (Collado and Guallar, 2013; Ulmer, 1998; Yellowhair and Andraka, 2013).

Schlaich Bergermann und partner (SBP sonne GmbH) have introduced a new heliostat with 'slope drive' configuration that allows their heliostat to continuously track the sun throughout the day unlike heliostats with azimuth-elevation tracking (Arbes *et al.*, 2016). They claim that the tracking errors are in the range of 0.4-0.6 mrad using this concept (Balz *et al.*, 2016).

6.6 Receiver

The receiver geometry is defined which gives an indication of the surface area available for absorbing the heat. It is important to reduce the surface area to lower the convective and radiative heat transfer losses. The optical properties are also defined which include the allowable peak flux at any point on the cylindrical surface which is important for operation of the receiver.

6.6.1 Receiver geometry

The receiver geometry of an external cylindrical receiver is characterized by the height and diameter of the receiver. The surface of the receiver consists of a number of rectangular panels which themselves contain several vertical tubes that carry the HTF. The diameter of these tubes must be designed keeping in mind the convection and radiation losses, molten salt pressure drop and velocity and the maximum metal temperature. The outer diameter values presented in literature are in the range of 20-45 mm (Lata *et al.*, 2006). The number of tubes per receiver depends on the receiver diameter. The area of the cylindrical receiver A_{rec} is a function of the height H_{rec} and the diameter D_{rec} and can be expressed as:

$$A_{rec} = \pi \times D_{rec} \times H_{rec} \tag{6.12}$$

The aspect ratio of the receiver is defined as the height of the receiver divided by the diameter and the recommended value is about 1.2 to 1.5 indicating a larger height. This helps in minimizing the spillage losses which improves the optical performance (Vant-Hull, 2002; Zavoico, 2001). The area of the receiver is optimized keeping the aspect ratio in mind.

6.6.2 Receiver operation

In a power tower plant, the receiver surface is subjected to a very high solar flux concentration. Due to the high temperatures that can be achieved, high flux gradients can exist between the external surface of the receiver and the outer and inner surfaces

of the material of the receiver (Salome *et al.*, 2013). These high temperatures when combined with an uneven distribution of thermal gradients could result in thermal stresses and potentially cause damage to the receiver in the long term (Grobler, 2015). Hence the receiver is typically limited to an allowable flux density (AFD). If the AFD is too low then the HTF is at a risk of freezing, which happened in the Solar II demonstration project. Conversely, if the AFD is too high, it could lead to a 'burnout' of the receiver panels resulting in premature failure of the receiver panels (Wagner, 2008). Christian *et al.* (2015) evaluated the design of a typical 100 MW_e power tower plant and the AFD was set at 1.1 MW/m^2. The same value is used for this study.

6.7 Performance simulation results

This section presents the performance results of the three heliostat field layouts. Each field layout is generated according to the method described in § 6.4, where heliostats are typically sorted according to the power they produce over the chosen simulation design points. Once the field layout is generated, the optical and thermal performance is calculated using a heliostat aiming strategy and specifying the flux simulation model: Hermite method (analytical) or SolTrace (MCRT). The solar field is then optimized to reduce the system's cost of energy where different values for the height of the tower, the receiver dimensions and heliostat positions around the receiver are explored (NREL, 2014). The heat losses due to convection and radiation in the receiver system and the piping thermal losses in the receiver/tower system are estimated and considered in the optimization of the solar field. The optimized field layout is then presented and the energy performance of the plant is simulated.

6.7.1 Optimization method

The heliostat field is the most capital intensive part of a power tower plant hence optimizing the field size is very critical for reducing overall costs. The optimization algorithm generates the best suitable layout leading to the lowest LCOE values. This is achieved by obtaining the maximum flux and minimizing the system losses. Each iteration in the optimization process makes a full layout and simulates the performance of that field. The optimization considers the capital costs, the energy performance

(optical and thermal) and the site specific weather data. Optimal values for receiver height and diameter and the tower height are investigated by the optimization algorithm which uses the design point thermal losses $Q_{loss,des}$ and the piping thermal losses Q_{piping} to calculate the design point thermal rating of the receiver Q_{des} :

$$Q_{des} = \alpha Q_{in} - Q_{loss,des} - Q_{piping} \tag{6.13}$$

where α is the receiver thermal absorptance and Q_{in} is the power incident at the receiver at any given time. The receiver thermal losses are due to convection and radiation losses and are calculated using the design point receiver thermal loss $Q_{rec,loss}$, the area of the receiver and polynomials that scale with incident power on the receiver and the wind velocity:

$$Q_{loss,des} = Q_{rec,loss} \times A_{receiver} \times \left(\sum_{i=0}^{3} C_{w,i} \times v_{wind} \right) \times \left(\sum_{i=0}^{3} C_{l,i} \times \frac{Q_{in}}{Q_{des}} \right) \tag{6.14}$$

where $C_{w,i}$ are the polynomials that scale thermal losses with wind velocity v_{wind} and are multiplied with the wind velocity raised to the corresponding power. On the other hand, $C_{l,i}$ are the polynomials that scale thermal losses with the ratio of power incident of the receiver at any time Q_{in} to the power indecent on the receiver at design point.

The piping losses are obtained by estimating a constant receiver loss $C_{piping,c}$ that is not dependent on the system geometry and the losses that scale with height of the tower and is expressed as follows:

$$Q_{piping} = C_{piping,s} \times H_{tower} + C_{piping,c} \tag{6.15}$$

6.7.2 Optimization algorithm

The optimization algorithm is used to generate the heliostat positions and to optimize the tower height, the receiver height and the aspect ratio. Several open source optimization algorithms exist and can be used for the optimization of the solar field layout. In this study, the Response Surface Generation methodology (RSGS) (Wu and Hamada, 2000) is used to generate and optimize the field layout. RSGS is an effective tool when the number of inputs in a system to be optimized are small and are all

quantitative (Wu and Hamada, 2000). Although the number of inputs involved in the optimization of a heliostat field is quite high the actual values to be optimized are very few, i.e. outer land boundary, the tower height, the receiver height and the aspect ratio. Furthermore, all these variables are quantitative.

The initial optimization step size determines the first step away from the initial estimated design points and is the total fractional departure for all the variables involved. A maximum number of iterations are used until convergence is achieved and the best suitable layout with the best objective function is achieved. The tolerance of the optimization determines whether the convergence is achieved, which happens when the objective function ceases to change by more than the tolerance during different iterations. A loose tolerance takes fewer optimization steps and the objective function might not be accurate, hence a tight convergence tolerance is used. The over-flux objective penalty factor is used to penalize the design when the flux intensity on the receiver exceeds the specified value of 1.1 MW/m^2. Table 6.4 shows the default optimization settings used by the built in RSGS optimization algorithm in SolarPILOT to generate the heliostat field layout.

Table 6.4: Optimization settings used to generate the heliostat field layout

Optimization settings	**Value**
Initial optimization step size	0.05
Maximum optimization iterations	200
Optimization convergence tolerance	0.001
Over-flux objective penalty factor	0.35

6.7.3 Field layout

The three optimized heliostat field layouts are generated and analysed. The figures [**Error! Reference source not found.**5, **Error! Reference source not found.**6 and REF _Ref458080051 \h **Error! Reference source not found.**7] show the optimized heliostat field layouts with large, medium and small heliostats respectively. The field also shows the efficiency value for each heliostat. The colour gradient sets the lowest efficiency value to dark blue and the highest value to bright red with a corresponding transition between these extreme values. The results of the optimization are listed in Table 6.5.

Table 6.5: Optimization results for the three heliostat fields

Optimization result	**Large heliostat field**	**Medium heliostat field**	**Small heliostat field**
Number of heliostats (-)	8131	21 670	55 544
Tower optical height (m)	171.9	168.8	156.9
Receiver height (m)	23.08	22.94	17.46
Receiver diameter (m)	17.99	17.24	16.28
Total reflective aperture area (m^2)	951 770	920 385	915 592

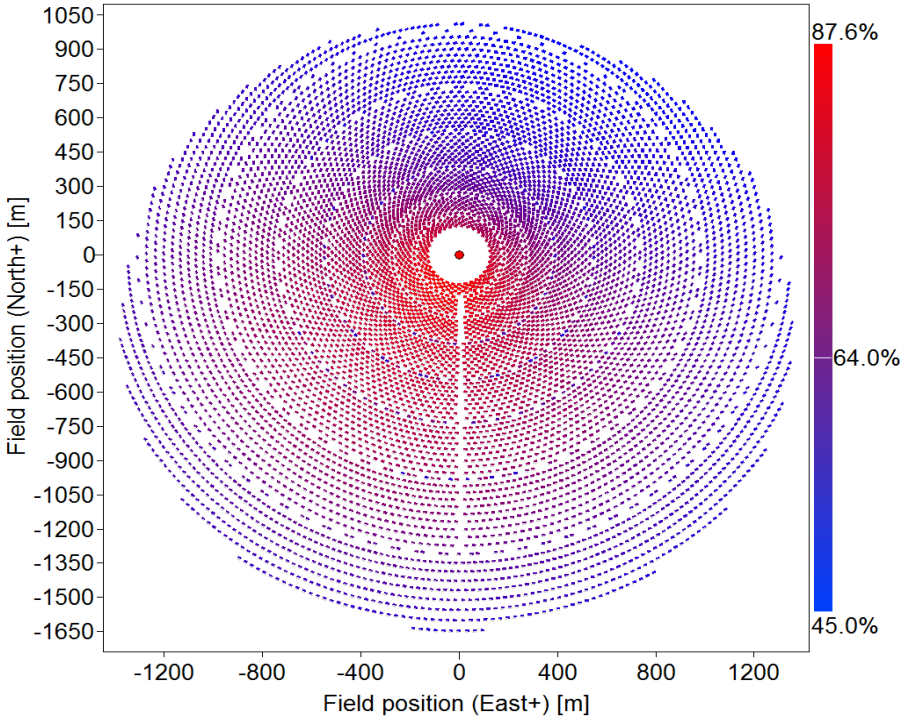

Figure 6.5: Optimized field layout with 8131 large size heliostats

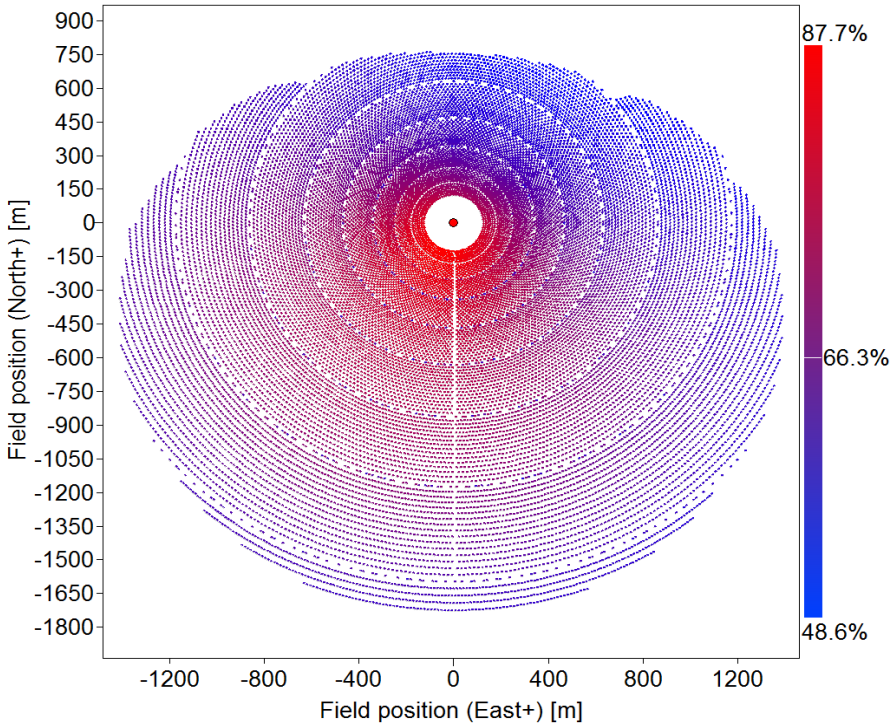

Figure 6.6: Optimized field layout with 21 670 medium size heliostats

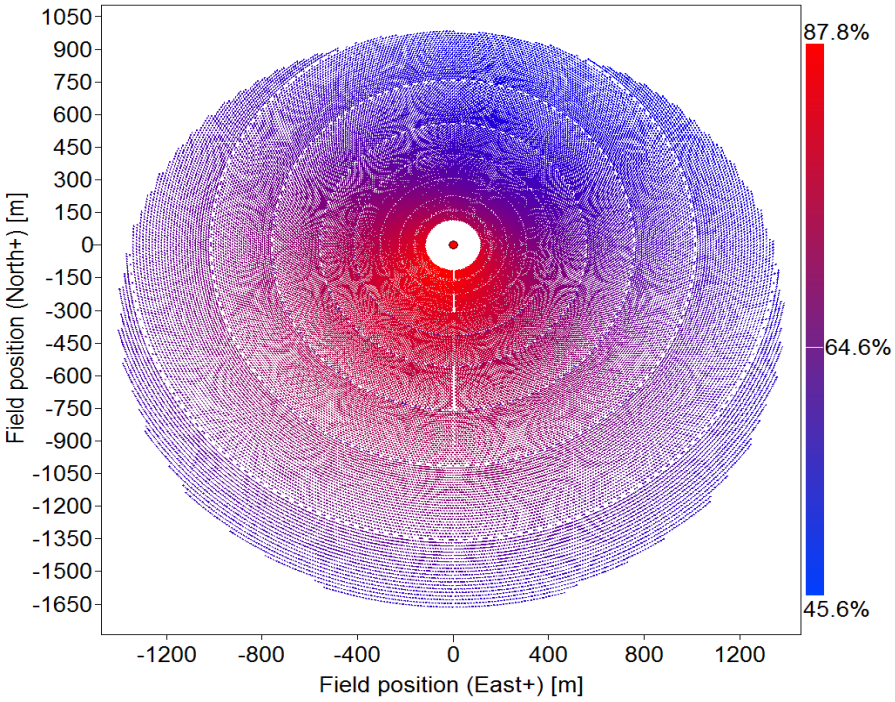

Figure 6.7:Optimized field layout with 55 544 small size heliostats

6.7.4 Performance simulation results – Model validation with SolarPILOT

This section compares the simulation results for the power tower plant optical performance model developed in § 5 with the results using SolarPILOT- an industry standard tool used for the generation and optical characterization of a solar field layout. The optical performance of the model was developed on Python software and the code is given in **Error! Reference source not found.**. The Hermite (analytical) method is u sed as the flux simulation model in SolarPILOT. The results of the performance simulated are then compared to validate the results predicted by the model. The optical performance model is developed for a 100 MW_e power tower plant in Upington with 8 hours of thermal storage (TES) and a SM of 1.8. This field with 8131 heliostats, each with a total area of 115.56 m^2, was simulated at solar noon, spring equinox. A mathematical formulation to eliminate blocking was enforced on the layout (Siala and Elayeb, 2001). Shading losses are not considered. The performance simulation results are listed in Table 6.6.

Table 6.6: Optical performance simulation results for solar noon, spring equinox, 2016

Optical performance result	**Model**	**SolarPILOT Hermite (analytical) method**
Cosine efficiency (%)	79.47	79.90
Blocking efficiency (%)	99.07	99.40
Atmospheric attenuation efficiency (%)	91.93	91.90
Heliostat reflection (%)	90.25	90.25
Interception efficiency (%)	97.53	96.10
Solar field efficiency (%)	63.702	63.302

The cosine and blocking efficiencies are slightly under-predicted by the model whereas interception efficiency is slightly over-predicted. The difference in the cosine efficiency values might be because 2016 is a leap year and there is a possibility of a small variance in the sun vectors of the model and SolarPILOT. The difference in the interception efficiency values are because of the different sunshape errors assumed by the model and SolarPILOT. The overall results indicate good agreement with the results obtained using the Hermite (analytical) method in SolarPILOT.

6.8 Optical performance results

Once the layout of the heliostat field is fixed, the performance of the three plants is simulated using SolarPILOT. The fields can be simulated by specifying the sun position or the hour/day of the year and in this study this is done using the latter i.e. on solar noon, spring equinox. Several heliostat aiming strategies exist for the cylindrical receiver (Grobler and Gauché, 2014). The heliostat aiming strategy is based on the 'image size priority' method where the aim position is determined by placing the heliostat image on the receiver at points of lowest flux. The size of the image determines the order in which the heliostat images are placed on the receiver, which indicates that heliostats which are further away from the receiver will first be chosen. The flux simulation model is based on the Hermite (analytical) method as described in § 6.2.

The optical performance results are influential while calculating the total reflective solar field area and in predicting the annual energy collected by the three heliostat fields. These parameters combined with the financial metrics are used in calculating the LCOE of the three plants. Table 6.7 shows the optical performance simulation results for the heliostat field layouts with large, medium and small heliostats.

Table 6.7: Optical performance simulation results for the three fields

Optical performance result	**Field with large heliostat**	**Field with medium heliostat**	**Field with small heliostat**
Heliostat area (m^2)	115.56	43.33	16.69
Heliostat count (-)	8131	21 670	55 544
Slope error (mrad)	2.60	1.18	1.50
Tracking error (mrad)	0.630	0.600	0.945
Total RSS error (mrad)	5.350	2.648	3.456
Cosine efficiency (%)	80.00	81.50	79.80
Blocking efficiency (%)	99.40	99.20	99.80
Shading efficiency (%)	100.00	100.00	100.00
Atmospheric attenuation efficiency (%)	91.90	92.00	92.00
Heliostat reflection (%)	90.25	90.25	90.25
Image intercept efficiency (%)	96.10	97.20	96.80
Solar field optical efficiency (%)	63.38	65.30	64.01

7. Economic Assessment

This chapter gives an overview of the total installed costs involved during the construction of the three power tower plants considered. These costs are categorized into direct and indirect capital costs. The costing model is adopted from the 2013 report 'Molten Salt Power Tower Cost Model for the System Advisor Model' to reflect the current state of art molten salt power towers (Turchi and Heath, 2013). The prices in the report mentioned above are indexed using 2012 as the reference year. However, the cost inputs for this study are indexed to the year 2015 using the Chemical Engineering Plant Cost Index (CEPCI) (CEPCI, 2015). The heliostat costs are calculated separately for the three different heliostat sizes considered and include the effects due to size scaling, learning curves and the price index. The annual operation and maintenance (O&M) costs are estimated separately.

7.1 Direct capital costs

Direct capital costs include the system costs for the heliostat field, the tower and receiver, thermal energy storage, steam generator, power block and site improvements. During the construction stages of the project, several uncertainties in the estimation of these direct costs cannot be foreseen. To account for these uncertainties, a contingency percentage is applied on the subtotal direct costs.

7.1.1 Heliostat field

The heliostat field costs include the capital required for site improvement and the heliostats including the foundation, steel supporting structure and pedestal, the drives and their controls, mirrors and assembly.

Site improvements

Site improvements are expressed as a cost per square meter of the total reflective area of the heliostat field A_{sf} and account for the preparation of the site. The activities included in this category are land levelling, laying roads and fences, storm water control system, infrastructure for water supply and blowdown evaporation pond. These costs can be very low when the heliostat field is not levelled as in the case of the Ivanpah SEGS plant. The total site improvement costs are calculated using the site improvement cost per square meter $C_s = 16$ \$/m^2 (Kurup and Turchi, 2015) and the total reflective area of the heliostat field A_{sf} as follows (Turchi and Heath, 2013):

$$C_{s,tot} = C_s \times A_{sf} \tag{7.1}$$

The three heliostat fields have different reflective area and hence have different costs for this category. The costs for the small heliostat are the lowest owing to the better optical efficiencies which result in a smaller heliostat field and reflective area.

Heliostat field costs

The heliostat field costs include the foundation, steel supporting structure, drives and controls, mirrors and assembly (including installation and checkout). These costs are estimated using a reference specific cost for a single heliostat. This cost is then multiplied by cost effects due to scaling factor s, volume effects accounting for learning curve benefits measured by a progress ratio pr, and a price index pi reflecting the changes in heliostat sub-costs over the years. The scaling effect deals with varying the heliostat sizes and is the ratio of the heliostat area under investigation A_h to that of the reference heliostat $A^0{}_h$ with s as the exponent.

Learning curve effects predict the decrease in costs (or time) with the increase in production volumes as workers in a manufacturing plant become more efficient (Nemet, 2006). These effects will be important for smaller heliostats as there is a percentage drop in cost with doubling of each production. These effects are accounted for using the progress ratio with the ratio of the current volume of production V_h and a reference volume $V^0{}_h$ as exponent. The price index is estimated for each cost category to reflect the latest costs. However, since latest price indices for 2016 were not available for heliostats, the prices are indexed to 2011. The total heliostat field costs $C_{h,tot}$ can therefore be expressed as a function of individual heliostat cost C_h and total number of heliostats in the field N_{hel} (Augsburger, 2013):

$$C_{h,tot} = C_h \times N_{hel} \tag{7.2}$$

where

$$C_h = C_0 \times \left(\frac{A_h}{A^0{}_h} \right)^s \times (pr)^{\log_2\left(\frac{V_h}{V^0{}_h}\right)} \times pi \tag{7.3}$$

with $A^0{}_h$ = 43.33 m^2 and $V^0{}_h$ = 21 500

In this study, the reference specific costs for a single heliostat are estimated for the three power tower plants considered. The heliostat considered for these costs is a medium sized heliostat with a total area of 43.33 m^2. The reason for choosing a medium heliostat is that heliostats can be scaled on either sides of the reference heliostat (medium to small / medium to large) while considering the appropriate reference volume production and costs. The reference specific costs for a medium size heliostat are shown in Table 7.1 along with the scaling factor, progress ratio and the price index.

Table 7.1: Heliostat subcomponent cost for a medium size heliostat (Weinrebe *et al.*, 2014).

Heliostat subcomponent cost	**Reference cost per unit ($)**	**Scaling factor (-)**	**Progress ratio (-)**	**Price index (-)**
Foundation	563.27	1.5000	0.9806	1.0816
Steel supporting structure	1303.08	1.5000	0.9900	1.8070
Drives	2030.54	0.6000	0.9400	1.3702
Controls	62.80	0.2311	0.9600	1.2841
Mirrors	491.81	1.0420	0.9700	1.0861
Assembly	701.98	0.4264	0.9800	1.0000

7.1.2 Individual heliostat optical improvement

The heliostat optical quality indicates the capability of a heliostat to reflect a circular and a specular image on the receiver surface. A high beam quality is desired and achieving this with an intelligent design is not possible beyond a certain point, for example, a higher quality material like a stiffer metal support structure is costly because of the higher assembly and erection procedures (Reeken *et al.*, 2016a). Instead of considering heliostat optical cost as direct cost, Augsburger (2013) recommends

calculating these costs separately to identify the importance of the heliostat optical variables. These costs are calculated using a single 'root-sum-square' (RSS) value which is 'bundled' which consists of the slope and the tracking error. The heliostat error of a medium sized heliostat is chosen as the reference heliostat error. This essentially means that a heliostat with a higher optical quality than the reference heliostat will not necessarily lower the LCOE due to the higher costs involved in achieving this optical quality. A negative value means that costs are saved. The heliostat optical improvement cost $C_{h,opt}$ is expressed as a function of the optical improvement cost per heliostat $C_{h,optic}$ and the total number of heliostats:

$$C_{h,opt} = C_{h,optic} \times N_{hel} \tag{7.4}$$

where

$$C_{h,optic} = 0.01 \times 10^{-3} \times \left(\frac{1}{\sigma_{rss}^{\ 2}} - \frac{1}{\sigma^{0}{}_{rss}^{\ 2}} \right) \times A_h \tag{7.5}$$

with $\sigma^{0}{}_{rss}$ = 3.4 mrad

7.1.3 Tower

The cost of the tower $C_{t,tot}$ is a function of the fixed tower cost $C_{t,fixed}$ and an exponential term which itself is a function of the tower cost scaling exponent k_t and the tower height H_t. The fixed tower cost serves as the base value for scaling costs of the tower with the overall height. The tower cost scaling exponent is a constant which determines how costs of the tower escalate nonlinearly with increasing tower height. The cost of the tower also depends on the material used for construction of the tower. A steel lattice structure is recommended for heights lower than 120 m and concrete beyond 120 m (Kistler, 1986). Since the height of the tower for all the three plants considered is more than 120 m, it is proposed that the towers be built with concrete. The total tower costs $C_{t,tot}$ can therefore be expressed as:

$$C_{t,tot} = C_{t,fixed} \times e^{k_t \times H_t} \tag{7.6}$$

where $k_t = 0.0113$ and $C_{t,fixed}$ = \$ 3 030 000

7.1.4 Receiver

The cost of the receiver depends on the area of the receiver and the type of receiver used. An external cylindrical receiver was proposed in § 2.5. The type of materials used and the selection of the heat transfer fluid also play an important role in estimating the costs of the receiver. The receiver cost $C_{r,tot}$ is calculated in a similar manner to that of the tower. The reference receiver cost $C_{r,ref}$ is multiplied by the ratio of the receiver area A_{rec} to that of the reference receiver $A^0{}_{rec}$. This ratio is subject to a scaling exponent k_{rec}. The receiver cost can now be calculated as:

$$C_{r,tot} = C_{r,ref} \times \left(\frac{A_{rec}}{A^0{}_{rec}} \right)^{k_{rec}} \tag{7.7}$$

with $A^0{}_{rec}$ = 1571 m^2 and $C_{r,ref}$ = \$ 102 100 000

7.1.5 Thermal energy storage

The TES system includes the tanks, piping, hardware costs and the storage medium. The storage system is an active direct system with two tanks for hot and cold storage. The storage medium chosen is solar salt (60 % $NaNO_3$ and 40 % KNO_3). The cost for TES system is a function of the storage capacity of the system, which in turn, is dependent on the number of full load hours of storage $N_{h,TES}$ planned for the plant. The rated cycle conversion efficiency η_{des} and the design turbine gross output also influence the storage costs. C_{TES} is the thermal energy specific cost per thermal kilowatt-hour of storage capacity and accounts for the cost of the equipment, installation and labour. The total TES system costs $C_{TES,tot}$ are given by:

$$C_{TES,tot} = C_{TES} \times \frac{N_{h,TES} \times W_{des}}{\eta_{des}} \tag{7.8}$$

with C_{TES} = 26 \$/kWh$_t$ (Kurup and Turchi, 2015)

7.1.6 Power cycle

The power cycle costs comprise the capital required for steam generation system (SGS), also called 'Balance of Plant' (BOP) and the power block costs. These costs are expressed per electric kilowatt of the gross capacity of the power block and take account of the equipment, construction, installation and the labour required for these systems.

Steam generation system

The main components of the SGS are heat exchangers for reheating, evaporation, preheating; steam drum and the pumps for circulation and transfer of hot salt. The total SGS costs $C_{SGS,tot}$ are given by multiplying the specific cost per electric kilowatt of the steam generation system C_{SGS} with the design turbine gross output.

$$C_{SGS,tot} = C_{SGS} \times W_{des} \tag{7.9}$$

with C_{SGS} = 340 \$/kW$_e$ (Kurup and Turchi, 2015)

Power block

The main component of the power block is steam turbine generator island comprising a steam turbine coupled to an electric generator. The major auxiliary systems for the power block are the systems for power distribution, water treatment, instrumentation and control, fire protection and water treatment. The total power block investment costs $C_{PB,tot}$ is calculated by multiplying the specific cost per electric kilowatt of the power block C_{PB} with the design turbine gross output of this configuration:

$$C_{PB,tot} = C_{PB} \times W_{des} \tag{7.10}$$

with C_{PB} = 1190 \$/kW$_e$ (Kurup and Turchi, 2015)

The subtotal direct cost of the plant $C_{d,s}$ can now be calculated by summing up the costs for the heliostat field, the tower and receiver, thermal energy storage, steam generation, power cycle and site preparation:

$$C_{d,s} = \begin{pmatrix} C_{s,tot} + C_{h,tot} + C_{h,opt} + C_{t,tot} + C_{r,tot} + C_{TES,tot} + \\ C_{SGS,tot} + C_{PB,tot} \end{pmatrix} \tag{7.11}$$

7.1.7 Contingency

The estimated cost for each category of direct cost calculated above i.e. heliostat field, the tower and receiver system, thermal energy storage, steam generation, power cycle and site preparation is subject to some uncertainties during the construction stage. Hence a contingency CP is added as a percentage of the subtotal direct costs. The contingency costs $C_{c,tot}$ are calculated as:

$$C_{c,tot} = C_{d,s} \times CP \tag{7.12}$$

with CP = 5 % (Reeken *et al.*, 2016a)

The total direct costs of the plant $C_{d,tot}$ can now be calculated by summing up subtotal direct costs and the contingency costs and is expressed as:

$$C_{d,tot} = C_{d,s} + C_{c,tot} \tag{7.13}$$

7.2 Indirect costs

Indirect costs generally cannot be identified with specific equipment or installation service. These costs include the costs for engineering-procurement-construction (EPC), purchasing land required for the plant and a sales tax applied as a percentage on the total direct cost.

7.2.1 EPC

The EPC costs account for the design and construction of the plant. Permitting, consulting, legal fees, site surveys, spare part inventories and costs for commissioning are some examples that can be included in this category. These costs are expressed as a percentage $EPCP$ of the total direct costs. The total EPC cost $C_{EPC,tot}$ can now be expressed as:

$$C_{EPC,tot} = C_{d,tot} \times EPCP \tag{7.14}$$

with $EPCP$ = 5 % (Weinrebe *et al.*, 2014)

7.2.2 Land

Land costs for the plant are the costs involved during the purchase of the land. The total cost of the land $C_{l,tot}$ is calculated by multiplying the total land area required A_l by the cost in USA dollars per total land area C_l. The land area is expressed in acres. For the three plants considered, the cost of land per hectare (ha) in the Upington region is assumed to be approximately ZAR 2730 (www.Landbou.com, 2016).

$$C_{l,tot} = C_l \times A_l \tag{7.15}$$

7.2.3 Sales tax

Sales tax is applied on a percentage of the total direct costs and is a one-time tax. Some countries like USA have a sales tax exemption on components which will be used for production of electricity from renewable energy sources. Currently, South Africa does not have this provision hence a sales tax is applied. The sales tax cost $C_{ST,tot}$ is a function of the sales tax rate STR and a percentage basis STB of the total direct costs and is expressed as:

$$C_{ST,tot} = STR \times STB \times C_{d,tot} \tag{7.16}$$

The total indirect costs of the plant can now be calculated by summing up subtotal indirect costs and is expressed as:

$$C_{i,tot} = C_{EPC,tot} + C_{land,tot} + C_{ST,tot} \tag{7.17}$$

The total installed costs of the power tower plant $C_{inst,tot}$ can now be obtained by summing up the total direct and indirect costs. Furthermore, an estimated total cost per net capacity $C_{net/cap}$ of the plant is found by dividing the total installed capacity of the plant by the design net output rating of the turbine and can be used as a reference for

comparison with other CSP technologies. It is important to note that this calculation is done using the total system rated capacity and not the gross power block rated capacity to reflect the actual energy delivered to the grid and to maintain consistency while reporting costs for utility generation technologies. The two financial parameters are expressed by the following equations:

$$C_{inst,tot} = C_{d,tot} + C_{i,tot} \tag{7.18}$$

$$C_{net/cap} = \frac{C_{inst,tot}}{W_{net}} \tag{7.19}$$

7.3 Operations and maintenance (O&M)

The operations and maintenance (O&M) costs for a power tower plant have been approached in several ways. Trieb *et al.* (2009) use an annual rate of 2 % of the total investment as the O&M costs. However, Blackmon, (2012) points out that the size and the number of heliostats have an effect on the annual O&M costs. This argument is based on the fact that even though the number of technicians and logistics personnel required for a plant is dependent on the size of the plant, this number will definitely go up for a field with a large number of heliostats. This logic is important in this study as the three fields considered in this study have a wide range of heliostat count: The heliostat field layouts with large, medium and small heliostats have 8 131; 21 670 and 55 544 heliostats respectively.

The O&M costs for this study are adopted from the model based on the study by Turchi and Heath (2013). This model assumes an O&M schedule which provides the maintenance and the consumable material quantities associated with the plant. This plant, with 8709 heliostats is used as a reference to develop the O&M costs for the three heliostat fields. However, the model uses a large size 144 m^2 heliostat. Hence a new method is developed to estimate the O&M personnel required for the heliostat field whilst considering the suggestions made by Blackmon, (2012) and Turchi and Heath (2013).

The new method estimates the number of instrument technicians and mechanical technicians (Machinist/welders) based on the number of heliostats in the field. Table

7.2 shows the solar field maintenance labour required for the three heliostat fields. The instrument and mechanical technicians are required to perform the heliostat field operations and hence the number of these personnel required varies. The number of maintenance supervisors and foremen and clerks/assistants is not changed as it is perceived that this number does not depend on the number of heliostats.

Table 7.2: Solar field maintenance labour

O&M personnel details	Reference heliostat field	Large heliostat field	Medium heliostat field	Small heliostat field
Area of each heliostat (m^2)	148.00	115.56	43.33	16.69
Number of heliostats (-)	8709	8131	21 670	55 544
Solar field reflective area (m^2)	1 289 000	951 770	920 385	915 592
Reference year (-)	2011	2015	2015	2015
Maintenance supervisor (-)	1	1	1	1
Maintenance Foreman (-)	1	1	1	1
Instrument technician (-)	2	2	3	5
Machinist/Welder/Mechanical technician (-)	2	2	3	5
Clerk/Assistant (-)	4	4	4	4

The following inputs are entered into the O&M cost model and a value for fixed cost by capacity ($/kW-year) and annual variable cost ($/MWh) is generated. These values are used in the calculation for the annual O&M costs and subsequently used in the calculation of the LCOE values. The annual O&M costs summary for the reference heliostat field and the three heliostat fields considered in this study is listed in Table 7.3 below.

Table 7.3: Annual O&M costs summary

Item	Reference heliostat field	Large heliostat field	Medium heliostat field	Small heliostat field
Fixed cost by capacity ($/kW-year)	72.00	67.00	68.00	72.00
Variable cost by generation ($/MWh)	4.00	4.00	4.00	4.00
Total annual costs ($)	10 643 479	8 107 845	8 266 131	8 546 940

7.4 Power tower cost break-up

The economic performance of the three power tower plants is estimated by breaking down the equipment costs. Figure 7.1 shows an example of the cost break-up of the total plant overnight installed costs. The major cost components are the heliostat field (25 %) and the power block (20 %). The cost of the land is almost negligible. Indirect costs are significantly higher for power towers due to the contingencies and additional risk premiums (IRENA, 2016) and this is confirmed by the cost breakup.

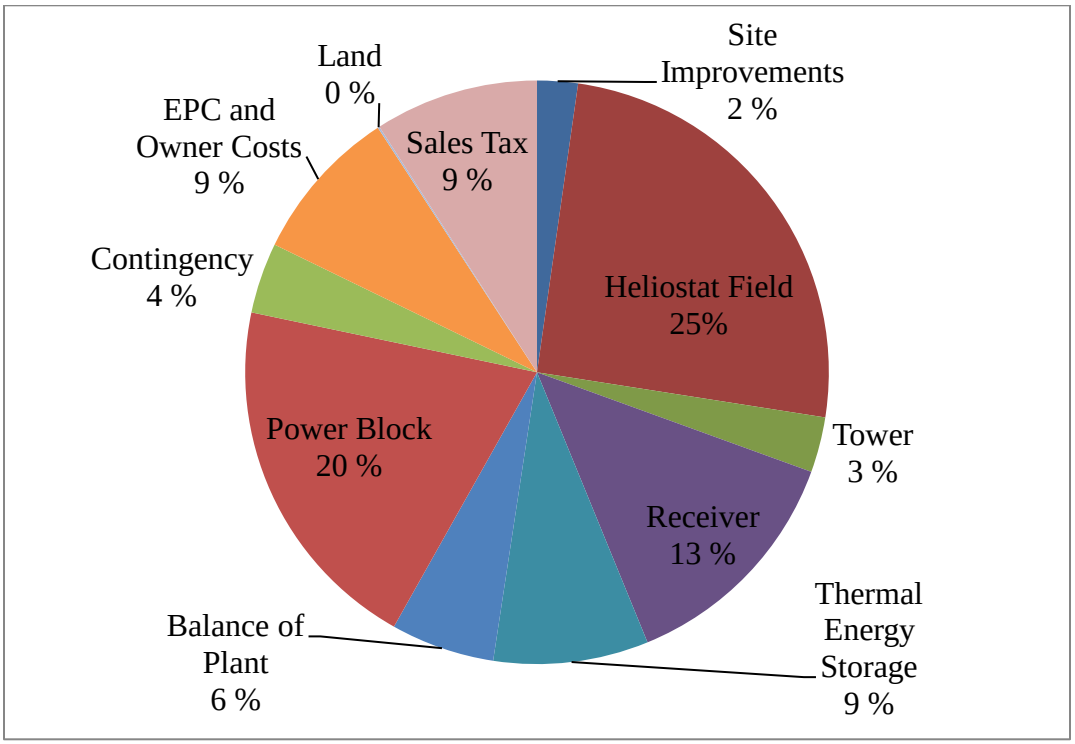

Figure 7.1: Pie chart of the heliostat field with large heliostat

8. Results - Thermo-economic performance and LCOE

In this section, the energy performance model of the power tower (described in § 5 and § 6) and the economic assessments (described in § 7) are combined for the power tower plant using primary or derived indicators. Primary units provide knowledge about quantities like the annual electrical energy generated or the total installed cost of the plant. These units are measured in single units (e.g. annual electrical energy generated in kWh_{el}) and give an idea about the size of the plant. On the other hand, derived indicators evaluate qualities of both the energy and the capital conversion, such as LCOE or the solar to electric efficiency (e.g. LCOE in $\$/kWh_e$) (Augsburger, 2013). These units can be used for comparison with other CSP technologies or other sources of energy. Subsequently, LCOE is defined and the results are presented for comparison of the three heliostat fields considered. The design considerations used for the evaluation of the thermo-economic performance of the three plants is presented in Appendix A.

8.1 Thermo-economic performance

The thermo-economic performance of power tower plants depends on the optimal size of its components and since the solar field and the TES system are the most cost intensive subsystems they must be sized carefully. For this reason, a parametric study is typically performed by increasing the SM and the number of hours of TES. A study done to identify the optimum hours of storage for a 100 MW_e power tower plant in Upington revealed that with a SM of 3 and 16 hours of storage, capacity factors as high as 92.19 % could be reached. However, upon consultation with ESKOM stakeholders, a capacity factor CF of 60 % is recommended by Madaly (2014) to determine the effect on the optimum storage capacity and investment costs. With this constraint in the capacity factor, a SM of 1.8 and 8 hours of TES were identified.

For the energy performance, hourly DNI values from the weather data are used. This weather data uses hourly values from a TMY3 file for Upington. The optical power is summed up during each hour for each heliostat in the field to get the annual energy

reflected by the solar field to the receiver (Kunert *et al.*, 2009). The annual energy reaching the receiver is approximated as:

$$E_{rec} = A_h \times DNI \times N_{hel} \times \eta_{sf} \tag{8.1}$$

The net annual electrical energy generated by the plant is calculated by using an approximate cycle thermal efficiency of 41 %, a receiver solar to thermal efficiency (described in § 5.10) and a CF of 60 % and is expressed as:

$$E_{e,a} = E_{rec} \times \eta_{rec} \times \eta_{des} \times CF \tag{8.2}$$

8.2 LCOE

LCOE is defined "as the total lifetime cost of an investment divided by the cumulated generated energy by this investment" (Pawel, 2014) and is expressed as (Pitz-Paal *et al.*, 2005):

$$LCOE = \frac{\left(CRF \times C_{i,tot}\right) + OPEX + k_{fuel}}{E_{e,a}} \tag{8.3}$$

where, CRF is the capital recovery factor and is an indication of the number of equal instalments that must be paid over a certain time with a certain interest rate and is expressed as:

$$CRF = \frac{k_d \times (1+k_d)^n}{(1+k_d)^n - 1} + k_i \tag{8.4}$$

where, n is the lifetime and depreciation rate in years (taken as 25 years), k_d is the annual debt interest rate (taken as 8 %), and k_i is the annual insurance rate (relative to total installed costs of the plant), in this case, is 0.5 %. Table 8.1 shows the summary of the thermo-economic performance and the LCOE values. The LCOE value is being used as a figure of merit.

Table 8.1: Summary of thermo-economic performance of the three plants

Item	Field with large size heliostat	Field with medium size heliostat	Field with small size heliostat
Capital Recovery Factor (%)	9.88	9.88	9.88
Heliostat field cost ($/m^2)	176.26	166.23	165.69
Total capital costs ($)	677 965 762	652 517 939	624 566 401
Annual O&M costs($)	8 107 845	8 266 131	8 546 940
Cost of fuel ($)	0	0	0
Annual electrical energy generated (GWh_e)	351.75	366.32	336.51
LCOE ($/$kWh_e$)	0.2115	0.1960	0.2017

The results indicate that the medium sized heliostat with an LCOE of 0.1960 $/$kWh_e$ is a better choice for the power tower plant considered in this study. This gives us an indication that heliostat cost per unit area should not be the only figure of merit for choosing an appropriate heliostat size for the plant. The total capital costs, the annual O&M costs, and the energy performance i.e. the annual electrical energy generated by the plant should be taken into consideration while comparing heliostats of different sizes.

8.3 Summary of results

The thermo-economic performance of the three power tower plants is estimated by combining both the energy and the economic performance. Primary and derived indicators are defined and estimated. The LCOE values are calculated using the primary and the derived indicators for the three power tower plants and are used as a figure of merit to compare the three heliostat sizes. The results show that a holistic LCOE model must be used to compare heliostats of different sizes. Additionally, the cost per unit area may be used as a guideline but not as the deciding factor for choosing the best suitable heliostat.

9. Conclusions and Outlook

With the aim of reducing heliostat costs in a power tower plant, a holistic LCOE model which includes the thermo-economic performance, along with the annual O&M costs is suggested to recommend the suitable heliostat size for a power tower plant with a net capacity of 100 MW_e. This chapter summarizes the findings of the study and makes recommendations for further work further research in the field of heliostat cost reduction

9.1 Summary of findings

This thesis focused on a power tower plant with a net capacity of 100 MW_e, TES of 8 hours and a SM of 1.8. For this configuration, a medium sized heliostat with an area of 43.33 m^2 is recommended for this particular heliostat field layout. The results are based on the scaling effects, the learning curve benefits, the price index, and the optical performance of individual heliostats. The LCOE model includes the direct and indirect capital costs of all the components involved in a power tower plant along with the energy performance of the heliostat field layout. It can be concluded that heliostat cost per unit area should not be the only figure of merit for choosing an appropriate heliostat size for the plant. The total capital costs, the annual O&M costs, and the energy performance i.e. the annual electrical energy generated by the plant should be taken into consideration while comparing heliostats of different sizes.

9.2 Future work

Heliostat cost reduction is a very broad subject that is very important for the market development of power tower plants. A tariff structure was not included in this study. Payment allocation factors for the time of day (TOD) and time of use (TOU) dispatch schedule also affect the heliostat position in the field layout. This should be included

in further studies by power tower developers to investigate the effect of the tariff structure which has been observed to change with every round in REIPPPP.

Furthermore, different heliostat sizes and shapes must be considered. Donker *et al.* (2016) investigated using a 2 m^2 heliostat in a 100 MW_e power tower plant and report that costs could be reduced by directly measuring the orientation of the mirror. Balz *et al.* (2016b) recommend using a roundish shape to reduce the blocking and shading effects and design compact field layouts. These two parameters can be included in further studies.

A suspension heliostat developed recently has reported using about 60 to 80 % less steel than conventional heliostats by stabilizing the structure with steel cables from the front and the rear (Bender, 2013). Such innovative designs must also be considered in the future studies.

Landman *et al.* (2016) suggest incorporating the incidence angle effects into the beam quality and the tracking error terms as this is negligible computational expense but corrects the deviation and is shown to be robust. These effects must be included in further studies.

Monreal *et al.* (2014) suggest using mass manufactured cheap drives produced for markets with a high volume. Within this context, CENER and IK4-TEKNIKER have developed the 'EASY (hEliostats for eAsy and Smart deploYment)' concept where a proper calibration system is also being implemented. Heliostat calibration needs to be included in future studies.

It is further recommended to include a sensitivity analysis to understand the effects of different solar multiples, hours of TES and heliostat design parameters like heliostat geometry in future studies.

Appendices

Appendix A: Thermo-economic performance

TECHNICAL PERFORMANCE			
Characteristics of the power tower plant	**Heliostat 1 (Large heliostat)**	**Heliostat 2 (Medium heliostat)**	**Heliostat 3 (Small heliostat)**
Location and Resource	This section looks at the location and the solar resource available at the location, in this case in Upington.		
Location (-)	Upington, Northern Cape Province, South Africa (ESKOM, 2016)		
Elevation (m)	814		
Time zone (-)	GMT + 2		
Annual sum of DNI (kWh/m^2/year)	2863 (obtained from TMY3 weather dataset from Upington)		
Long term annual average DNI (kWh/m^2/year)	2816 (Suri, 2011)		
Data source used for this study (-)	Typical Meteorological Year (TMY)		
Latitude (°N)	-28.43		

Longitude (°E)	21.05
Design point parameters and main systems	This section looks at the design point parameters for the heliostat field, tower and receiver, thermal energy storage system and the power cycle for the power tower plant.
Design turbine gross output (MW_e)	114.3
Estimated gross-to-net conversion factor (-)	0.875 (assumed)
Cooling system (-)	Dry cooling (Weinrebe *et al.*, 2014)
Estimated net output at design (nameplate) (MW_e)	*Estimated Net Output at Design* (MW_e) = *Design turbine Gross Output* (MW_e) × *Estimated Gross-to-net Conversion Factor* = 114.3×0.875 = 100.0125
Cycle thermal efficiency (%)	41 (Madaly, 2014)
Cycle thermal power, (MW_t)	*Cycle Thermal Power* (MW_t) = *Design Turbine Gross Output* (MW_e) ÷ *Cycle Thermal Efficiency* = 114.3÷0.41 = 278.780
Solar multiple (-)	1.8 (Madaly, 2014)
Receiver type (-)	External cylindrical receiver
Receiver thermal power (MW_t)	*Receiver Thermal Power* (MW_t) = *Solar Multiple* × *Cycle Thermal Power* (MW_t) = 278.780×1.8 = 501.805

Design point DNI (W/m^2)	950 (Pan, 2015) ; this value is also in agreement with the P90 analysis for DNI values over the year.		
HTF hot temperature (°C)	574 (SAM default value), This is the temperature of the hot HTF at the outlet of the receiver outlet.		
HTF cold temperature (°C)	290 (SAM default value), this is the temperature at which the HTF enters the receiver inlet.		
Full load hours of storage (h)	8 (Madaly, 2014), This is the number of hours the storage system can supply energy at the design point for the cycle.		
Solar field hours of storage (h)	*Solar Field Hours of Storage = Full Load Hours of Storage ÷ Solar Multiple* = 8÷1.8 = 4.44		
Solar field and SolarPILOT input values	This section describes the layout of the solar fields for the three heliostat sizes chosen and the inputs for the model and the optimization of the solar field in the SolarPILOT software.		
Heliostat size (m^2)	115.56	43.33	16.69
Shape (-)	Rectangular	Rectangular	Rectangular
Range of heliostat size (m^2)	60-150	20-60	1-20
Type of heliostat (-)	Azimuth-elevation		
	Conventional torque tube		

Conventional support structure (-)			
Hypothetical Company/ Developer with this type of heliostat (-)	Sener	SBP sonne GmbH	Brightsource
Plant already installed in/ designed for (-)	Gemasolar (Collado and Guallar, 2013)	Hypothetical	Hypothetical
Heliostat height (m)	9.00 (Weinrebe, 2014)	6.42 (Weinrebe, 2014)	3.21 (Weinrebe, 2014)
Heliostat width (m)	12.84 (Weinrebe, 2014)	6.75 (Weinrebe, 2014)	5.20 (Weinrebe, 2014)
Ratio of reflective area to profile for typical heliostat of this size (-)	0.964 calculated from (Lata *et al*., 2010)	0.97 (Weinrebe *et al.*, 2014)	0.92 (Huss *et al.*, 2011)
Single heliostat effective mirror reflective area (m^2)	110.74	42.03	15.36
Heliostat optical error one axis (mirror slope error)	2.60 (Augsburger, 2013)	0.88; measured as 1.18 (Balz *et al.*, 2016)	1.30 (Pfahl *et al.*, 2013)
Heliostat availability in plant (-)	0.99 (assumption)		
	4 (Weinrebe, 2014)		

Number of facets in X direction (-)		3 (Weinrebe, 2014)	2 (Weinrebe, 2014)
Number of facets in Y direction (-)	4 (Weinrebe, 2014)	2 (Weinrebe, 2014)	1 (Weinrebe, 2014)
Pedestal height (m)	5.675 (Augsburger, 2013)	3.500 (assumed)	2.250 (assumed)
Heliostat visualization (-)	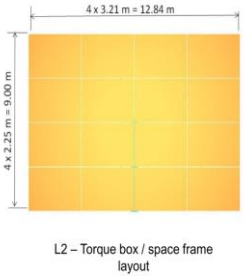 L2 – Torque box / space frame layout	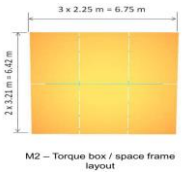 M2 – Torque box / space frame layout	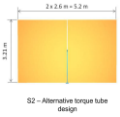 S2 – Alternative torque tube design
Heliostat focusing method (-)	Flat; this is the method used to determine the focal point for the heliostat (facet) surface(s). if there are several facets, it applies to individual facets		
Heliostat canting method (-)	Equinox; the facets are mounted so that the image they reflect on the receiver strikes the aim point when the sun is in equinox position (March 20th or September 20th). In this case, the date chosen is 20th September, 2016 which is a leap year.		
Mirror type /thickness (mm)	Float glass / 4; assumption (Vazquez *et al.*, 2006)		
Atmospheric attenuation polynomial coefficient 0 (-)	0.006739 (Wagner, 2008)		
Atmospheric attenuation polynomial coefficient 1, (1/km)	0.1046 (Wagner, 2008)		

Atmospheric attenuation polynomial coefficient 2, ($1/km^2$)	-0.017 (Wagner, 2008)
Atmospheric attenuation polynomial coefficient 3, ($1/km^3$)	0.002845 (Wagner, 2008)
Visibility (km)	23
Maximum distance to tower height ratio (-)	20; quasi- no limitation on this value (Reeken *et al.*, 2016a)
Minimum distance to tower height ratio (-)	0.75; (Reeken *et al.*, 2016a)
Receiver coating absorptance (-)	0.94; Absorptance fraction of the coating on the tubes of the receiver. Typical values are 0.91 to 0.95 in SAM 2016.3.14
Height of Tower (Initial guess) (m)	180; an initial value guessed for SolarPILOT to use as a reference value for optimization values
Receiver height (m)	22.7985; an initial value guessed for SolarPILOT to use as a reference value for optimization values
Receiver diameter (m)	26.5135; an initial value guessed for SolarPILOT to use as a reference value for optimization values
Receiver heat loss design factor (-)	1; this means that there is no correction in the heat loss values. The modes of convection and radiation are considered.
	3 030 000

Tower fixed costs ($)	(Reeken *et al.*, 2016a)		
Tower cost scaling exponent (-)	0.006931 (Reeken *et al.*, 2016a)		
Receiver reference costs ($/m^2)	102 100 000 (Reeken *et al.*, 2016a); these are the costs for receiver installation costs, including labour and equipment.		
Receiver reference area ($/m^2)	1571 (Reeken *et al.*, 2016a)		
Receiver cost scaling exponent (-)	0.7, this is the nonlinear relationship between the cost of the receiver and the area of the receiver.		
Site improvement costs not included in heliostat field costs ($/m^2)	16 (Kurup and Turchi, 2015)		
Heliostat field costs ($/m^2)	176.26 (calculated)	166.23 (calculated)	165.69 (calculated)
Power Block ($/kW$_e$)	1190 (Kurup and Turchi, 2015); this is for the power block components and control systems, and construction of buildings, including the labour and equipment.		
Balance of plant (BOP) ($/kW$_e$)	340 (Kurup and Turchi, 2015); this is cost for the BOP plant components, control systems, and construction of buildings, including the labour and equipment.		
HTF and storage medium considered (-)	Solar salt (60 % $NaNO_3$ and 40 % KNO_3) (Weinrebe *et al.*, 2014)		
Thermal energy storage costs ($/kWh$_t$)	26 (Reeken *et al.*, 2016a); these costs are for the installation of a thermal energy storage system, including the equipment and the required labour.		

Fixed solar field costs ($)	0 (SAM default value assumed); this value accounts for the costs not included in any of the categories mentioned above.
Contingency rate (%)	5, Contingency accounts for all the unexpected costs that arise in the calculations of the direct costs mentioned above.
Sales tax rate (%)	14.5 (sales tax in South Africa in 2016 is 14.5 %)
Sales tax fraction (%)	80; SAM default value which is expressed as a percentage of the total direct costs
Optimization settings using SolarPILOT	This section describes the optimization method and the settings used to generate the optimized heliostat field layout.
Optimization algorithm chosen (-)	RSGS (Wu and Hamada, 2000)
Initial optimization step size (-)	0.05 (SAM default value assumed)
Maximum optimization iterations (-)	200 (SAM default value assumed)
Optimization convergence tolerance (-)	0.001 (SAM default value assumed)
Over-flux objective penalty factor (-)	0.35 (SAM default value assumed)

SolarPILOT optimization values for the heliostat field	This section describes the values accepted after using SolarPILOT to generate the optimal heliostat field layout.		
Number of heliostats in the field (-)	8131	21 670	55 544
Tower optical height (m)	171.9	168.8	156.9
Receiver height (m)	23.0839	22.9347	17.4578
Receiver diameter (m)	17.9997	17.2356	16.2738
Total heliostat reflective area (m^2)	951 770	920 385	915 592
Simulation time (sec)	339.1	958	1518
Heliostat dimensional considerations for the heliostat field layout	The three fields are made using the radial staggered pattern (Wagner, 2008)		
Radial increment (m)	$\Delta R = (1.1442 \times \cot\theta_L - 1.0935 + 3.0684\theta_L^{\ 2}) \times H_{helio}$ (Wagner, 2008)		
Azimuthal increment (m)	$\Delta AZ = (1.791 + 0.6396 \times \theta_L) \times W_{helio} + \frac{0.02873}{\theta_L - 0.04902}$ (Wagner, 2008)		
Heliostat footprint diameter (m)	15.7 (Vazquez *et al.*, 2006)		6.11; (Vazquez *et al.*, 2006)

		9.31; taken as 9 for safety (SBP, 2015)	
Additional separation distance (m)	0 (Collado and Guallar, 2013)	0 (Collado and Guallar, 2012)	0 (Collado and Guallar, 2012)
Diagonal + safety distance (m)	15.7 + 0 = 15.7	9 + 0 = 9	6.11 + 0 = 6.11
Horizontal clearance distance (m)	15.7-12.305 = 3.4	9.31 – 6.75 = 2.56	6.11 - 5.2 = 0.91
Minimal radial increment (m)	13.6	8.06	5.29
Vertical clearance distance (m)	13.6 – 9.752 = 3.85	8.06– 6.42 = 1.64	5.29 -3.21 = 2.08
Method of Cleaning (-)	HECTOR (Heliostat Cleaning Team-Oriented Robot) (Hardt *et al.*, 2011)	HECTOR (Hardt *et al.*, 2011)	Semi-automated system for heliostat cleaning (Schell, 2011)
Optical efficiency calculations	This section considers the optical losses i.e. cosine, atmospheric attenuation, interception/spillage, blocking and shading losses		
Cosine losses calculation method	$\eta_c = \vec{n} \cdot \vec{S}$ (Besarati and Goswami, 2014)		
Cosine efficiency (%)	80.00	81.50	79.80

Blocking factor (-)	$f_b = 1 - \left[\frac{\Delta R}{L}\left(\frac{\cos(\varepsilon_T) + \tan(\beta)\sin(\varepsilon_T)}{\cos(\omega)}\right)\right] \times \left[\frac{2f - (\sqrt{1+f^2} + ds)}{f}\right]$ (Collado, 2009)		
Blocking efficiency calculation method	$\eta_b = 1 - f_b$		
Blocking efficiency (%)	96.10	97.20	96.80
Shading efficiency calculation method	Shading efficiency is not included (Falcone, 1986)		
Atmospheric attenuation factor calculation method	$\eta_a = 0.99321 - 0.0001176d + 1.97 \times 10^{-8} d^2; d \leq 1000$ $\eta_a = \exp(0.0001106d); d > 1000$ (Collado and Turégano, 1989; Leary and Hankins, 1979; Schmitz *et al.*, 2006)		
Mirror reflectance and soiling (-)	0.9025		
Interception losses formula method	$\eta_i = \frac{A_{eff}}{A_{total}}$ (Lutchman, 2014)		
Interception efficiency (%)	96.10	97.20	96.80
Tower shadow efficiency (%)	The effect of the tower shadow on the solar field efficiency is not included.		

Receiver solar-to-thermal efficiency	$\eta_{rec} = \frac{Q_{in} - Q_{loss}}{Q_{in}} = \frac{\alpha Q_{in} - \varepsilon \sigma A_{rec} (T_{wall})^4 - h A_{rec} (T_{wall} - T_{amb})}{Q_{in}}$ (Christian *et al.*, 2015)		
Absorptivity (-)	0.94		
Emissivity (-)	0.85		
Stefan–Boltzmann constant ($W/m^2/K^4$)	5.67×10^{-8}		
Incident receiver thermal power (MW_t)	501 805 000		
Receiver area (m^2)	1305.342	1241.851	892.706
Average wall temperature (K)	873		
convective heat transfer coefficient ($W/m^2/K$)	10		
Ambient temperature (K)	293		
Receiver solar-to-thermal efficiency - model (%)	87.56	87.96	90.13
Solar field area calculations			
Solar Multiple (-)	1.8		

Total solar to electric efficiency (%)	22.927	23.697	23.758
Total power block electrical capacity (W)		~114 300 000	
Total solar field reflective area - Model calculation (m^2)	944 600	913 903	911 551
Total solar field reflective area - SolarPILOT (m^2)	946 435	910 897	916 621
Difference in model and SolarPILOT (m^2)	-1834.18	3006.19	-5069.75
Difference in model and SolarPILOT (%)	-0.19	0.32	-0.55
Non- solar field land area (acres)		45.00	
Solar Field land area (acres)	1406	1167	1864
Solar field land area multiplier (-)		1.3	
Total land area (acres)	1873	1562	2468

FINANCIAL PERFORMANCE

Direct Capital Costs

Site Improvements costs	$C_{site,tot} = C_{site} \times A_{sf}$		
Site improvement cost per square meter ($/m^2)	16		
Total site improvement costs ($)	15 113 612	14 622 451	14 584 819
Heliostat subcomponent calculation method	$C_{h,tot} = C_h \times N_{hel}$ where, $C_h = C_0 \times \left(\frac{A_h}{A^0{}_h}\right)^s \times (pr)^{\log_2\left(\frac{V_h}{V^0{}_h}\right)} \times pi$		
Foundation ($)	2677.72	609.10	130.97
Steel support structure and pedestal ($)	9919.28	2354.40	528.57
Drives ($)	5426.40	2780.29	1397.05
Controls ($)	106.82	80.60	60.43
Reflector panels ($)	1529.65	533.97	179.42
Assembly ($)	1091.49	701.82	444.47
Optical Improvements costs calculation method	$C_{h,opt} = C_{h,optic} \times N_{hel}$		

where,

$$C_{h,optic} = 0.01 \times 10^{-3} \times \left(\frac{1}{\sigma_{rss}^{\ 2}} - \frac{1}{\sigma^{0}{}_{rss}^{\ 2}} \right) \times A_h$$

(Augsburger, 2013)

Optical improvement ($)	-119.30	-	-9.69
Total cost per unit ($/unit)	20 632.06	7060.18	2731.20
Total costs of the heliostat field ($)	167 759 285	152 994 208	151 702 046
Heliostat field cost per unit area ($/m^2)	177.60	167.41	166.42
Tower costs ($)	$C_{t,tot} = C_{t,fixed} \times e^{k_t \times H_t}$ (Turchi and Heath, 2013)		
Fixed Tower costs ($)		3 030 000	
Tower cost scaling exponent (-)	0.0113	0.0113	0.0113
Heliostat height (-)	9.752	6.42	3.21
Tower optical height (-)	171.9	168.8	156.9
Tower height for calculating costs (m) – (Tower optical height +heliostat height/2)	176.78	172.01	158.51

Total tower costs ($)	20 713 925	19 278 058	16 762 915
Receiver costs ($)	$C_{r,tot} = C_{r,ref} \times \left(\frac{A_{rec}}{A^{0}_{rec}} \right)^{k_{rec}}$ (Turchi and Heath, 2013)		
Receiver reference costs ($)	102 100 000		
Receiver reference area (m^2)	1571	1571	1571
Receiver height (m)	23.08	22.93	17.45
Receiver diameter (m)	17.99	17.23	16.27
Area of receiver calculated (m^2)	1305.34	1241.85	892.70
Receiver cost scaling exponent (-)	0.7	0.7	0.7
Total receiver costs ($)	89 682 857	86 606 592	68 738 223
Thermal energy storage costs ($)	$C_{TES,tot} = C_{TES} \times \frac{N_{h,TES} \times W_{des}}{\eta_{des}}$		
Solar Multiple (-)	1.8		
Cycle thermal power (MW_t)	278.78		
	501.805		

Incident receiver thermal power (MW_t)	
Full load storage (h)	8
Solar field hours of storage (h)	4.44
TES Storage capacity (MWh_t)	2230.24
TES Storage capacity (kWh_t)	2 230 243
Thermal energy storage costs per unit ($/$kWh_t$)	26.00
Total thermal energy storage costs ($)	57 986 341
Power cycle costs Calculation method (-)	$C_{PB,tot} = C_{PB} \times W_{des}$
Cycle gross capacity (MW_e)	114.3
Cycle gross capacity (kW_e)	114 300
Balance of plant costs ($/kWe) per kWe	340.00

Balance of plant costs for total plant ($)	38 862 000		
Power cycle costs ($/kWe)	1190.00		
Power cycle costs for total plant ($)	136 017 000		
Subtotal direct costs calculation method (-)	$C_{d,s} = \begin{pmatrix} C_{s,tot} + C_{h,tot} + C_{h,opt} + C_{t,tot} + C_{r,tot} + C_{TES,tot} + \\ C_{SGS,tot} + C_{PB,tot} \end{pmatrix}$		
Subtotal direct costs ($)	526 135 022	506 366 652	484 653 347
Contingency cots calculation method	$C_{c,tot} = C_{d,subtot} \times CP$		
Contingency costs ($)	26 306 751	25 318 332	24 232 667
Total direct costs calculation method	$C_{d,tot} = C_{d,s} + C_{c,tot}$		
Total direct costs ($)	552 441 774	531 684 984	508 886 014
Indirect Capital Costs			
EPC costs calculation method	$C_{EPC,tot} = C_{d,tot} \times EPCP$		
EPC as a percentage of direct costs (%)	11		

Total land costs calculation method	$C_{l,tot} = C_l \times A_{land}$
Cost of land per hectare in Upington (ZAR)	2730.00
Cost per acre (ZAR)	1104.79
ZAR to USD conversion (1 ZAR to 1 USD)	0.0640 (as on 15th May, 2016)
Cost of land per acre in Upington (USD)	70.71
Total land area (acres)	1872.9
Minimum land area available (hectares)	3847.0
Minimum land area available (acres)	9506.1
Total cost of land in ZAR (ZAR)	10 502 310
Cost of land in Upington, South Africa (USD)	672 147.84
Sales tax calculation method	$C_{ST,tot} = STR \times STB \times C_{d,tot}$

Sales tax basis of total direct costs (%)		80	
Sales tax rate (%)		14.50	
Total sales tax ($)	64 083 245	61 675 458	59 030 777
Indirect capital costs ($)	61 703 810	59 410 679	56 891 936
Total installed costs calculation method ($)		$C_{inst,tot} = C_{d,tot} + C_{i,tot}$	
Total installed costs	587 838 833	565 777 331	541 545 283
TECHNO-ECONOMIC PERFORMANCE			
Net annual energy to receiver from solar field, (kWh_t)	1 634 155 533	1 701 836 977	1 563 346 007
'Solar to thermal' efficiency of receiver (%)		88	
Net annual energy to power block from receiver (kWh_t)	1 441 762 971	1 507 503 914	1 415 277 055
Capacity factor (CF) (%)		60	
Net annual energy including CF (kWh_e)	354 673 690	370 845 962	348 158 155

Net annual energy including CF (MWh_e)	354 673.69	370 845.96	348 158.16
Net annual energy (GWh_e)	354.6737	370.8460	348.1582
O&M costs			
Fixed costs by capacity ($/kW-yr.)	67	68	72
Variable costs by generation ($/$MWh_e$)		4	
Annual O&M Costs ($)	8 119 532	8 284 233	8 593 532
LCOE calculations			
Yearly nominal interest rate (%)		8	
Number of years in the plant lifetime (-)		25	
Annuity factor (-)		0.0936	
Annual insurance rate (%)		0.5	
Capital recovery factor (CRF) (-)		0.0986	
Annual fuel costs ($)		0	

LCOE calculation method	$LCOE = \frac{(CRF \times C_{installed,tot}) + OPEX + k_{fuel}}{E_{e,a}}$ (Pitz-Paal *et al.*, 2005)		
LCOE of the plant ($/kWh$_e$)	**0.2115**	**0.1960**	**0.2017**

Appendix B: Computer code

The following code is used to analyse the weather data (DNI and wind speed) at the site and to plot the solar field layout once the field is optimized using SolarPILOT.

```
1.     import math  # importing the math module into python
2.     import numpy as np  # importing the numpy module as np
3.     from numpy import array  # importing arrays
4.     import matplotlib.pyplot as plt  # importing the plotting fucntion a
s plt from the matplotlib module
5.
6.     City = 'Upington'
7.     print(City, " is the location of the power tower")
8.
9.     State = 'Northern Cape'
10.    print(State, " is the province where the power tower is loacted")
11.
12.    Country = 'South Africa'
13.    print(Country, " is the country where the power tower is loacted")
14.
15.    Time_Zone = 'GMT+2'
16.    print(Time_Zone, " is the time zone")
17.
18.    Elevation = 814
19.    print(Elevation, " is the elevation of the location in [msl]")
20.
21.    # Charts used in ocean navigation often use the OPPOSITE notation--
Î» for LONGITUDE and Ï† for LATITUDE and is used here.
22.    #  Latitude of the location,
23.    PHID = -28.433
24.    print(PHID, "North, latitude of the location in degrees (PHID)")
25.    PHIR = math.radians(PHID)
26.    print(PHIR, "is the value of PHI in Radians (PHIR)")
27.
```

```
    #  Longitude of the location, Lambda
    LL = 21.05
    print(PHID, "East, longitude of the location in degrees")

    #  This section considers the weather data - solar resource at locat
ion and wind speeds

    import csv
    import pylab #Imports pylab

    # Reading data from csv file
    with open('Upington_DNI.csv') as csvfile:
        readCSV = csv.reader(csvfile, delimiter=',')
        Hour_of_year = []
        Beam_irradiance = []
        for row in readCSV:
            hour = row[0]
            DNI = row[1]
            Hour_of_year.append(hour)
            Beam_irradiance.append(DNI)
    Hours_since00hrsJan1 = [float(Hour_of_year[c]) for c in range(1,len(
Hour_of_year))]
    Beam_irradiance_DNI=[float(Beam_irradiance[c]) for c in range(1,len(
Beam_irradiance))]

    # Plotting DNI vs time
    plt.figure(1)
    plt.plot(Hours_since00hrsJan1,Beam_irradiance_DNI, color="orange")
    plt.title("Hourly beam irradiance for Upington")
    plt.xlabel("Hour of year (-
)"); plt.ylabel("Beam irradiance - DNI [W/mÂ²]")
    pylab.xlim([0,8760])
    plt.savefig('Figure 1 - Hourly beam irradiance for Upington.png')
    plt.show()

    from matplotlib.colors import LogNorm
    import matplotlib.cm as cm
    # Plotting the histogram for the design DNI for the plant
    plt.figure(2)
    plt.hist((Beam_irradiance_DNI), color="orange", bins=15)
    plt.title("Histogram for Beam irradiance - DNI")
    plt.xlabel("Beam irradiance - DNI [W/mÂ²]"); plt.ylabel("Probability
 of occurrence (-)")
    pylab.xlim([0,1090])
    plt.savefig('Figure 2 - Histogram for beam irradiance - Upington.png
')
    plt.show()

    import numpy as np
    import matplotlib.pyplot as plt
```

```
    import matplotlib.cm as cm
    import matplotlib.colors as colors

    # Wind speeds for Upington
    # Reading wind speed data from csv file for Upington

    with open('Upington_Windspeed.csv') as csvfile:
        readCSV = csv.reader(csvfile, delimiter=',')
        Hourssince00hrsJan1 = []
        Windspeeds = []
        for row in readCSV:
            hour = row[0]
            windspeed = row[1]
            Hourssince00hrsJan1.append(hour)
            Windspeeds.append(windspeed)
    Hours_since00hrsJan1 = [float(Hourssince00hrsJan1[c]) for c in range
(1,len(Hourssince00hrsJan1))]
    Wind_speeds=[float(Windspeeds[c]) for c in range(1,len(Windspeeds))]

    # Plotting Windspeed vs time
    plt.figure(3)
    plt.plot(Hours_since00hrsJan1,Wind_speeds,color="blue")
    plt.title("Frequency of gust wind speeds at Upington")
    plt.xlabel("Hours since 00Hrs Jan1 (-
)"); plt.ylabel("Wind Speed interval [m/s]")
    plt.savefig('Figure 4 - Frequency of hourly wind speeds.png')
    pylab.xlim([0,8765])
    plt.show()

    # Plotting the histogram for GoToStow wind speeds
    plt.figure(4)
    plt.hist(Wind_speeds, color="blue")
    plt.title("Histogram - Wind speed in Upington")
    plt.savefig('Figure 5 - Histogram of wind speed.png')
    plt.xlabel("Wind speeds [m/s]"); plt.ylabel("Frequency of occurrence
 (-)")
    plt.show()

    import numpy as np
    # Plotting the heliostat field by using the coordinates of heliostat
s obtained by SolarPILOT
    import matplotlib.pyplot as plt
    # 1. LARGE HELIOSTAT
    import csv

    # Large area heliostat - 115.56 mÂ²
    # Reading data from csv file
    with open('SolarPILOT_Upington_large_helio.csv') as csvfile:
        readCSV = csv.reader(csvfile, delimiter=',')
        X = []
```

```
        Y = []
        Z = []

        for row in readCSV:
            X_coordinates = row[0]
            Y_coordinates = row[1]
            Z_coordinates = row[2]
            X.append(X_coordinates)
            Y.append(Y_coordinates)
            Z.append(Z_coordinates)
    Xcoordinate = [float(X[c]) for c in range(1,len(X))]
    Ycoordinate=[float(Y[c]) for c in range(1,len(Y))]
    Zcoordinate=[float(Z[c]) for c in range(1,len(Z))]

    # Plotting the solar field for the large heliostat - 115.56 mÂ²
    plt.figure(5)
    plt.scatter(Xcoordinate,Ycoordinate, color = 'black', s=1)
    plt.title("Solar field layout with large heliostat\nheliostat size:
115.56 mÂ²; Number of heliostats: 8131")
    plt.savefig('Figure 6 - Solar field layout with large heliostat.png'
)
    plt.xlabel("Position, east-west [m]"); plt.ylabel("Position, north-
south [m]")
    plt.show()

    # Medium area heliostat - 43.33 mÂ²
    # Reading data from csv file
    with open('SolarPILOT_Upington_medium_helio.csv') as csvfile:
        readCSV = csv.reader(csvfile, delimiter=',')
        X = []
        Y = []
        Z = []
        for row in readCSV:
            X_coordinates = row[0]
            Y_coordinates = row[1]
            Z_coordinates = row[2]
            X.append(X_coordinates)
            Y.append(Y_coordinates)
            Z.append(Z_coordinates)
    Xcoordinatem = [float(X[c]) for c in range(1,len(X))]
    Ycoordinatem=[float(Y[c]) for c in range(1,len(Y))]
    Zcoordinatem=[float(Z[c]) for c in range(1,len(Z))]

    # Plotting the solar field for the medium heliostat - 43.33 mÂ²
    plt.figure(8)
    plt.scatter(Xcoordinatem,Ycoordinatem, color = 'black', s= 43.33/115
.56)
    plt.title("Solar field layout with medium heliostat\nheliostat size:
 43.3 mÂ²; Number of heliostats: 21 670")
```

```
plt.savefig('Figure 7 - Solar field layout with medium heliostat.png')
plt.xlabel("Position, east-west [m]");plt.ylabel("Position, north-south [m]")
plt.show()

# Small area heliostat - 16.69 mÂ²
# Reading data from csv file
with open('SolarPILOT_Upington_small_helio.csv') as csvfile:
    readCSV = csv.reader(csvfile, delimiter=',')
    X = []
    Y = []
    Z = []
    for row in readCSV:
        X_coordinates = row[0]
        Y_coordinates = row[1]
        Z_coordinates = row[2]
        X.append(X_coordinates)
        Y.append(Y_coordinates)
        Z.append(Z_coordinates)
XcoordinateS = [float(X[c]) for c in range(1,len(X))]
YcoordinateS=[float(Y[c]) for c in range(1,len(Y))]
ZcoordinateS=[float(Z[c]) for c in range(1,len(Z))]

# Plotting the solar field for the medium heliostat - 16.69 mÂ²
plt.figure(9)
plt.scatter(XcoordinateS,YcoordinateS, color='black', s=16.69/115.56)
plt.title("Solar field layout with small heliostat\nheliostat size: 16.69 mÂ²; Number of heliostats: 55 544")
plt.xlabel("Position, east-west [m]"); plt.ylabel("Position, north-south [m]")
plt.savefig('Figure 8 - Solar field layout with small heliostat.png')
plt.show()
```

The following code is used to calculate the sun vector.

```
import math  # importing the math module into python
import numpy as np  # importing the numpy module as np
from numpy import array  # importing arrays from the numpy module
import matplotlib.pyplot as plt  # importing the plotting function as plt from the matplotlib module

# "Charts used in ocean navigation often use the OPPOSITE notation--Î» for LONGITUDE and Ït for LATITUDE and is used here."
# Source: http://www-istp.gsfc.nasa.gov/stargaze/Slatlong.htm
#  Latitude of the location,
PHID = -28.433
```

```
10.    print(PHID, "North, latitude of the location in degrees (PHID)")
11.    PHIR = math.radians(PHID)
12.    print(PHIR, "is the value of PHI in Radians (PHIR)")
13.
14.    #  Longitude of the location, Lambda
15.    LL = 21.05
16.    print(PHID, "East, longitude of the location in degrees")
17.
18.    # This program is for the sun Vector on 22nd September as an
       example.
19.    # the representative design point is at Solar Noon on Spring Equinox
       , hence the date is 22 September 2016
20.    # Since 2016 is a leap year the day  number will be calculated as D+
       243  and +1 for the leap year,# Hence N = 22+243+1 = 266
21.    # N is the day of the year
22.    N = 266
23.    print(N, " is the day of the year")
24.
25.    Xd = 360 * (N-1)/365
26.    print(Xd, "is the value of X in Degrees (Xd)")
27.
28.    Xr = math.radians(Xd)
29.    print(Xr, "is the value of X in Radians (Xr)")
30.
31.    # Longitude correction
32.    LCH = (LL - LS)/15
33.    print(LCH, "is the Longitude correction in hours, (LCH)")
34.    LCM = LCH*60
35.    print(LCM, "is the Longitude correction in minutes, (LCM)")
36.
37.    EOT1 = ((0.258 * (math.cos(Xd)))-(7.416 * math.sin(Xd))-
       (3.468*math.cos(2*Xd))-(9.228*math.cos(2*Xd)))
38.    print(EOT1)
39.
40.    EOT = 229.2 * (0.000075 + 0.001868 * math.cos((Xr)) - 0.032077 * mat
       h.sin((Xr)) - 0.014615 * math.cos((2*Xr)) - 0.04089 * math.sin((2*Xr
       )))
41.    print(EOT, "is equation of time in minutes (EOT)")
42.
43.    # Standard Time, Time on a clock or wrist watch
44.    STDT = 11
45.    # Solar Time, ST
46.    ST = STDT + (4*(LL-LS)+ EOT)/60
47.    print(ST, " solar time in hours (ST)")
48.    # For example: If this value comes out to be 11.290071540838104
49.    # 0.290071540838104 is a fraction of 60 minutes , i.e. 3600 seconds
       i.e. 1044 seconds.
50.    # 1044 seconds translates to 17 minutes and 23 seconds
51.    # Hence the local time will be 11:17:23
52.
```

```
53.    # Hour angle, Omega
54.    Wd = (ST/24 - 0.5) * 360
55.    print(Wd, " hour angle in degrees (Wd)")
56.
57.    Wr = math.radians(Wd)
58.    print(Wr, " hour angle in radians (Wr)")
59.    # The declination angle must now be calculated
60.    # Declination angle, Delta in radians, Dr
61.    Dr = 0.006918 - 0.399912 * math.cos((Xr)) + 0.070257 * math.sin((Xr)
       ) - 0.006758 * math.cos((2*Xr)) + 0.000907 * math.sin((2*Xr)) - 0.00
       2679 * math.cos((3*Xr)) + 0.00148 * math.sin((3*Xr))
62.    print(Dr, " is declination angle in radians (Dr)")
63.
64.    DD = math.degrees(Dr)
65.    print(DD, " is declination angle in degrees (DD)")
66.
67.    # Another way to calculate the declination angle is by using the for
       mula: Delta = asin (0.39795 * cos [(0.98563(N-173)]
68.    DD1 = math.degrees(math.asin(0.39795*math.cos(math.radians(0.98563*(
       N-173)))))
69.    print(DD1)
70.    # This value is 13.457 which is very close to the value DD of 13.989
       9 , so using DD
71.
72.    DD1R = math.radians(DD1)
73.    print(DD1R)
74.
75.    # Zenith Angle, theta Z, in degrees
76.    ZD = math.degrees(math.acos(((math.sin(math.radians(PHID))* math.sin
       (Dr))+(math.cos(math.radians(PHID))*math.cos(Dr)*math.cos(math.radia
       ns(Wd))))))
77.    print(ZD, " is zenith angle in degrees (ZD)")
78.
79.    ZR = math.radians(ZD)
80.    print(ZR, " is the zenith angle in radians (ZR)")
81.
82.    # Zenith Angle, theta Z, in degrees
83.    ZD1 = math.pi/2 - math.asin(math.cos(PHIR) * math.cos((DD)) * math.c
       os(math.radians(Wr)) + math.sin((PHIR)) * math.sin((DD)))
84.    print(ZD1, " is zenith angle in radians (ZD1)")
85.
86.    ZR1 = math.degrees(ZD1)
87.    print(ZR1, " hour angle in degrees (ZR1)")
88.
89.    # Solar Altitude Angle, Alpha z, in degrees
90.    SALD = 90 - ZD
91.    print(SALD, " is the solar altitude angle in degrees (SALD)")
92.
93.    # Solar Altitude Angle, Alpha z, in radians
94.    SALR = math.radians(SALD)
```

```
    print(SALR, " is the solar altitude angle in radians (SALR)")

    # Solar Azimuth Angle, Ys
    def sign(Wd):
        if Wd > 0:
            return 1.
        elif Wd < 0:
            return -1.
        elif Wd == 0:
            return 0.
        else:
            return Wd
    SIGNW = sign(Wd)
    print(Wd)
    print(SIGNW, " since Wd is negative")

    # Solar Azimuth Angle, in degrees
    SAZD = SIGNW * math.degrees((math.acos(((math.cos(ZR)*math.sin(PHIR)
    -math.sin(Dr))/(math.sin(ZR)*math.cos(PHIR))))))
    print(SAZD, "is the solar azimuth angle in degrees (SAZD)")

    # Solar Azimuth Angle, in radians
    SAZR = math.radians(SAZD)
    print(SAZR, "is the solar azimuth angle in radians (SAZR)")

    #SUN VECTOR

    # East component of Sun Vector
    SE = math.cos(SALR)*(-math.sin(SAZR))
    print(SE, "is the east component of the sun vector (SE)")

    # North component of Sun vector
    SN = math.cos(SALR)*(-math.cos(SAZR))
    print(SN, "is the north component of the sun vector (SN)")

    # Zenith component of Sun Vector
    SZ = math.sin(SALR)
    print(SZ, "is the zenith component of the sun vector (SZ)")

    S = np.array((SE,SN,SZ))
    print(S, "is the sun vector (S)")
```

The following code is used to calculate the optical losses. As an example, two heliostats with the co-ordinates (15, 35, 5.35) and (15, 33, 5.35) are used along with a tower height of 170 m.

```
    XT = 0
    YT = 0
    ZT = 170
```

```
4.
5.      A = np.array(([XT],
6.                    [YT],
7.                    [ZT]))
8.      print(A," are the co-ordinates of the target i.e. the receiver")
9.
10.     X1 = 15
11.     Y1 = 35
12.     Z1 =5.35
13.
14.     B = np.array(([X1],
15.                   [Y1],
16.                   [Z1]))
17.     print(B," are the co-ordinates of the first heliostat")
18.
19.     X2 = 15
20.     Y2 = 33
21.     Z2 = 5.35
22.
23.     C = np.array(([X2],
24.                   [Y2],
25.                   [Z2]))
26.     print(C," are the co-ordinates of the second heliostat")
27.
28.     T1 = A - B
29.     print(T1," is the target vector for heliostat 1, T1")
30.
31.     modulusTVH1 = np.sqrt((T1**2).sum())
32.     print(modulusTVH1, "is the magnitude of this vector [t1]")
33.
34.     #Unit vector for heliostat 1
35.
36.     t1 = T1/modulusTVH1
37.     t1 = t1*np.array(([-1],[-1],[1]))
38.     print(t1, "is the unit vector for heliostat 1,t1")
39.
40.     # For heliostat 2
41.     T2 = A - C
42.     print(T2," is the target vector for heliostat 2,T2")
43.
44.     modulusTVH2 = np.sqrt((T2**2).sum())
45.     print(modulusTVH2, "is the magnitude of this vector")
46.
47.     #Unit vector for heliostat 2
48.
49.     t2 = T2/modulusTVH2
50.     t2 = t2*np.array(([-1],[-1],[1]))
51.     print(t2, "is the unit vector for heliostat 2,t2")
52.
53.     # Heliostat Normal
```

```
    # The heliostat normal for heliostat 1

    N1 = S+t1
    print(N1,"The heliostat normal for heliostat 1, N1")

    modulusN1 = np.sqrt((N1**2).sum())
    print(modulusN1, "is the magnitude of this vector")
    n1 = N1/modulusN1
    print(n1, "the unit vector for the normal vector is (n1)")

    # The heliostat normal for heliostat 1
    N2 = S+t2
    print(N2,"The heliostat normal for heliostat 2, N2")

    modulusN2 = np.sqrt((N2**2).sum())
    print(modulusN2, "is the magnitude of this vector")

    n2 = N2/modulusN2
    print(n2, "the unit vector for the normal vector is (n2)")

    # 1) cosine efficiency

    cosineeffn1 = (S*n1).sum()
    print(cosineeffn1, "is the cosine efficiency of heliostat 1")

    cosineeffn2 = (S*n2).sum()
    print (cosineeffn2, "is the cosine efficiency of heliostat 2" )

    # 2) Attenuation efficiency

    print(modulusTVH1)
    if modulusTVH1 < 1000:
        atteffn1 = (0.99321) - (0.0001176*modulusTVH1)+((1.97*(10**-
    8)*(modulusTVH1**2)))
        print(atteffn1)
    else:
        atteffn1 = np.exp(-0.0001106*modulusTVH1)
    print(atteffn1,"is the attenuation efficiency")

    # 3) Interception efficiency

    #diagonal of heliostat

    LW = 12.3  # Heliostat width
    LH = 9.75  # Heliostat height
    DH = math.sqrt(LW**2+LH**2)
    print(DH, "is the diagonal of the heliostat")

    #omega, angle of incidence, for this we first need St1
    St1 = S*t1
```

```
print(St1, "is the angle needed for calculating the incidence angle
")
#ST1 in python scalar
ST1 = np.sum(St1)
print(ST1)
Omegarad = (math.acos(ST1))/2
print(Omegarad, "is the angle of incidence, omegarad")

Omega = math.degrees(Omegarad)
print(Omega, "is the angle of incidence, omega")

# focal distance is set as the distance between the heliostat and th
e receiver , calculated as TVH1
f = modulusTVH1

# Target plane in tangential and sagittal plane
# Tangential plane calculation
Ht = math.fabs(DH*((modulusTVH1/f)-math.cos(Omegarad)))
print(Ht, "is the target image plane in the tangential direction")

# Sagittal plane calculation: A sagittal plane is an anatomical plan
e which divides the body into right and left halves.
Ws = math.fabs(DH*(((modulusTVH1/f)*(math.cos(Omegarad))-1)))
print(Ws, "is the target image plane in the sagittal direction")

# The total deviation
#The total deviation stot in HFLCAL is the result of the convolution
 of the Gaussian error functions considered :
# namely sunshape error, with standard deviation (ssun), beam qualit
y (sbq) associated with mirror slope errors (smse),
# the astigmatic effect (sast), and the tracking error (st).
ssun = 0.00251
print(ssun, "is the sunshape error in radians")

# beam quality error: = 2* mirror slope errors (smse)
# First calculate the mirror slope errors by using the slope errors
in the horizontal axis (sh) and vertical axis (sv)
# horizontal axis (sh) and vertical axis (sv) values in radians,
sh = 0.00102 # Collado and Guallar, 2013
sv = 0.00085 # Collado and Guallar, 2013
smse = (math.sqrt((sh**2 + sv**2)/2))
print(smse, "is the mirror slope error in radians")

# Finally beam quality error (sbq) can be calculated as = 2* mirror
slope errors (smse)
sbq = 2*smse
print(sbq, "is the beam quality error in radians")

# standard deviation for the astigmatic effect
sast = (math.sqrt((Ht**2 + Ws**2)*(0.5)))/(4*modulusTVH1)
```

```
print(sast, "is the astigmatic error in radians")

# tracking error (st)after 240 tracking tests of Sener heliostats under low wind speed conditions,
# an average standard deviation of the Gaussian tracking error of st = 0.63 mrad has been reported Collado and Guallar, 2013
strack = 0.00063 # Collado and Guallar, 2013
print(strack, "is the tracking quality error in radians")

# Total error:  The total deviation stot is calculated as follows
stot = math.sqrt((ssun**2 + sbq**2 + sast**2 + strack**2)*(modulusTVH1**2))
print(stot, "is the total error / total deviation in radians")

# View Height (ViewHt) = RecHt * (R/D) of the receiver must now be determined
RecHt = 20.41  # (SAM default value after optimization for a 100 MW power tower, change after using SolarPILOT)
RecDia = 17.61  # (SAM default value after optimization for a 100 MW power tower, change after using SolarPILOT)
HelRad = math.sqrt((XT-X1)**2 + (YT-Y1)**2) # Heliostat radius
print(HelRad, "is the heliostat radius")
ViewHt = RecHt * (HelRad/modulusTVH1)
print(ViewHt, "is the view height of the receiver")  # View height of the receiver

PosYlimit = ViewHt/2  # Positive integration limit for receiver height
print(PosYlimit, "is the positive limit of the receiver height")

NegYlimit = -1* PosYlimit  # Negative integration limit for receiver height
print(NegYlimit, "is the negative limit of the receiver height")

PosXlimit = RecDia/2  # Positive integration limit for receiver diameter
print(PosXlimit, "is the positive limit of the receiver diameter")

NegXlimit = -1* PosXlimit  # Negative integration limit for receiver height
print(NegXlimit, "is the negative limit of the receiver diameter")

# The interception efficiency has now been calculated using the integrating limits as the receiver diamter and View height
# This has been done on Mathematica.
# In this case the interception efficiency is given as 100% i.e. 1
Inteff = 1
print(Inteff, "is the interception efficiency")

# 4) Blocking efficiency
```

```
184.  # Some dimensional constraints are needed to calculate the blocking
      efficiency.
185.  Towerht = 203.3  # value taken now from SAM, later used
      from SolarPILOT
186.  LW = 12.3  # Heliostat width
187.  LH = 9.75  # Heliostat height
188.  DS = 0  # safety distance
189.  print(DS, "is the safety distance")
190.
191.  alpha = 90 - Omega  # This is the elevation angle of the heliostat
192.  print(alpha, "is the elevation angle of the heliostat, alpha")
193.
194.  beta = 0  # Field slope
195.  print(beta, "is the field slope, beta")
196.
197.  elev = 90 - math.degrees(math.acos(HelRad/modulusTVH1))  # elevation
       angle of the heliostat
198.  print(elev," is the elevation angle of the heliostat, elev")
199.  whr = LW/LH  # Heliostat width to height ratio
200.  print(whr," is the heliostat width to height ratio, whr")
201.  # Interference free diamteer
202.  DM = DH+DS
203.  print(DM," is the Interference free diameter, DM")
204.
205.  DrMin = DM * np.cos(np.pi/6.)  # minimal radial spacing
206.  print(DrMin,"is the minimal radial spacing, DrMin")
207.
208.  A = DrMin/LH # first part of equation for blocking
209.  print(A,"is the first part of equation for calculating blocking fact
      or, A")
210.  Bd = 1 - (A*((math.degrees(math.cos(elev)+ (math.degrees(math.tan(be
      ta)*math.degrees(math.sin(elev))/math.degrees(math.cos(Omega))))))))

211.  print(Bd)
212.  B = math.radians(Bd)
213.  print(B, "is the second part of equation for calculating blocking fa
      ctor, B")
214.
215.  C = ((2*whr)-(math.sqrt(1+whr**2))+DS)/whr
216.  print(C, "is the second part of equation for calculating blocking fa
      ctor, C")
217.  fb = 1 -B*C
218.  print(fb, "is the blocking factor, fb")
219.  if fb > 1:
220.      blockeff = 1
221.      print(blockeff, "is the blocking efficiency, fb")
222.  else:
223.      blockeff = fb
224.  print(blockeff, "is the blocking efficiency, blockeff")
```

The Interception efficiency for a receiver with a height of 3.15 m and a diameter of 4.25 m is calculated using the double integral function in Mathematica software using the following expression:

$$\text{ETA} = 1/(2\text{Pi}\sigma^2)\,\text{Integrate}[\text{Integrate}[\text{Exp}[-(x^2+y^2)/(2\sigma^2)],\{x,-a,a\}],\{y,-b,b\}]$$
$$\text{ETA}/.\{\sigma \to 1.6012, a \to 3.15, b \to 4.25\}$$

References

Abengoa, 2015. Atacama 1: Project Brochure.

Abengoa, 2012. Industrial production, Abengoa annual report 2012.

Amsbeck, L., Buck, R., Pfahl, A., Uhlig, R., 2007. Optical Performance and Weight Estimation of a heliostat with ganged facets, Solar Enerey.

Arbes, F., Weinrebe, G., Wöhrbach, M., 2016. Heliostat Field Cost Reduction By " Slope Drive " Optimization Azimuth-Elevation Tracking, Conference proceedings SolarPACES 2015. Cape Town, South Africa.

Augsburger, G., 2013. Thermo-economic optimisation of large solar tower power plants. École Polytechnique Federale de Laussane. doi:10.5075/epfl-thesis-5648

Augsburger, G., Das, A.K., Boschek, E., Clark, M.M., 2016. Thermo-Mechanical and Optical Optimization of the Molten Salt Receiver for a Given Heliostat Field. SolarPACES Conf. procedings 2015 030005. doi:10.1063/1.4949057

Balz, M., Göcke, V., Keck, T., Reeken, F. Von, Weinrebe, G., Wöhrbach, M., 2016. Stellio – Development , Construction and Testing of a Smart Heliostat, in: AIP Conference Proceedings. AIP Publishing. doi:10.1063/1.4949026

Balz, M., Reeken, F. Von, 2015. Environmental Loading Conditions for CSP Solar Fields, in: Energy Procedia. Elsevier B.V., Beijing, China, pp. 1–8.

Belhomme, B., Pitz-Paal, R., Schwarzbözl, P., Ulmer, S., 2009. A New Fast Ray Tracing Tool for High-Precision Simulation of Heliostat Fields. J. Sol. Energy Eng. 131, 031002. doi:10.1115/1.3139139

Bender, W., 2013. Final Technical Progress Report : Development of Low-Cost Suspension Heliostat Final Technical Progress Report : Development of Low-Cost Suspension Heliostat. Norwich, Vermont.

Besarati, S.M., Goswami, Y., 2014. A computationally efficient method for the design of the heliostat field for solar power tower plant. Renew. Energy 69, 226–232. doi:10.1016/j.renene.2014.03.043

Bhargav, K.R., Gross, F., Schramek, P., 2013. Life cycle cost optimized heliostat size for power towers, in: Energy Procedia. Elsevier B.V., pp. 40–49. doi:10.1016/j.egypro.2014.03.005

Biggs, F., Vittitoe, C.N., 1979. Helios model for the optical behavior of reflecting solar concentrators, NASA STI/Recon Technical Report N. Albuquerque, New Mexico.

Björkman, N., 2014. Heliostat Design. KTH Royal Institute of Technology.

Blackmon, J.B., 2015. Personal communation.

Blackmon, J.B., 2013. Parametric determination of heliostat minimum cost per unit area. Sol. Energy 97, 342–349. doi:10.1016/j.solener.2013.08.032

Blackmon, J.B., 2012. Heliostat size optimization for central receiver solar power plants, in: Concentrating Solar Power Technology: Principles, Developments and Applications. Woodhead Publishing Limited.

Blair, N., Dobos, A.P., Freeman, J., Neises, T., Wagner, M., Ferguson, T., Gilman, P., Blair, N., Dobos, A.P., Freeman, J., Neises, T., Wagner, M., Ferguson, T., Gilman, P., 2014. System Advisor Model , SAM 2014 . 1 . 14 : General Description. Golden, Colorado.

Blanco, M.J., Amieva, J.M., Mancilla, A., 2005. The Tonatiuh Software Development Project: An open source approach to the simulation of solar concentrating systems, in: Proceedings of the ASME Computers and Information in Engineering Division. pp. 157–164. doi:10.1115/IMECE2005-81859

Blanco-Muriel, M., Alarcón-Padilla, D.C., López-Moratalla, T., Lara-Coira, M., 2001. Computing the solar vector. Sol. Energy 70, 431–441. doi:10.1016/S0038-092X(00)00156-0

BrightSource, 2014. Ivanpah Solar Electric Generating System.

Buck, R., Wurmhöringer, K., Lehle, R., Göttsche, J., Pfahl, A., 2010. Development of a 30m^2 heliostat with hydraulic drive, in: SolarPaces Conference. pp. 1–8.

Buie, D., Monger, a. G., Dey, C.J., 2003. Sunshape distributions for terrestrial solar simulations. Sol. Energy 74, 113–122. doi:10.1016/S0038-092X(03)00125-7

Cádiz, P., Frasquet, M., Silva, M., Martínez, F., Carballo, J., 2015. Shadowing and blocking effect optimization for a variable geometry heliostat field. Energy Procedia 69, 60–69. doi:10.1016/j.egypro.2015.03.008

Cardemil, J., Starke, A., Scariot, V., Grams, I., Colle, S., 2014. Evaluating Solar Radiation Attenuation Models to Assess the Effects of Climate and Geographical Location on the Heliostat Field Efficiency in Brazil. Energy Procedia 49, 1288–1297. doi:10.1016/j.egypro.2014.03.138

CEPCI, 2015. Chemical Engineering Plant Cost Index [WWW Document]. URL WWW.Chemengonline.com/PCI (accessed 4.30.16).

Christian, J., Moya, A., Andraka, C., Yuan, J., 2015. Probabilistic Analysis to Quantify Optical Performance and Error Budgets for Next Generation Heliostats. J. Sol. Energy Eng. 137, 1–8. doi:10.1115/1.4029376

Collado, F.J., 2009. Preliminary design of surrounding heliostat fields. Renew. Energy 34, 1359–1363. doi:10.1016/j.renene.2008.09.003

Collado, F.J., 2008a. Quick evaluation of the annual heliostat field efficiency. Sol. Energy 82, 379–384. doi:10.1016/j.solener.2007.10.007

Collado, F.J., 2008b. Preliminary design of surrounding heliostat fields, in: Conference Proceedings SolarPACES 2008. pp. 1–7.

Collado, F.J., Guallar, J., 2016. Two-stages optimised design of the collector field of solar power tower plants. Sol. Energy 135, 884–896. doi:10.1016/j.solener.2016.06.065

Collado, F.J., Guallar, J., 2013. A review of optimized design layouts for solar power tower plants with campo code. Renew. Sustain. Energy Rev. 20, 142–154. doi:10.1016/j.rser.2012.11.076

Collado, F.J., Guallar, J., 2012. Campo: Generation of regular heliostat fields. Renew. Energy 46, 49–59. doi:10.1016/j.renene.2012.03.011

Collado, F.J., Turégano, J. a., 1989. Calculation of the annual thermal energy supplied by a defined heliostat field. Sol. Energy 42, 149–165. doi:10.1016/0038-092X(89)90142-4

Coventry, J., Pye, J., 2013. Heliostat cost reduction - Where to now? Energy Procedia 49, 60–70. doi:10.1016/j.egypro.2014.03.007

Crespo, L., Dobrotkova, Z., Philberibert, C., Richter, C., Simbolotti, G., Turchi, C., Wenhua, X., 2012. Concentrating Solar Power. doi:10.1016/B978-0-08-087872-0.00319-X

D'Ortigue, O.L., 2015. Renewable Energy Capacity Statistics 2015. doi:10.1016/j.renene.2014.09.059

de Meyer, O.A.J., Dinter, F., Govender, S., 2016. Thermal resistance model for CSP central receivers, in: SolarPACES Conference Procedings 2015. p. 030010. doi:10.1063/1.4949062

Donker, P. Van Den, Rosinga, G., Voorthuysen, E.M. Van, 2016. Reducing Heliostat Field Costs by Direct Measurement and Control of the Mirror Orientation. Conf. Proc. SolarPACES 2015.

Dostal, V., Driscoll, M.J., Hejzlar, P., 2004. A Supercritical Carbon Dioxide Cycle for Next Generation Nuclear Reactors. Tech. Rep. MIT-ANP-TR-100 1–317. doi:MIT-ANP-TR-100

Duffie, J. a., Beckman, W. a., 2013. Solar Engineering of Thermal Processes, Fourth Edi. ed. John Wiley & Sons, Inc., Wisconsin-Madison.

Dyreby, J., Klein, S., Nellis, G., Reindl, D., 2014. Design Considerations for Supercritical Carbon Dioxide Brayton Cycles With Recompression. J. Eng. Gas Turbines Power 136, 101701. doi:10.1115/1.4027936

Emes, M.J., Arjomandi, M., Nathan, G.J., 2015. Effect of heliostat design wind speed on the levelised cost of electricity from concentrating solar thermal power tower plants. Sol. Energy 115, 441–451. doi:10.1016/j.solener.2015.02.047

ESKOM, 2016. Concentrating solar power generation [WWW Document]. URL http://www.eskom.co.za/news/Pages/Jan22B.aspx (accessed 2.25.16).

ESTELA, Greenpeace, SolarPACES, 2016. Solar Thermal Electricity - Global Outlook 2016.

Ewert, M., Fuentes, O.N., 2012. Modeling sun shape and optical error in a solar tower power plant.

Falcone, P.K., 1986. A handbook for Solar Central Receiver Design. Livermore.

Fluri, T.P., 2009. The potential of concentrating solar power in South Africa. Energy Policy 37, 5075–5080. doi:10.1016/j.enpol.2009.07.017

García, L., Burisch, M., Sanchez, M., 2015. Spillage Estimation in a Heliostats Field for Solar Field Optimization, in: SolarPaces Conference Precedings 2014. pp. 1–8.

Garcia, P., Ferriere, A., Bezian, J.-J., 2008. Codes for solar flux calculation dedicated to central receiver system applications: A comparative review. Sol. Energy 82, 189–197. doi:10.1016/j.solener.2007.08.004

Gauché, P., Backström, T.W. Von, Brent, A.C., 2011. Csp Modeling Methodology for Macro Decision Making - Emphasis on the Central Receiver Type, in: Proceedings of Solar Power and Chemical Energy Systems Conference (SolarPACES 2011). pp. 1–8.

General Motors Corporation, 1979. Heliostat Production Evaluation and Cost Analysis Executive Summary. Golden, Colorado.

Georgiou, M.D., Bonanos, A.M., Georgiadis, J.G., 2013. Caustics as an Alternate of Ray Tracing to Evaluate Heliostat Mirrors. Conf. Pap. Energy 2013, 1–7. doi:10.1155/2013/395659

Gertig, C., Delgado, A., Hidalgo, C., Ron, R., 2013. SoFiA - A novel simulation tool for Central Receiver Systems, in: Energy Procedia. pp. 1361–1370. doi:10.1016/j.egypro.2014.03.145

Geyer, M., 2014. Constructing CSP Plants in the Kalahari Desert. Stellenbosch.

Google, 2013. RE < C : Google Heliostat Project Overview.

Grobler, A., 2015. Aiming strategies for small central receiver. Stellenbosch University.

Grobler, A., Gauché, P., 2014. a Review of Aiming Strategies for Central Receivers, in: Sasec 2014. pp. 1–8.

Guédez, R., Topel, M., Spelling, J., Laumert, B., 2015. Enhancing the Profitability of Solar Tower Power Plants through Thermoeconomic Analysis Based on Multi-objective Optimization, in: Energy Procedia. Elsevier B.V., pp. 1277–1286. doi:10.1016/j.egypro.2015.03.155

Hardt, M., Martínez, D., González, A., Garrido, C., Aladren, S., Villa, J.R., Saenz, J., 2011. HECTOR – heliostat cleaning team-oriented robot. SolarPaces Conf.

Heimsath, A., Lindner, P., Klimm, E., Schmid, T., Moreno, O., Nitz, P., 2016. Specular Reflectance of Soiled Glass Mirrors – Study on the Impact of Incidence Angles, in: Conference Proceedings SolarPACES 2015.

Helman, U., Jacobowitz, D., 2014. The Economic and Reliability Benefits of CSP with Thermal Energy Storage : Literature Review and Research Needs.

Hirsch, T., Feldhoff, J.F., 2012. Start-Up Modeling for Annual CSP Yield Calculations. J. Sol. Energy Eng. 134, 1–9. doi:10.1115/1.4006268

Ho, C.K., Iverson, B.D., 2014. Review of high-temperature central receiver designs for concentrating solar power. Renew. Sustain. Energy Rev. 29, 835–846. doi:10.1016/j.rser.2013.08.099

Ho, C.K., Mahoney, A.R., Ambrosini, A., Bencomo, M., Hall, A., Lambert, T.N., 2014. Characterization of Pyromark 2500 Paint for High-Temperature Solar Receivers. J. Sol. Energy Eng. 136, 014502. doi:10.1115/1.4024031

Hoffmann, J., Madaly, K., 2015. On Thermal Energy Storage Capacity for CSP Plant in South Africa. R D J. South African Inst. Mech. Eng. 31, 46–51.

Hottel, H.C., 1976. A simple model for estimating the transmittance of direct solar radiation through clear atmospheres. Sol. Enerey 18, 129–134. doi:10.1016/0038-092X(76)90045-1

Huang, W., Li, L., Li, Y., Han, Z., 2013. Development and evaluation of several models for precise and fast calculations of shading and blocking in heliostats field. Sol. Energy 95, 255–264. doi:10.1016/j.solener.2013.06.016

Huss, S., Traeger, Y.D., Shvets, Z., Rojansky, M., Stoyanoff, S., Garber, J., 2011. Evaluating effects on wind loads in heliostat design, in: SolarPaces Conference.

Iqbal, M., 1983. Chapter 1 - Sun–earth astronomical relationships, in: Iqbal, M.B.T.-A.I. to S.R. (Ed.), An Introduction to Solar Radiation. Academic Press, pp. 1–28. doi:http://dx.doi.org/10.1016/B978-0-12-373750-2.50006-9

IRENA, 2016. The Power to Change: Solar and Wind Cost Reduction Potential to 2025.

IRENA, 2013. Concentrating Solar Power: Technology Brief.

Iverson, B.D., Conboy, T.M., Pasch, J.J., Kruizenga, A.M., 2013. Supercritical CO2 Brayton cycles for solar-thermal energy. Appl. Energy 111, 957–970. doi:10.1016/j.apenergy.2013.06.020

Jones, S., 2000. Heliostat Cost as a Function of Size For Molten-Salt Power Towers.

Kistler, B.L., 1986. A user's manual for DELSOL3: A computer code for calculating the optical performance and optimal system design for solar thermal central receiver plants. Albuquerque, New Mexico. doi:SAND86-8018

Kolb, G., Ho, C., Mancini, T., Gary, J., 2011. Power tower technology roadmap and cost reduction plan, SAND2011-2419. Albuquerque, New Mexico. doi:10.2172/1011644

Kolb, G.J., Jones, S.A., Donnelly, M.W., Gorman, D., Thomas, R., Davenport, R., Lumia, R., 2007. Heliostat Cost Reduction Study, Sandia Report. Albuquerque, New Mexico. doi:10.2172/912923

Kost, C., Mayer, J.N., Thomsen, J., Hartmann, N., Senkpiel, C., Philipps, S., Nold, S., Lude, S., Saad, N., Schlegl, T., 2013. Levelized Cost of Electricity Renewable Energy Technologies.

Kunert, J., Pfahl, A., Buck, R., 2009. Dimensioning heliostat drives considering dynamic wind loads, in: SolarPaces Conference. pp. 1–8.

Kurup, P., Turchi, C.S., 2015. Parabolic Trough Collector Cost Update for the System Advisor Model (SAM) Parabolic Trough Collector Cost Update for the System Advisor Model (SAM).

Kusek, S., 2011. Low Cost Heliostat Development - DOE - CSP Program review.

Landman, W.A., 2013. Optical performance of the refelective surface profile of a heliostat. University of Stellenbosch.

Landman, W.A., Gauché, P., 2014. Analysis of canting strategies using the HFLCAL model, in: Proceedings of SASEC 2014. Port Elizabeth, South Africa, pp. 1–7.

Landman, W.A., Grobler, A., Gauché, P., Dinter, F., 2016. Incidence angle effects on circular Gaussian flux density distributions for heliostat imaging. Sol. Energy 126, 156–167. doi:10.1016/j.solener.2015.12.008

Larmuth, J., Malan, K., Gauché, P., 2013. Design and cost review of a two square metre heliostat prototypes. Proc. SASEC.

Larmuth, J.N., Landamn, W.A., Gauché, P., 2016. A top-down approach to heliostat

cost reduction, in: SolarPACES Conference Procedings 2015. AIP Publishing, Cape Town, South Africa, pp. 020013–1–8. doi:10.1063/1.4949037

Lata, J., Alcalde, S., Fernández, D., Lekube, X., 2010. First surrounding field of heliostats in the world for commercial solar power plants - Gemasolar. Solarpaces 1–9.

Lata, J.M., Rodríguez, M., de Lara, M.A., 2006. High Flux Central Receivers of Molten Salts for the New Generation of Commercial Stand-Alone Solar Power Plants. p. 021002. doi:10.1115/1.2884576

Leary, P.L., Hankins, J.D., 1979. User's guide for MIRVAL: a computer code for comparing designs of heliostat-receiver optics for central receiver solar power plants, Sand-77-8280.

Leonardi, E., D'Aguanno, B., 2011. CRS4-2: A numerical code for the calculation of the solar power collected in a central receiver system. Energy 36, 4828–4837. doi:10.1016/j.energy.2011.05.017

Lipps, F.W., Vant-Hull, L.L., 1980. Programmer's manual for the University of Huston computer code RCELL: cellwise optimization for the solar central receiver project. Report SAND-0763e1. Sandia National Labs; 1980. Albuquerque, New Mexico.

Lipps, F.W., Vant-Hull, L.L., 1978. A cellwise method for the optimization of large central receiver systems. Sol. Energy 20, 505–516. doi:10.1016/0038-092X(78)90067-1

Lovegrove, K.M., Stein, W.H., 2012. Concentrating solar power technology: Principles, developments and applications. Woodhead Publishing Limited, 2012, Cambridge.

Lutchman, S.L., 2014. Heliostat Field Layout Optimization for a Central Receiver. Stellenbosch University.

Lutchman, S.L., Groenwold, a. a., Gauché, P., Bode, S., 2014. On using a gradient-based method for heliostat field layout optimization, in: Energy Procedia. pp. 1429–1438. doi:10.1016/j.egypro.2014.03.152

Madaly, K., 2014. Identifying the optimum storage capacity for a 100 - MW e concentrating solar power plant in South Africa. Stellenbosc University.

Malan, K.J., 2014. A Heliostat Field Control System. Stellenbosch University.

Mehos, M., Turchi, C., Jorgenson, J., Denholm, P., Ho, C., Armijo, K., 2016. On the Path to SunShot : Advancing Concentrating Solar Power Technology, Performance and Dispatchability. Golden, Colorado.

Meyen, S., Lüpfert, E., Pernpeintner, J., Fend, T., 2009. Optical characterisation of

reflector material for Concentrating Solar Power technology. SolarPaces Conf. 1–7.

Meyer, A.J., 2013. The South African Refit: Solar resource assessmet options for CSP developers, in: Proceedings of SASEC 2012. Stellenbosch, South Africa, pp. 1–9.

Meyer, A.J., 2012. The South African REFIT: Solar resource assessment options for solar developers., in: Proceedings of SASEC. Stellenbosch, pp. 1–9.

Monreal, A., Burisch, M., Sanchez, M., Pérez, D., Villasante, C., Olabarrieta, E., Olasolo, D., Olarra, A., 2014. EASY: An Innovative Design for Cost Effective Heliostats/Solar Fields, in: Energy Procedia. Elsevier B.V., pp. 174–183. doi:10.1016/j.egypro.2014.03.019

Montecchi, M., 2016. Proposal of a New Parameter for the Comprehensive Qualification of Solar Mirrors for CSP Applications, in: Conference Proceedings SolarPACES 2015.

Monterreal, R., Heller, P., 1997. Large area heliostat comparison at PSA. Internal Report, PSA.

Müller-Steinhagen, H., Trieb, F., 2004. Concentrating solar power - A review of the technology. Q. R. Acad. Eng. 43–50. doi:10.1126/science.1168539

Mutuberria, A., Pascual, J., Guisado, M. V, Mallor, F., 2015. Comparison of Heliostat Field Layout Design methodologies and impact on power plant efficiency, in: Energy Procedia.

Neises, T., Turchi, C., 2013. A comparison of supercritical carbon dioxide power cycle configurations with an emphasis on CSP applications, in: Energy Procedia. pp. 1187–1196. doi:10.1016/j.egypro.2014.03.128

Nemet, G.F., 2006. Beyond the learning curve: factors influencing cost reductions in photovoltaics. Energy Policy 34, 3218–3232. doi:10.1016/j.enpol.2005.06.020

Noone, C.J., Torrilhon, M., Mitsos, A., 2012. Heliostat field optimization: A new computationally efficient model and biomimetic layout. Sol. Energy 86, 792–803. doi:10.1016/j.solener.2011.12.007

NREL, 2014. System Advisor Model (SAM).

Ong, S., Campbell, C., Denholm, P., Margolis, R., Heath, G., 2013. Land-Use Requirements for Solar Power Plants in the United States, Nrel/Tp-6a20-56290.

Pacheco, J.E., 2002. Final Test and Evaluation Results from the Solar Two Project. Albuquerque, New Mexico.

Pacheco, J.E., Reilly, H.E., Kolb, G.J., Tyner, C.E., 2000. Summary of the Solar Two

test and evaluation program. Albuquerque, New Mexico.

Pan, C.A., 2015. Joint CSP and PV power plant simulation – enabling economic power production through combined operation.

Pawel, I., 2014. The cost of storage - How to calculate the levelized cost of stored energy (LCOE) and applications to renewable energy generation, in: Energy Procedia. Elsevier B.V., pp. 68–77. doi:10.1016/j.egypro.2014.01.159

Peterka, J., Tan, L., 1987. Mean and peak wind load reduction on heliostats, SERI/STR-253-3212. Gol.

Pfahl, A., 2014. Survey of Heliostat Concepts for Cost Reduction. J. Sol. Energy Eng. 136, 014501–(1–9). doi:10.1115/1.4024243

Pfahl, A., Randt, M., Holze, C., Unterschütz, S., 2013. Autonomous light-weight heliostat with rim drives. Sol. Energy 92, 230–240. doi:10.1016/j.solener.2013.03.005

Pfahl, A., Randt, M., Meier, F., Zaschke, M., Geurts, C.P.W., Buselmeier, M., 2015. A Holistic Approach for Low Cost Heliostat Fields, in: Energy Procedia SolarPACES 2014. Elsevier B.V., Beijing, China, pp. 178–187. doi:10.1016/j.egypro.2015.03.021

Pitman, C.L., Vant-Hull, L.L., 1989. The University of Houston Solar Central Receiver Code System: Concepts, Updates, and Start-up Kits . United States: N. p., 1989. United States.

Pitman, C.L., Vant-Hull, L.L., 1984. Atmospheric Transmittance Model for a Solar Beam Propagating between a Heliostat and a Receiver.

Pitz-Paal, R., Dersch, J., Milow, B., 2005. ECOSTAR: European Concentrated Solar Thermal Road-Mapping.

Reda, I., Andreas, A., 2003. Solar Position Algorithm for Solar Radiation Applications (Revised). Nrel/Tp-560-34302 1–56. doi:10.1016/j.solener.2003.12.003

Reeken, F. Von, Nicodemo, D., Keck, T., Weinrebe, G., Balz, M., 2016a. Key aspects of cost effective collector and solar field design, in: Conference Proceedings SolarPACES 2015. Cape Town, South Africa, pp. 1–8.

Reeken, F. Von, Weinrebe, G., Keck, T., Balz, M., 2016b. Heliostat cost optimization study, in: Conference Proceedings SolarPACES 2015. Cape Town, South Africa, pp. 1–8.

Relancio, J., Cuellar, A., Walker, G., Ettmayr, C., 2016. South African CSP Projects Under the REIPP Programme – Requirements , Challenges and Opportunities, in: Conference Proceedings SolarPACES 2015.

Relloso, S., Lata, J., 2011. Molten Salt Thermal Storage: A Proven Solution to increase Plant Dispatchability. Experience in Gemasoalr Tower Plant, in: Solar Paces. pp. 1–6.

REN21, 2016. Renewables 2016 Global status report. Paris.

REN21, 2015. Renewables 2015 Global status report. (Paris: REN21 Secretaria, pp. 1–251).

Ricklin, P., Slack, M., Rogers, D., Huibregtse, R., 2013. Commercial readiness of eSolar next generation heliostat. Energy Procedia 49, 201–208. doi:10.1016/j.egypro.2014.03.022

Ridley, J.N., 1982. Packing efficiency in sunflower heads. Math. Biosci. 58, 129–139. doi:10.1016/0025-5564(82)90056-6

Salome, A., Chhel, F., Flamant, G., Ferriere, A., Thiery, F., 2013. Control of the flux distribution on a solar tower receiver using an optimized aiming point strategy: Application to THEMIS solar tower. Sol. Energy 94, 352–366. doi:10.1016/j.solener.2013.02.025

Sánchez, M., Romero, M., 2005. Methodology for generation of heliostat field layout in central receiver systems based on yearly normalized energy surfaces. Sol. Energy 80, 861–874. doi:10.1016/j.solener.2005.05.014

Sargent & Lundy LLC Consulting Group, 2003. Assessment of Parabolic Trough and Power Tower Solar Technology Cost and Performance Forecasts, Report No. NREL/SR-550-34440. Golden, Colorado. doi:NREL/SR-550-34440

SBP, 2015. Point-focusing Solar Energy Technology : Stellio Heliostat confirms unprecedented optical and economic performance.

Scheffler, O.C., 2015. Optimization of an Optical Field for a Central Receiver Solar Thermal Power Plant. Stellenbosch University.

Schell, S., 2011. Design and evaluation of esolar's heliostat fields. Sol. Energy 85, 614–619. doi:10.1016/j.solener.2010.01.008

Schmitz, M., Schwarzbözl, P., Buck, R., Pitz-Paal, R., 2006. Assessment of the potential improvement due to multiple apertures in central receiver systems with secondary concentrators. Sol. Energy 80, 111–120. doi:10.1016/j.solener.2005.02.012

Schramek, P., Mills, D.R., 2003. Multi-tower solar array. Sol. Energy 75, 249–260. doi:10.1016/j.solener.2003.07.004

Schwarzbözl, P., Schmitz, M., Pitz-Paal, R., 2009. Visual HFLCAL – A Software Tool for Layout and Optimisation of Heliostat Fields, in: SolarPACES Conference.

Seidel, W., 2010. Model developmenet and annual simulation of the supercritical carbon dioxide Brayton cycle for concentrating solar power applications. University of Wisconsin-Madison.

Sengupta, M., Habte, A., Kurtz, S., Dobos, A., Wilbert, S., Lorenz, E., Stoffel, T., Renné, D., Gueymard, C., Myers, D., Wilcox, S., Blanc, P., Perez, R., 2015. Best Practices Handbook for the Collection and Use of Solar Resource Data for Solar Energy Applications Best Practices Handbook for the Collection and Use of Solar Resource Data for Solar Energy Applications.

Sengupta, M., Wagner, M., 2012. Atmospheric attenuation in central receiver systems from dni measurements. Proc. Sol. Power Chem. Energy Syst. Conf. (SolarPACES 2012) 6. doi:10.1115/ES2012-91229

Sengupta, M., Wagner, M., 2011. Impact of Aerosols on Atmospheric Attenuation Loss in Central Receiver Systems, in: Solar Paces. p. 6.

Siala, F.M.F., Elayeb, M.E., 2001. Mathematical formulation of a graphical method for a no-blocking heliostat field layout. Renew. energy 23, 77–92. doi:10.1016/S0960-1481(00)00159-2

Siebers, D.L., Kraabel, J.S., 1984. Estimating convective energy losses from solar central receivers 69. doi:SAND84-8717

Silinga, C., Gauché, P., Rudman, J., Cebecauer, T., 2015. The South African REIPPP two-tier CSP tariff : Implications for a proposed hybrid CSP peaking system. jhbsfjrbhgfedjgb 00.

Sobin, A., Wagner, W., Easton, C.R., 1976. Central collector solar energy receivers. Sol. Energy. doi:10.1016/0038-092X(76)90032-3

SolarReserve, 2015. Redstone Solar Thermal Power Project [WWW Document]. URL http://www.solarreserve.com/en/global-projects/csp/redstone

Spelling, J.D., 2012. Solar Power Technologies: Concentrated Solar Power. Stockholm, Sweden.

Spencer, J.W., 1971. Fourier series representation of the position of the sun. Search 10, 2569–2571.

Srilakshmi, G., Venkatesh, V., Thirumalai, N.C., Suresh, N.S., 2015. Challenges and opportunities for Solar Tower technology in India. Renew. Sustain. Energy Rev. 45, 698–709. doi:10.1016/j.rser.2015.02.016

Stine, W.B., Geyer, M., 2001. Power From The Sun.

Stoddard, L., Abiecunas, J., Connell, R.O., 2006. Economic , Energy , and Environmental Benefits of Concentrating Solar Power in California Economic , Energy , and Environmental Benefits of Concentrating Solar Power in

California. Golden, Colorado.

Stoddard, M.C., Faas, S.E., Chiang, C.J., Dirks, J.A., 1987. SOLERGY - A Computer Code for Calculating the Annual Energy from Central Receiver Power Plants.

Stone, K.W., Jones, S. a, 1995. Analysis of solar two heliostat tracking error sources. Proc. Renew. Adv. Energy Syst. 21st Century, a Jt. ASME/JSME/JSES/KSME Int. Conf. 10. doi:SAND99-0239C

Sukhatme, S.P., 1996. Solar Energy: Principles of Thermal Collection and Storage, Second Edi. ed. Tata McGraw-Hill.

Suri, M., 2011. Site Assessment of Solar Resource :Upington Solar Park.

Tahboub, Z., Oumbe, a., Hassar, Z., Obaidli, a., 2013. Modeling of irradiance attenuation from a heliostat to the receiver of a solar central tower. Energy Procedia 49, 2405–2413. doi:10.1016/j.egypro.2014.03.255

Tonopah Solar Energy LLC, 2009. Crescent Dunes Solar Energy Project. Santa Monica, California.

Trieb, F., 2007. Concentrating Solar Power for Seawater Desalination. Stuttgart, Germany.

Trieb, F., Schillings, C., Sullivan, M.O., Pregger, T., Hoyer-klick, C., 2009. Global Potential of Concentrating Solar Power. Middle East 0, 1–11.

Turchi, C.S., Heath, G. a, 2013. Molten Salt Power Tower Cost Model for the System Advisor Model (SAM). Golden, Colorado.

U.S. Department of Energy, 2013. SunShot Concentrating Solar Power Program Review 2013. Phoenix, Arizona.

U.S. Department of Energy, 2012. SunShot Vision Study. doi:SunShot, Energy Efficiency and Renewable Energy, U.S. Department of Energy. NREL Report No. BK5200-47927; DOE/GO-102012-3037

Ulmer, S., 1998. Influences of cost reduction measures on the beam quality of a large-area heliostat. Plataforma Solar de Almería, Spain.

van Rooyen, D.W., Schöttl, P., Bern, G., Heimsath, A., Nitz, P., 2016. Optical advantages of astigmatic aberration corrected heliostats, in: SolarPACES Conference Procedings 2015. p. 020026. doi:10.1063/1.4949050

Vant-Hull, L.L., 2012. Central tower concentrating solar power (CSP) systems, in: Lovegrove, K., Stein, W. (Eds.), Concentrating Solar Power Technology: Principles, Developments and Applications. Woodhead Publishing Limited, 2012, Cambridge, pp. 240–283. doi:10.1016/B978-1-84569-769-3.50008-X

Vant-Hull, L.L., 2002. The Role of “Allowable Flux Density” in the Design and

Operation of Molten-Salt Solar Central Receivers. J. Sol. Energy Eng. 124, 165. doi:10.1115/1.1464124

Vant-Hull, L.L., 1976. Methods for estimating total flux in the direct solar beam at any time, in: Boer, K.W. (Ed.), Proceedings of the Sharing the Sun So- Lar Technology in the Seventies Joint Conference of the International So- Lar Energy Society and the Solar Energy Society of Canada. Winnipeg, Canada, p. 369. doi:10.1142/9789814374439

Vant-Hull, L.L., Winter, C.-J., Sizmann, R.L., 1991. Concentrator optics, in: Solar Power Plants: Fundamentals, Technology, Systems, Economics. Springer Science & Business Media.

Vazquez, J., Relloso, S., Domingo, M., 2006. Sener heliostat design and testing. Proc. 2006 SolarPACES Int. Symp. 1–8.

Vittitoe, C.N., Biggs, F., 1977. HELIOS: a computer program for modeling the solar thermal test facility : a users guide. Sandia National Laboratories, Albuquerque, New Mexico.

Vogel, H., 1979. A better way to construct the sunflower head 189, 179–189.

Wagner, M.J., 2015. SolarPILOT User' s Manual.

Wagner, M.J., 2008. Simulation and Predictive Performance Modeling of Utility-Scale Central Receiver System Power Plants. University of Wisconsin - Madison.

Wagner, M.J., Wendelin, T., 2016. SolarPILOT: A Tool for Solar Power Tower Layout and Optimization. Golden, Colorado.

Walzel, M.D., Lipps, F.W., Vant-Hull, L.L., 1977. A solar flux density calculation for a solar tower concentrator using a two-dimensional hermite function expansion. Sol. Energy 19, 239–253. doi:10.1016/0038-092X(77)90067-6

Wang, M., Vandal, R., Thomsen, S., 2010. Durable Concentrating Solar Power (CSP) Mirrors, in: SolarPaces Conference. pp. 1–5.

Wei, X., Lu, Z., Wang, Z., Yu, W., Zhang, H., Yao, Z., 2010. A new method for the design of the heliostat field layout for solar tower power plant. Renew. Energy 35, 1970–1975. doi:10.1016/j.renene.2010.01.026

Weinrebe, G., 2014. Holistic Design and Optimization - Concept & Application.

Weinrebe, G., Reeken, F. Von, Wöhrbach, M., Plaz, T., Göcke, V., Balz, M., 2014. Towards holistic power tower system optimization, in: Energy Procedia. Elsevier B.V., pp. 1573–1581. doi:10.1016/j.egypro.2014.03.166

Wendelin, T., 2003a. SolTRACE: A New Optical Modeling Tool for Concentrating

Solar Optics, in: Proceedings of the ISEC 2003: International Solar Energy Conference. pp. 253–260. doi:10.1115/ISEC2003-44090

Wendelin, T., 2003b. SolTRACE: A New Optical Modeling Tool for Concentrating Solar Optics, Proceedings of the ISEC 2003: International Solar Energy Conference. doi:10.1115/ISEC2003-44090

Wilbert, S., Geuder, N., 2013. Sunshape analysis and atmospheric influences, Sfera.

Winter, C.-J., Sizmann, R.L., Vant-Hull, L.L., 1991. Solar power plants: fundamentals, technology, systems, economics. Springer Science & Business Media.

WMO, 2008. Guide to Meteorological Instruments and Methods of Observation, WMO-No. 8.

Woolf, H.., 1968. On the computation of solar elevation angles and the determintaion of sunrise and sunset times, NASA TM X-1646.

Wright, T., 1936. Factors Affecting the Cost of Airplanes. J. Aeronaut. Sci. (Institute Aeronaut. Sci. 3, 122–128. doi:10.2514/8.155

Wu, C.F.J., Hamada, M., 2000. Experiments: Planning, analysis, and parameter design optimization. John Wiley & Sons, INC.

www.Landbou.com, 2016. Farm for sale in Upington [WWW Document]. URL http://property.landbou.com/3?bedroom?farm?for?sale?in?upington?103706065 (accessed 5.16.16).

Yao, Z., Wang, Z., Lu, Z., Wei, X., 2009. Modeling and simulation of the pioneer 1MW solar thermal central receiver system in China. Renew. Energy 34, 2437–2446. doi:10.1016/j.renene.2009.02.022

Yellowhair, J., Andraka, C.E., 2013. Evaluation of advanced heliostat reflective facets on cost and performance, in: Energy Procedia. pp. 265–274. doi:10.1016/j.egypro.2014.03.029

Zavoico, A.B., 2001. Solar Power Tower Design Basis Document Revision 0. San Francisco, California.

Zhang, M., Du, X., Yang, L., Xu, C., Yang, Y., 2015a. Comparing Study of Biomimetic Spiral and Radial Staggered Layouts of the Heliostat Field, in: Energy Procedia. pp. 242–249. doi:10.1016/j.egypro.2015.03.028

Zhang, M., Yang, L., Xu, C., Du, X., 2015b. An efficient code to optimize the heliostat field and comparisons between the biomimetic spiral and staggered layout. Renew. Energy 87, 720–730. doi:10.1016/j.renene.2015.11.015